

**GRAVITY MODELING OF THE PAKA GEOTHERMAL PROSPECT IN BARINGO
COUNTY, NORTHERN KENYA RIFT**

WAFULA CHEMBENI PETER

**A thesis Submitted to the Graduate School in Partial Fulfillment for the Requirements
of the Master of Science Degree in Physics of Egerton University**

**EGERTON UNIVERSITY
NOVEMBER 2018**

DECLARATION AND RECOMMENDATION

DECLARATION

This thesis is my original work and has not been submitted award of Degree or Diploma or for examination in any institution

Signature.....

Date.....

Wafula Chembeni Peter

SM13/23542/14

RECOMMENDATION

This thesis has been submitted with our approval as supervisors for examination according to Egerton University regulations.

Signature.....

Date.....

Dr. M. S. K. Kirui

Egerton University

Signature.....

Date.....

Dr. Antony Wamalwa

Geothermal Development Company

COPYRIGHT

© 2018, Wafula Chembeni Peter

All rights reserved. No part of this thesis may be reproduced, stored in a retrieval system or transmitted in any form or by any means, electronic, mechanical, photocopying, recording or otherwise, without the prior permission in writing from the copyright owner or Egerton University.

DEDICATION

I dedicate this work to my parents Mr. Richard Chembeni Karibu and Mrs. Gladys Nasambu Chembeni. To my brothers and sisters Daniel, Samuel, Vitalis and Kenneth, Felister, Susan and Annemary.

ACKNOWLEDGEMENT

I thank the Lord God Almighty, Our creator for granting me this life, being faithful to me and giving me the knowledge, wisdom, patience and strength in pursuing this geophysical study. This study would not have been successful without the guidance and help of several individual and institutions who in one way or another contributed and extended their assistance in preparation and completion of this study. Primarily, it is with immense gratitude that I acknowledge the support and help of my supervisors Dr. Wamalwa Antony of Geothermal Development Company, Nakuru and Dr. M.S.K. Kirui of Physics Department, Egerton University. Their advice, mentorship, goodwill and guidance through proposal preparation, research as well as thesis write-up and financial support are highly valued. I acknowledge the Department of Physics, Egerton University since, this is where I was registered and trained for my MSc Physics. Hence, this work would not be the way it is without the Department of Physics. It gives me great pleasure to acknowledge staff members from the Department Physics of Egerton University for their relevant academic guidance, providing useful insights and suggestions during the entire research work. I share the credit of my work with Mr. Ndongoli, Noor, and Gichira from the Geothermal Development Company, Nakuru for assistance in data acquisition. I give credit of my work to Paka volcano Pokot community, who provided direction to inaccessible areas of the volcano and security protection for the entire work of data collection. Also, the Geosoft team for providing me with Geosoft Oasis Montaj software and useful insights into how to work with the software. Much of gratitude to my dear family for the financial and moral support. With gratitude, I acknowledge my MSc classmates and Kizito for the encouragement they gave me, sharing an enthusiasm for and comments on my work. Lastly, I thank my beloved wife Bridgit Nyongesa for the constant moral and financial support she selflessly gave me all through the period while doing my work – a debt I can never truly repay, but something for which I am forever thankful.

ABSTRACT

Paka volcano is situated in active northern Kenya rift. It is considered one of the geothermal prospects. It has been covered by most studies that focused on the regional tectonic evolution of the East Africa Rift, lithospheric and crustal structural analysis. However, regional analysis overlooked local analysis, where key geothermal structural features like thin massive intrusive and shallow faults that are significant have remained relatively poorly constrained. Hence, the key concealed structural features at local analysis have not been mapped at regional analysis. The study is an advancement of the regional analysis in the northern Kenya rift to a detailed local analysis in Paka volcano. This study aimed at developing a Bouguer anomaly map showing different relative density distribution in the subsurface, to generate a 3D inversion models from Bouguer anomaly data, to interpret the 3D density model developed from gravity data inversion, to delineate the subsurface volcanic fault structures with the view to determine their influence to the hydrothermal fluid flow and contributions to the geothermal system. A total of 157 gravity data points were established over the prospect area for gravity modeling and geological structures delineation at local analysis. Raw data were reduced to Bouguer data and band pass and upward filter were used to generate Bouguer maps. For local analysis, residual data was separated from regional data through application of filters. Our gravity analysis method produced the following results: Bouguer anomaly maps revealed regions of positive gravity anomalies and negative gravity anomalies that trend in a northwest direction. An inversion model under positive gravity regions revealed an intrusive dykes. At a depth less than 1000 m from the surface, the intrusive dyke were interpreted as due to lava rocks of magnesium iron reach and at depth greater than 3000 m as due intrusive magma that can serve as a geothermal heat source. The negative gravity zones were due to mean fractured rocks to a lower calculated density range ($1.90 - 2.40$ g/cm 3) that can serve as a good storage for geothermal fluids. 3D density model revealed a high density distribution that is associated with the existence of several intrusive rocks within the study area that is overlain with surficial pyroclastic or Paka Basalt of layer thickness 200 – 300 m across the prospect of calculated density range ($2.20 - 2.60$ g/cm 3) that may serve as a capping layer for geothermal system around Paka volcano. The gravity data also reveals several NW – SE trending of the mapped structural features that are parallel to the major rift fault and pre-existing Proterozoic regional structures in the northern Kenya rift which seems to have played a role in guiding the orientation and trending for this local structural feature in Paka area. The study revealed and delineated both deep and shallow subsurface faults at shallow depth that are essential in enhancing geothermal fluid permeability. Among the many recommendations highlighted, the study emphasizes an exploratory geothermal borehole drilling be undertaken in Paka prospect from the caldera summit towards the eastern flank and northwestern flank along the fault zones.

TABLE OF CONTENTS

DECLARATION AND RECOMMENDATION	II
COPYRIGHT	III
DEDICATION.....	IV
ACKNOWLEDGEMENT.....	V
ABSTRACT	VI
TABLE OF CONTENTS	VII
LIST OF TABLES	XI
LIST OF FIGURES	XI
LIST OF ABBREVIATIONS AND ACRONYMS	XIV
LIST OF SYMBOLS	XV
CHAPTER ONE	1
INTRODUCTION.....	1
1.1 Background Information.....	1
1.2 Statement of the Problem.....	4
1 .3 Objectives	4
1.3.1 Main Objective.....	4
1.3.2 Specific Objectives.....	4
1.4 Hypotheses	4
1.5 Justification	5
CHAPTER TWO	6
LITERATURE REVIEW	6
2.1 Overview.....	6
2.2 The Gravity Method.....	6
2.2.1 The Theory of Gravity Methods.....	7
2.2.2 Gravimeter.....	8
2.2.3 Differential Global Positioning Survey (DGPS)	8
2.3 Data Processing and Corrections	9
2.3.1 Drift and Tidal Corrections	9
2.3.2 Terrain and Bathymetry Correction	10
2.3.3 Sensor Height Correction	12
2.3.4 Latitude Correction	12

2.3.5 Free Air Correction (FAC)	13
2.3.6 Bouguer Correction (BC)	13
2.4 Datum.....	15
2.5 Gridding	15
2.5.1 Mathematical Aspect of Kriging	16
2.5.2 Kriging Overview Theory	17
2.6 Geophysical Data Enhancement	17
2.6.1 Descriptive and Application of Linear Transformations (filters).....	18
2.6.2 Fourier Transform Filters	19
2.6.3 Convolution.....	21
2.6.4 Band pass Filters	22
2.6.5 Upward and Downward Continuation.....	22
2.7 Derivatives	23
2.7.1 Horizontal Derivatives or Horizontal Gradients (HG)	23
2.7.2 Tilt Derivative (TDR).....	24
2.7.3 Horizontal Derivative of the Tilt Derivative (HG-TDR)	24
2.7.4 Analytic Signal (AS)	24
2.8 Theoretical Aspects of Geophysical Modeling	25
2.8.1 Geophysical Data Modeling.....	26
2.8.2 Forward Modeling.....	26
2.8.3 Inverse Modeling.....	26
2.8.4 VOXI Earth Modeling (Inversion Software) Theory	27
2.9 Tectonic and Geology of Paka prospect	29
2.10 Physiography of the Inner Trough of Paka Volcano	30
2.11 Previous Geophysical Studies.....	31
2.11.1 Gravity Studies	31
2.11.2 Resistivity Studies	33
2.11.3 Seismic Studies	33
2.11.4 Summary	34
CHAPTER THREE	35
MATERIALS AND METHODS	35
3.1 The Study Area	35

3.2 Materials for Gravity Data Collection and Processing	35
3.3 Survey Design and Field Operations	36
3.4 Developing Bouguer Anomaly Map.....	38
3.4.1 Gravity Data Pre-Processing (Data Reduction)	38
3.4.2 Setting the Projected Coordinate System of Paka Geothermal Prospect	38
3.4.3 Gridding	38
3.4.4 Kriging of Bouguer Channel.....	38
3.4.5 Kriging of Elevation Channel	39
3.4.6 Filtering	40
3.4.7 Floating Grid	40
3.4.8 Generating Gravity Bouguer Anomaly Maps using the Step-By-Step Filtering	40
3.5 The 3D Inversion Model.....	40
3.5.1 Gravity Anomaly Separation.....	40
3.5.2 Calculating the Residual Grid	41
3.5.3 Constraints on Crustal Structure	41
3.5.4 Preparing VOXI for Inversion and the Gravity Inversion Model	42
3.5.5 Gravity inversion Modeling	43
3.6. The 3D Density Model and Interpretation.....	43
3.7 Delineating the Subsurface Fault Structures.....	44
CHAPTER FOUR.....	45
RESULTS AND DISCUSSION	45
4.1 Overview.....	45
4.2 Bouguer Anomaly Maps	45
4.3 A Residual Gravity Map Showing the Area of Interest	47
4.3.1 3D Gravity Inversion Model for Region A (<i>Riongo area</i>).....	47
4.3.2 3D Gravity Inversion Model for Region B (<i>Cheptebesia</i>)	48
4.3.3 The 3D Inversion Model for Region C (<i>Paka summit</i>).....	49
4.3.4 Inversion Model for Region D (<i>Paka west</i>)	50
4.3.5 The Inversion Model for Region E (<i>Tuwot</i>)	51
4.3.6 An Inversion Model for Region F (<i>Eastern flank of Paka summit</i>)	52
4.3.7 An Inversion Model for Region G (<i>South Riongo area</i>).....	53
4.3.8 Gravity Inversion Model for Region H (<i>southern flank of Paka summit area</i>)	53

4.4 The 3D Density Model of Paka Prospect.....	54
4.5 Delineating the Subsurface Fault Structures in Paka Prospect	58
4.5.1 Horizontal Gradient contour map.....	58
4.5.2 Tilt Derivative Contour Map (Tilt Depth Map)	59
4.5.3 Horizontal Derivative of the Tilt Derivative Contour Map.....	60
4.5.4 An Analytic Signal Contour Map.....	61
4.6 Discussion of the Results	62
CHAPTER FIVE	68
CONCLUSIONS AND RECOMMENDATIONS.....	68
5.1 Conclusion	68
5.1.1 Conclusion on the Bouguer Anomaly Map under paka volcano	68
5.1.2 Conclusion on 3D Gravity Inversion Models	68
5.1.3 Conclusion on the Interpretation of 3D Density Model	68
5.1.4 Conclusion on delineating the subsurface volcanic fault structures, there influence on the hydrothermal fluid flow and contribution to the geothermal system in Paka volcano.....	69
5.2 Recommendations.....	69
5.2.1 Recommendations Based on this Research Results	69
5.2.2 Recommendation for Further Studies	69
REFERENCES.....	70

LIST OF TABLES

Table 1: The zones and number of compartments in a zone under Graticule chart.....	9
Table 2: Kenya rift axial seismic velocity versus density values	45
Table 3: P-wave velocity model, layer thickness, and lithology	53

LIST OF FIGURES

Figure 1.1: A map showing the location of Paka geothermal prospect	2
Figure 2.1: CG-5 Autograv gravimeter.....	8
Figure 2.2: Variation of Bouguer anomaly with geoid elevation in Paka prospect	14
Figure 2.3: Geostatistical gridding technique for random data, non-parallel data	16
Figure 2.4: The spectrum of a prism with top and bottom.....	18
Figure 2.5: Spectrum shifted to a lower wavenumber as the prism depth increases.....	19
Figure 2.6: A graphical representation of convolution.....	20
Figure 2.7: An upward continuation with highlighted regional features.....	21
Figure 2.8: Downward continuation with highlighted near surface features.....	21

Figure 2.9: Tikhonov curve	26
Figure 2.10: Location of fumaroles, crater and faults in Paka volcano	27
Figure 3.1: The Elevation of Paka Volcano Mountain in the Kenya rift valley.....	32
Figure 3.2: Gravity data coverage in Paka prospect showing gravity station locations	33
Figure 3.3: Gravity measurement being taken in the field	34
Figure 3.4: Total Bouguer anomaly grid after Kriging.....	36
Figure 3.5: Elevation grid of Paka area.....	36
Figure 3.6: A mesh showing the Area of Interest (AOI).....	39
Figure 3.7: Unconstrained 3D model inversion model.....	39
Figure 4.1: The surface N-S trending faults, crater and caldera in Paka prospect.....	41
Figure 4.2: Bouguer anomaly map at 2 km depth from earth surface	42
Figure 4.3: Bouguer anomaly map at 5 km depth from earth surface	43
Figure 4.4: A residual gravity map	44
Figure 4.5: A residual gravity map showing the anomaly regions to be modelled.....	44
Figure 4.6: Regional A clipped to density range $2.77 \text{ g/cm}^3 - 2.941 \text{ g/cm}^3$	46
Figure 4.7: Regional A modeled to density $2.88 \text{ g/cm}^3 - 2.941 \text{ g/cm}^3$	46
Figure 4.8: A 3D modelled body for region B at to density range $(2.675 - 2.953) \text{ g/cm}^3$	47
Figure 4.9: A intrusive body for region C at density range $2.787 - 3.176 \text{ g/cm}^3$	48
Figure 4.10: Modeled body for region D at density range $(2.71 - 3.025) \text{ g/cm}^3$	49
Figure 4.11: An inversion model for region E $(2.675 - 2.791) \text{ g/cm}^3$	50
Figure 4.12: An inversion model for region F at density range $(2.528 - 2.682) \text{ g/cm}^3$	51
Figure 4.13: Inversion Model at Density Range $(2.00 - 2.417) \text{ g/cm}^3$	52
Figure 4.14: An inversion model for region H at density range $(2.281 - 2.658) \text{ g/cm}^3$	53
Figure 4.15: The 3D gravity inversion model of Paka Prospect	54
Figure 4.16: The 3D density model of Paka prospect.....	54
Figure 4.17: Profile 99000 in the y-direction across the 3D density model	55
Figure 4.18: Profile 99800 in the y-direction across the 3D density model	55
Figure 4.19: Profile 102700 in the y-direction across the 3D density model	56
Figure 4.20: Profile 108500 in the y-direction across the 3D density model	56
Figure 4.21: The horizontal gradient map	58
Figure 4.22: The tilt derivative map	59
Figure 4.23: Horizontal derivative of the tilt derivative map	60

Figure 4.24. The Analytic signal map61

LIST OF ABBREVIATIONS AND ACRONYMS

AOI	Area Of Interest
AS	Analytic Signal
BC	Bouguer Correction
BS	Base Station
CBA	Complete Bouguer Anomaly
DEM	Digital Elevation Model
DGPS	Differential Global Positioning Survey
EARS	East African Rift System
E.T.C	Earth Terrain Correction
FAA	Free Air Anomaly
FAC	Free Air Correction
FFT	Fast Fourier Transform
GABS	Gravity Absolute Base Station
GDC	Geothermal Development Company
GRS80	Geodetic Reference System 1980
GPS	Global Positioning Surveys
HG	Horizontal Gradient
HG-TDR	Horizontal Gradient of the Tilt Derivative
IGF	International Gravity Formula
ITRF	International Terrestrial Reference Frame
KRISP	Kenya Rift International Seismic Project
KRV	Kenya Rift Valley
LC	Latitude Correction
Ma	Million years ago
MT	Magnetotelluric
NNE	North North-East
SBA	Simple Bouguer Anomaly
TDR	Tilt Derivative
X	Eastings
Y	Northings

LIST OF SYMBOLS

d^{obs}	Observed geophysical data
d^{pre}	Predicted model response
δ_d	The model error
G_{obs}	Observed gravity
h_t	Depth to the top
h_b	Depth to the bottom
λ	Regularization parameter (data values)
ρ_a	Apparent resistivity
ρ	Rock density
φ_d	Data misfit
φ_m	Model norm
φ_T	Total objective function
\emptyset	Latitude in radians
ω	Wavenumber
$E(r)$	Data spectrum
G	Gravitational constant
g.u	Gravity unit
H	Elevation in meters
M	Number of voxel
M_E	Mass of the earth
N	Number of observations
R_E	The radius of the earth 6370 km
Z	Vertical component of gravity

CHAPTER ONE

INTRODUCTION

1.1 Background Information

The Kenyan rift system is part the East African Rift System (EARS), which is an example of an active continental rift zone with its arm extending from southern Ethiopia through central Kenya into Tanzania (Dunkley *et al.*, 1993; Ring, 2014; Muirhead *et al.*, 2015). The rift encompasses most of the geothermal prospects and fields that are associated with Quaternary volcanic center and fissure, which relates to the recent tectonic activity of the rift floor (Omenda, 2000; Omenda *et al.*, 2000; Waswa, 2017). These geothermal prospects include, from south to north: Suswa, Longonot, Eburru, Arus-Bogoria, Korosi, Chepchuk, Paka, Silali, Emuruangogolak, Namarunu and Barrier volcanic complex while the geothermal field are Olkaria and Menengai (Figure. 1.1) (Ouma, 2010). Paka volcano is situated approximately 25 km north of Lake Baringo and 15 km east of Nginyang' village at $00^{\circ} 25' N$ and $36^{\circ} 12' E$. The volcano rises to a maximum altitude of 1697 m with an irregular outline covering an area of approximately 280 km^2 (Lagat *et al.*, 2007; Kanda *et al.*, 2011; Waswa, 2017).

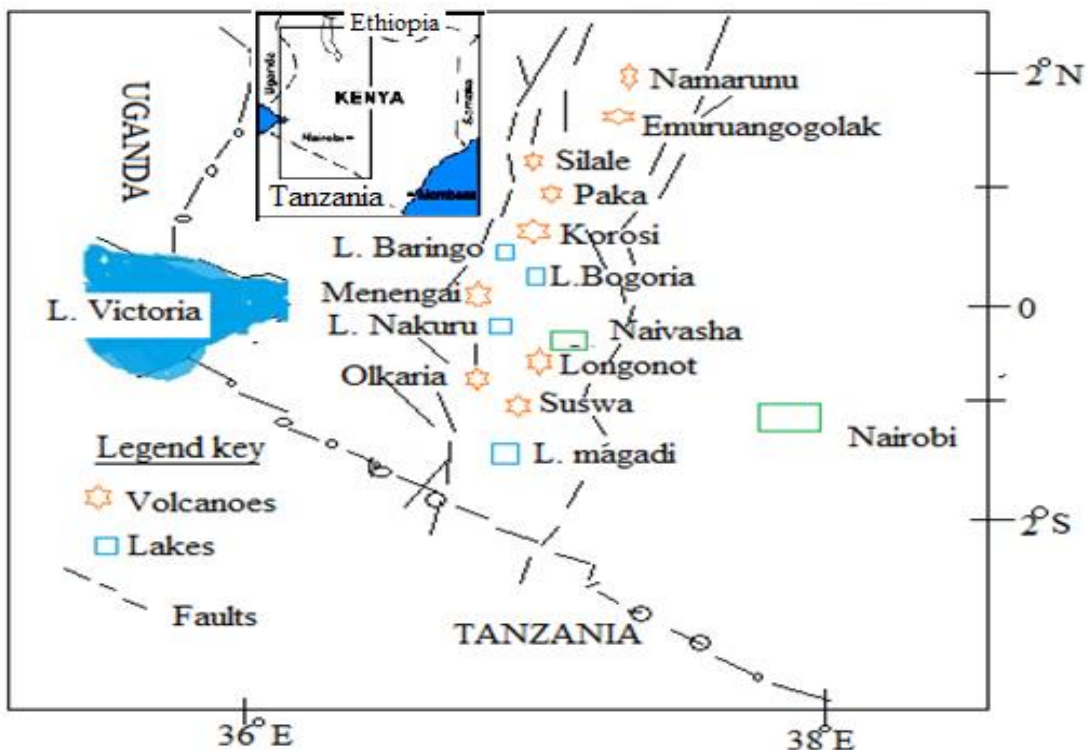


Figure 1.1: A map showing the location of Paka volcano

Paka volcano is dominated by trachyte-basaltic volcanism that resulted in the formation of the young central caldera at the summit which is 1.5 km in diameter. The tectonic and volcanic activities commenced by 390 ka and continued to within 10 ka that resulted in the formation of a broad zone normal faulting 7.5 km wide graben bound by eastern and western fault respectively (Omenda, 2007; Mwakirani, 2011; Robertson *et al.*, 2016; Waswa, 2017). The oldest exposed rocks are Trachyte which constructed an early volcanic shield. The subsequent fracturing of the shield by NNE trending faults was accompanied by an eruption of lower basalt from fissures sources on the eastern flank of the volcano (Dunkley *et al.*, 1993). The eruptions of the young basaltic lavas within the caldera and along the fissures to the north of the volcano are indicators that the magma chamber in Paka volcano is still active (Tapponnier and Molnar, 1977; Mutonga, 2013; Omenda, 2014b). Also, the occurrence of seismic events observed to the east flank of the Paka volcano are indicators of active fault zone (Simiyu and Keller, 2000; Patlan *et al.*, 2017).

The prolonged magmatic and volcanic activities under Paka volcano, have characterize the volcano with high level of (earthquake activities) seismicity events and intense surface geothermal manifestations like steaming ground, fumaroles, altered rocks or minerals, hot springs and *Fimbristylis exilis* ‘geothermal grass’ (Lagat *et al.*, 2007; Connor *et al.*, 2000; Kanda *et al.*, 2011). Presence of surface geothermal manifestations and seismicity events (that occurs at local, regional and teleseismic), thrilled us to explore the volcano.

Since the 1970s, Kenyan rift has been a target for some geophysical and geological investigations, especially the southern rift as compared to the northern rift. Studies focused on the regional tectonic evolution of Kenyan rift, lithospheric and crustal structural analysis. These results were summarised in three collections of papers (Prodehl *et al.*, 1994, 1997; Morley, 1999). Regional seismic and gravity studies based on the results of the KRISP project that provided many new constraints on the lithospheric structure and revealed significant differences between the northern and southern parts of the Kenya Rift (Simiyu and Keller, 2001; Mariita and Keller, 2007). For example, Bouguer gravity anomaly values increased by 200 mGal towards the Lake Turkana region, but are mostly due to crustal thinning (Mechie *et al.*, 1994). These studies also showed that the crustal thickness decreases along the rift from about 35 km around Lake Magadi in the south to 20 km in the north at Lake Turkana and this was explained as due to northward increase in extensional force that exist on the upper crust (Keller *et al.*, 1994; Mariita, 2003; Mariita and Keller, 2007).

The regional Bouguer gravity data covering the central and southern Kenya rift revealed that all the volcanic centers (e.g. Menengai, Eburru, Olkaria and Suswa) are associated with positive gravity anomalies superimposed on the regional gravity low (Simiyu and Keller, 1997, 2001). Modeling this broad gravity low using KRSIP seismic result as constraints, Simiyu and Keller (1997, 2001) showed that it is due to less dense mantle under the Kenya dome. The gravity highs were modeled and interpreted as resulting from the magmatic volcanic centers underlain by discrete mafic bodies at regional depth (6 – 40 km). Also, axial gravity high was explained as resulting from densification of the basement or the upper crust discrete dike intrusions (Simiyu and Keller, 2001). Mariita and Keller (2007) extended the results of Simiyu and Keller (1997, 2001) to the northern Kenyan rift (from Menengai to Lake Turkana) at regional analyses. As observed by previous studies done in the southern rift, Mariita and Keller (2007) explained the gravity high observed along the rift axis as due to mafic bodies associated with the main volcanic centers or due to densification of the upper crust as diking or as host blocks when Precambrian basement has been brought near the surface. Recently, the Kenya rift lithospheric structure has been revisited based on regional 3D gravity modeling (Sippel *et al.*, 2017). The study indicated an overall trend of increasing mean crustal densities from mainly less than 2880 kgm^{-3} in Western Kenya to more than 2880 kgm^{-3} in the eastern Kenya, which implies an increase in the crustal integrated strength from western to the eastern Kenya. Also, the study explained the positive gravity anomaly in Kenya rift crustal at the regional analysis as due to magnesium and iron rich mafic intrusions. While the gravity ‘low’ in the northern Kenya rift was explained as due to positive thermal anomalies within the crust that involves partial melting which strongly weakens the lithosphere.

Most of this studies focused on regional tectonic evolution of the East Africa rift, lithospheric and crustal structures at regional analysis. Regional analysis significantly maps deeper structural features associated with long wavelengths. However, regional analysis overlooked local analysis, where key geothermal structural features like thin massive intrusive and shallow faults that are significant have remained relatively poorly constrained. Hence, the key concealed structural features at local analysis like thin massive intrusive and shallow faults that are associated with short wavelengths have not been mapped at regional analysis. This study is an extension of the studies carried out at a regional analysis in northern Kenya rift to a detailed local analysis in Paka prospect. The study sought to improve and bring out new information on the subsurface density distribution patterns that can be used to explain the

shallower structures in the Paka prospect. Through investigating gravity variations over Paka volcano at shallow analysis, the study presented 3D inversion models of gravity data and the 3D density model which helped to constrain the shape and depth of massive magmatic intrusion. In this way, the geological interpretation was derived from the models.

1.2 Statement of the Problem

Kenya rift has been studied widely in terms of tectonic evolution of the rift, lithospheric and crustal structural analysis. The studies maps deeper structural features associated with long wavelengths. However, regional analysis overlooks local analysis, where key geothermal structural features like thin massive intrusion and shallow faults that are significant have remained relatively poorly constrained or they have not been mapped at regional analysis. Hence there was a need to extend earlier regional studies in northern Kenya rift to a detailed local analysis < 5 Km in Paka prospect. Our study focused on modeling the key concealed geothermal heat sources in form of dikes and faults structural features at local analysis < 5 Km with the view to improve and bring out new information on subsurface density distribution associated with local geothermal structural resources of the prospect.

1 .3 Objectives

1.3.1 Main Objective

To generate a geological interpretation from the density models derived from the gravity data inversion modeling of the Paka volcano

1.3.2 Specific Objectives

- i. To develop a Bouguer anomaly map showing different relative density distribution in the subsurface
- ii. To generate a 3D inversion models from simple Bouguer anomaly data
- iii. To interpret the 3D density model developed from gravity data
- iv. To delineate the subsurface volcanic fault structures in Paka volcano with the view to determine their influence in the hydrothermal fluid flow in the area and contribution to the geothermal system

1.4 Hypotheses

- i. Bouguer anomaly data does not show significantly different relative density anomalies distribution in the local topography
- ii. The 3D inversion model cannot be significantly affected by the local topography

- iii. The 3D density model data reflects both the mapped geology and the unmapped geological features but it does not significantly relate to the local topography
- iv. Buried faults structures are detected by gravity method and they have a significant influence in the hydrothermal fluid flow and contribution to the geothermal system of an area

1.5 Justification

Gravity method provides fast hand information in locating and delineating the crustal intrusions that are associated volcanic centres. Hence, the discovery of geothermal heat sources within an area is of great economic importance in geothermal prospects. Since the discovery of geothermal resources can create employment opportunity for the residents, provides an alternative source of energy for the country and encourage the use of clean energy which does not pollute the environment. Increase of amount of electricity supplied to the national grid thus lowering the cost of production.

CHAPTER TWO

LITERATURE REVIEW

2.1 Overview

The focus of this study was to generate a geological interpretation from a density model derived from gravity inversion at Paka. The study involved gravity data reduction, inversion, modeling, interpretation, application of gravity derivatives and analytical signal filters. In this chapter, the gravity theory associated with data reduction techniques, modeling theory, data enhancement theory, previous studies, Paka physiography, tectonics and geology of Paka volcano are presented.

2.2 The Gravity Method

Gravity method is widely used in determining the subsurface spatial distribution of rock density for mapping ore bodies, minerals, archeological site based on different rock densities and especially in geothermal prospects for mapping of faults and delineating geothermal heat source. The distribution of rock density, ρ , causes a small change in the earth's gravitational field strength, g , (Simiyu and Keller, 2001; Mariita, 2003; Cooper, 2004; Hinze *et al.*, 2005; Kearey *et al.*, 2013; Ochieng, 2014). The variation of density in the subsurface cause's anomalies within the crust, and this can be detected and measured using the ground-based gravimeters. Once the gravity at a new field site is known (observed gravity), theoretical gravity is calculated. The theoretical gravity depends on latitude, elevation and the surrounding topography. The difference between the observed and the theoretical gravity is known as the Bouguer anomaly. If the Bouguer is negative, it means the observed gravity is less than the theoretical gravity (Mauri *et al.*, 2017). A positive gravity anomaly is associated with shallow intruding high-density bodies, whereas gravity lows are associated with shallow low-density porous bodies (Simiyu and Keller, 2001; Mariita and Keller, 2007; Roecker *et al.*, 2017).

As per the monopole source of the gravity field, the amplitude of g is proportional to scale change, that is, if a structure has doubled the size of another (or the density contrast doubles) then the gravity effects will also double. Thus, the gravitational effects of large regional density structures, therefore, often dominate the gravity maps and the gravity effects due to shallow small-scale structures that are of interest may only represent a small percentage of the gravity signal (less than 10%) (Fairhead, 1976). The gravitational accelerations are neither influenced nor generated by an observer, but it is affected by the ground vibrations. Thus, the observed gravity is generally a composite of contributions from all depths within the

usual range of exploration, and such contributions can be individually resolved only in special cases (Mulwa *et al.*, 2011; Kearey *et al.*, 2013; Mulwa and Mariita, 2013). The results obtained from a geophysical gravity investigation are subjective and only rely on geologic interpretation. Thus, geophysical gravity methods do not measure directly the parameter needed to solve the problem, but instead, measures the density contrast in the rock properties.

2.2.1 The Theory of Gravity Methods

The aim of gravity method is to determine the spatial variation in the acceleration due to gravity, g , which depends on the mass (density and volume) of the rocks underlying a survey area (Telford *et al.*, 1990; ParASNIS, 1997; Hinze *et al.*, 2005; Kearey *et al.*, 2013). Gravity has its base in Newton's law of universal gravitation (equation 1), that is;

$$F = G \frac{m_1 \cdot m_2}{r^2} \quad (1)$$

Where F is the magnitude of the gravitational force between the two point masses that represents the hanging mass inside the gravimeter and the variation due to rock mass brought about by density contrast in the subsurface; G is the gravitational constant approximately equal to $6.673 \times 10^{-11} \text{ N m}^2 \text{ kg}^{-2}$; m_1 and m_2 are the first and second point mass and r is the distance between the two point masses.

The gravitational acceleration has the unit m/s^2 (1 mGal equals 10^{-5} m/s^2), which is the SI unit for acceleration. There exists a significant difference at various points on the earth when measuring the acceleration. In gravity modeling, the gravitational acceleration (g) is modeled. For perfectly spherical earth, with R_E as the radius and without any rotation, the acceleration is (equation 2);

$$g = G \frac{M_E}{R_E^2} \quad (2)$$

Where M_E is the mass of the Earth ($= 5.97 \times 10^{24} \text{ Kg}$) and R_E is the radius of the Earth (Hinze *et al.*, 2005; Kearey *et al.*, 2013).

Since the reference earth is a rotating ellipsoid, where the equatorial diameter is greater than the polar diameter, there needs to be a correction for the latitude. The gravitational acceleration g is less at the equator because it is further away from the center of the earth. Also, because of its rotation, the earth tends to fling bodies away from its rotation axis. The centrifugal force is dependent on the distance from the axis; the maximum is at the equator and decreases to zero at the poles. Both effects vary with the latitude, ϕ , and are combined in the International Gravity Formula (Hinze *et al.*, 2005; Girdler, 2013).

$$g_\phi = 978031.8 (1+0.0053024\sin^2\phi-0.0000059\sin^22\phi) \text{ mGals} \quad (3)$$

2.2.2 Gravimeter

The CG-5 Autograv is an automated gravimeter which works based on a quartz spring system. Observations are processed in real time with an onboard microprocessor (Figure. 2.1). Other than an initial leveling, there is no manual intervention in making the measurement hence there is no human-induced random error. The measurement range of the instrument is over 8000 mGal, and the lowest count is 0.001 mGals. The portability and fast data acquisition scheme of the instrument makes it convenient for large-scale surveys. The instrument measures the relative gravity of sampling at 6 Hz and six samples are averaged every second and the reading after each second is displayed. The data is stored in flash memory and subsequently transferred to a computer. The gravity sensor, the control system, and the battery are encased in a double casing which increases the stability of the instrument (Hinze *et al.*, 2005; Bhattacharya *et al.*, 2006; Kearey *et al.*, 2013).



Figure 2.1: CG-5 Autograv gravimeter

2.2.3 Differential Global Positioning Survey (DGPS)

The DGPS measures the latitude, longitude, and elevation of the gravity station to a reading resolution of 5 mm. The DGPS has a transmitter and a receiver (Figure. 3.3); the transmitter is located at a higher elevated point in order to send a signal to the satellite and communicates with the receiver to locate the gravity station in terms of latitude, longitude, and elevation (Odera, 2016; Mauri *et al.*, 2017).

2.3 Data Processing and Corrections

Extraneous effects affect the observed raw gravity data. The raw data is affected by a wide variety of sources of varying amplitudes, periods and wavelengths that generally mask gravity variables of geophysical interest. In order to isolate a small gravity signal of interest from the raw gravity data, unwanted gravity signals and noise from the raw data are removed. This conversion procedure is commonly known as correction or reduction of gravity data (Hinze *et al.*, 2005; Mulwa *et al.*, 2011; Kearey *et al.*, 2013). For gravity observations to be used for any meaningful geological and geophysical interpretation, they must be reduced from the extraneous effects to anomaly form, which depends only on the lateral density variation in the subsurface gravitational field. According to Hinze *et al.* (2005), a gravity anomaly is a difference between observed gravity and the value of gravity anomaly at the station based on a uniform ellipsoid of the earth without any lateral density variations. In the same way, Bouguer gravity anomaly is the difference between observed gravity and the theoretically calculated gravity.

The objective of gravity survey is to determine the spatial variations in the earth's gravitational field, which is dependent on subsurface density, or mass variations. The observed gravity field, however, includes effects due to elevation, nearby and distant topography (mass inhomogeneities), latitude and tidal effects due to the gravitational attraction of the sun and the moon on the earth. Hence, before gravity data can be used for any meaningful geological and geophysical interpretations. The data must be reduced (corrected) for all these effects to obtain a true representation of the variations in the gravitational field, which is dependent on density variations only (Grant and West, 1965; Telford *et al.*, 1990; Blakely, 1995; Parasnis, 1997; Kearey *et al.*, 2013). As a result, gravity data from the Paka volcano was subjected to various standard reductions as outlined in the preceding sections.

2.3.1 Drift and Tidal Corrections

Gravity meter drift is the variation in meter reading with time, probably due to temperature variation in the solid-state creep of the internal spring. Also, earth tides due to the attraction between the earth and both the moon and the sun cause periodic variations in gravity reading, which may be as large as $\approx 0.3\text{mGals}$ (Mariita, 2003; Mariita and Keller, 2007; Mulwa *et al.*, 2011). These factors cause small systematic and predictable changes in gravity field readings with time. The drift of the instrument can be removed by starting and ending groups (or gravity survey loops) of gravity measurements at the same base stations. The difference of

readings at the base station will be equal to drift plus tidal effects. The tidal corrections can be calculated and removed from the base station difference leaving only the drift component, which can be distributed about the survey of gravity measurements such that both base and field stations result in having identical values. In Paka volcano, gravity survey loops began at the single base station. After taking a reading at the base station, readings were taken at each field station at least three times before proceeding to the next field station. At the end of a survey loop, gravity reading was taken at the base station. The difference in base station reading equals tidal effects, plus instrument drift.

$$\text{Drift} = \frac{G_{\text{base},F} - G_{\text{base},i}}{T_{\text{base},F} - T_{\text{base},i}} \quad (4)$$

Where *Drift* is the drift rate of measurement. $G_{\text{base},F}$ - $G_{\text{base},i}$, are the final and initial total gravity field measurements at the base station, $T_{\text{base},F}$ – $T_{\text{base},i}$ are the final and initial time at the base station (Hinze *et al.*, 2005). The drift correction in the field at any station in the loop for a given day is calculated from:

$$D_{\text{Drift } n} = G_n * (T_n - T_i) \quad (5)$$

Where $D_{\text{Drift } n}$ is the drift correction for the gravity at the n^{th} station, G_n the total gravity at the n^{th} Station, T_n Time at the n^{th} Station and T_i Time at the first station of the loop (Hinze *et al.*, 2005).

2.3.2 Terrain and Bathymetry Correction

The gravity effect departures of topography from the assumed horizontal slab or spherical cap used in marking the Bouguer correction is referred as the terrain correction (Hinze *et al.*, 2005). The terrain correction may include the bathymetry of bodies of water. Gravity surveys in moderately to extremely rugged topography requires meticulous reduction for terrain effects. Terrain correction continues to be the most significant source of error in gravity data reduction (Hammer, 1939) since hills attract the mass of gravity meter whereas valleys are considered mass deficiencies and hence have a negative density concerning the surrounding rocks. The net effect of hills and valleys is therefore to reduce the observed gravity value of the station. Terrain correction is calculated and compounded effect of topography is always positive (Hammer, 1939; Grant and West, 1965; Dobrin and Savit, 1988; Telford *et al.*, 1990; Parasnis, 1997; Hinze *et al.*, 2005; Girdler, 2013). Implementation of good field procedures

and a comprehensive approach to data treatment can significantly reduce errors in the gravity anomaly values. These field procedures include a careful selection and placement of gravity stations away from abrupt changes in elevation such that elevation differences in zone A is zero. The precise determination of elevation of inner zones B, C and D and extension of terrain to at least zone O, 166.7 km (Figure 2.2) (Hinze *et al.*, 2005; Kearey *et al.*, 2013).

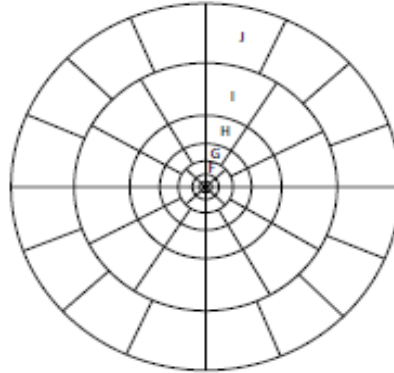


Figure 2.2: Graticule chart for calculation of terrain correction (Kearey *et al.*, 2013)

Table 1: The zones and number of compartments in a zone under Graticule chart (Kearey *et al.*, 2013)

Zone	r_1	r_2	n	Zone	r_1	r_2	n
B	2.0	16.6	4	H	1529.4	2614.4	12
C	16.6	53.3	6	I	2614.4	4468.8	12
D	53.3	170.1	6	J	4468.8	6652.2	16
E	170.1	390.1	8	K	6652.2	9902.5	16
F	390.1	894.8	8	L	9902.5	14740.9	16
G	894.8	1529.4	12	M	14740.9	21943.3	16

$$T = 0.4191 \frac{\rho}{n} \left(r_2 - r_1 + \sqrt{(r_1^2 + z^2)} - \sqrt{(r_2^2 + z^2)} \right) \quad (6)$$

Where T = terrain correction of compartment (mGal); ρ = Bouguer correction density (2.67 g/cm^3 .); n = number of compartments in a zone; r_1 = inner radius of zone (m); r_2 = outer radius of zone (m); and z = modulus of elevation difference between observation point and the mean elevation of compartment (m)

The terrain correction of compartment can be calculated for any given radius under the Graticule chart using figure 2.2, table 1 and the equation 6.

Traditionally, elevation difference between gravity station and the surrounding terrain for the inner zones is made in the field by visual observation, and terrain corrections applied using

standard table 1. From the gravity station, the topography is divided into zones; zone B covers a radius of 14.6 m and has 4 compartments; zone C covers a radius of 36.6 m and has 6 compartments, and zone D covers a radius of 116.8 m and has 6 compartments, for other zones the same can be done (Hinze *et al.*, 2005; Kearey *et al.*, 2013). For Paka geothermal volcano, an elevation grid does not extend up to 166.7 km but approximately the elevation grid ranges from 16 km to 30 km depending on the direction.

2.3.3 Sensor Height Correction

Sensor height correction is given by equation 7 and then it is subtracted from the gravity reading.

$$\text{Sensor height correction} = 0.3086 (h + 0.089) \quad (7)$$

Where h , is the sensor height of the spring to the flat ground and the constant 0.089 is the height above the spring to the top of the gravimeter, and 0.3086 is a height conversion constant. Since the increase in R_E by the Sensor height risen, g has decreased by 0.3086 mGal per meter rise (Hinze *et al.*, 2005; Bhattacharya *et al.*, 2006; Musset and Aftab, 2009; Kearey *et al.*, 2013).

2.3.4 Latitude Correction

According to the International Gravity Formula (1930), if the earth model is considered to be a simple spheroid, that approximates to the mean sea-level surface without the landmasses above the sea level. The theoretical gravity value (G_{theor}) at sea level on the surface of a spheroid, the geometric or mathematical reference surface would be about 978031.85 mGal according to Geodetic Reference System 1967 (Mariita and Keller, 2007). The variation of this value with latitude as computed from the international gravity formula (1903) and modified by the international union of geodesy and geophysics (Geodetic Reference System, 1967) is given by:

$$g_\phi = 978032.67715(1+0.0052970414(\sin \phi)^2+0.0000232718(\sin \phi)^4+0.0000001262(\sin \phi)^6) \text{ mGal} \quad (8)$$

Where ϕ is measured in radians. At the equator, the term in parenthesis reduces to 1 and $g_\phi = G_{\text{theor}}$.

From equation 8, the rate of gravity increase with latitude ϕ north or south of the equator is about 0.0142 mGal per km. In a gravity survey, stations located nearer the poles will have a higher gravity reading because of their geographic locations, and thus the correction would be negative (Hinze *et al.*, 2005). However, the correction will be positive for stations nearer the

equator than the base station. Due to gravity variation with the latitude, the correction was necessary for this gravity survey in the Paka volcano.

2.3.5 Free Air Correction (FAC)

During a gravity survey, the elevation of the gravity station varies considerably with the topography. This produces a significant variations in the observed gravity because of Newton's law of gravitation, which predicts that gravity varies with distance from the center of the earth (Parasnis, 1997; Kearey *et al.*, 2013). The vertical gradient of gravity is approximately 0.3086 mGal per meter and which is referred to as the free-air correction (equation 9) (Telford *et al.*, 1990; Blakely, 1996; Hinze *et al.*, 2005; Girdler, 2013).

$$\text{FAC} = 0.3086h \quad (9)$$

Where h is the elevation in meters, either concerning the ellipsoid or geoid (mean sea level) and the constant 0.3086 is the elevation height conversion constant. Gravity station elevation in the Paka volcano was determined using a DGPS. The value was then added to the latitude corrected gravity to obtain the free air corrected gravity at a particular station. Free-air anomaly (FAA) then calculated from the observed gravity value (G_{obs}) using the expression:

$$\text{FAA} = G_{\text{obs}} - g_{\emptyset} + 0.3086h \text{ mGals} \quad (10)$$

2.3.6 Bouguer Correction (BC)

The mass of rocks between a gravity station and a reference datum causes variations in gravity with elevation. Free air assumes lack of geologic materials (presence of air) between gravity station and the reference datum. The purpose of Bouguer correction is, therefore, to compensate for overcorrection by free air correction by replacing air with rock material (Hinze *et al.*, 2005; Kearey *et al.*, 2013). Traditionally it is calculated based on an infinite horizontal slab with the elevation h representing the vertical datum and the station;

$$\text{BC} = 2\pi G\rho h \quad (11)$$

Replacing the $G = 6.672 \times 10^{-11} \text{ m}^3 \cdot \text{Mg}^{-1} \cdot \text{s}^{-2}$, then the equation 10 reduces to

$$\text{BC} = 0.0419 \rho h, \text{ mGal} \quad (12)$$

Equation 12 is computed with a mean density for the spherical cap solid earth 2.67 g/cm³ (Hinze, 2003; Hinze *et al.*, 2005; Kearey *et al.*, 2013). Where ρ is the Bouguer density 2.67 g/cm³ and h is the height of station in meters relative to the ellipsoid or sea level. The expression in (12) could not account for the effect of the curvature of the earth. In this study, the revised

procedure was used to account for the effect of the curvature of the earth, where the horizontal slab equation was replaced with the closed-form formula for a spherical cap of radius 166.7 km (LaFehr, 1991) that is,

$$\delta g_{sc} = 2\pi G\rho(\mu h - \lambda R), \quad (13)$$

Where μ and λ are dimensionless coefficients defined by LaFehr (1991), R is the mean radius of the earth ($R_O + h$) at the station, R_O is the mean radius of the earth, h is the height above the ellipsoid and ρ is the density of the spherical cap. This gravitational effect of the spherical cap is smaller than the horizontal slab formulation because of the conventional truncation at 166.7 km and is larger because of the greater gravitational attraction resulting from the downward curvature of the slab as compared to the horizontal slab (Hinze, 2003; Hinze *et al.*, 2005).

The density used in calculating the Bouguer correction depends on the material making up the spherical cap. In a local survey, the density of the geological materials between the survey and the local vertical datum determines this value. However, in this study, a mean density used for the spherical cap was 2.67 g/cm³ for the solid earth (Hinze, 2003; Hinze *et al.*, 2005; Girdler, 2013). The residual after the process of gravity reduction have been eliminated is the Bouguer anomaly (BA).

$$BA = FAA - BC + G_{TC} = G_{obs} - G_\phi + FAC - BC + G_{TC} \quad (14)$$

Gravity data reduction and terrain corrections require knowledge of the average density of subsurface rocks that constitute the topographic relief of the surveyed area. Obtaining any plausible results for Bouguer anomaly, therefore, depends on the determination of the best average density possible for the rocks in an area of investigation (Simiyu and Keller, 2001). Simiyu and Keller (2001) and Mariita (2003) have used some approaches to determine the terrain density for the southern and northern Kenya rift valley respectively. Based on their results, they used a density of 2.55 g/cm³ for Bouguer and terrain corrections. Simiyu and Keller (2001) have, however, noted that use of the traditional Bouguer reduction density (2.67 g/cm³) would not have any significant effect on the resulting Bouguer anomaly. According to Hinze (2003) and Girdler (2013), a density value of 2.67 g/cm³ is generally assumed for the surface rocks of the continents that are crystalline and of granitic composition. The density of granitic rocks ranges from 2.5 to 2.8 g/cm³ with an average value of roughly 2.67 g/cm³.

In the present study, Bouguer and terrain corrections were determined using a terrain density of 2.67 g/cm^3 . This density value is consistent with Simiyu and Keller (2001), where the correct terrain density has the least correlation with topography. Figure (2.2) shows the variation of Bouguer anomaly with elevation in the Paka volcano. The linear line is the trend line, and from this graph, it is clear that Bouguer gravity has the low correlation with topography.

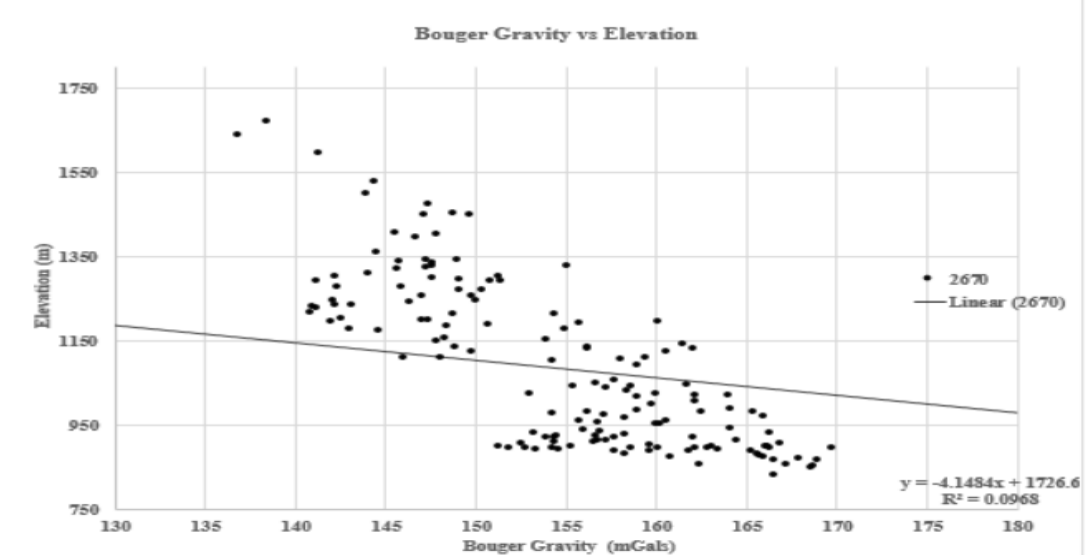


Figure 2.2: Variation of Bouguer anomaly with geoid elevation in Paka volcano

2.4 Datum

The geographic coordinates of gravity observation sites are given in units of the degree of longitude and latitude except for stations of local surveys in which the earth is assumed to be flat and horizontal distances between observations are measured in Cartesian coordinates. In minimizing errors arising from varying regional or national horizontal datum, the International Terrestrial Reference Frame (ITRF), in conjunction with the 1980 Geodetic Reference System (GRS80) ellipsoid, is used for the horizontal datum (Hinze, 2003; Hinze *et al.*, 2005; Mauri *et al.*, 2017). In this study, Arc 1960 datum was used in specifying the horizontal location in the DGPS, and the ITRF was in the coordinates system for the satellite altimeter-derived gravity data over the oceans (Waswa, 2017). Paka volcano was projected in a UTM zone 37N for gridding.

2.5 Gridding

Gridding is the process of interpolating data onto an equally spaced grid cell in a specified coordinate system such as x-y or longitude-latitude. These are several methods which

include minimum curvature, Bi-directional, Kriging, tinning, inverse distance weighting gridding, direct gridding, trend enforcement gridding among others (Jiang *et al.*, 2017; White *et al.*, 2017). Due to the nature of data collected over the Paka volcano, that were random data, non-parallel line data, Kriging as a method of interpolating data into an equally spaced grid was highly preferred.

2.5.1 Mathematical Aspect of Kriging

Kriging is a statistical gridding technique for random data, non-parallel line data or orthogonal line data or is a statistical local estimation technique that provides the best linear unbiased estimate of the unknown characteristic being studied. The nature of the measured gravity data that are poorly sampled and clustered, which facilitated the choice of the Kriging method (Chiao *et al.*, 2014; Jiang *et al.*, 2017; Shamsipour *et al.*, 2017; White *et al.*, 2017). For an ordinary Kriging, let $\{Z(x)\}$ be the data under the study, with the following expectation,

$$\{Z(x)\} = m, \quad (15)$$

A constant m , which is generally unknown or centered covariance,

$$\{Z(x + h) - Z\} = C(h); \quad (16)$$

Variogram

$$\{[Z(x + h) - Z(x)]^2\} = 2g(h); \quad (17)$$

An experimental data to be used consist of discrete values; $\{Z_\alpha | \alpha=1\dots n\}$, the linear estimate Z^*K considered is a linear combination of the n data values as follows:

$$Z^*K = \sum_{\alpha=1}^n \lambda_\alpha Z_\alpha \quad (18)$$

The weights are calculated to ensure that the estimate is unbiased and that the estimation variance is minimal (the estimation is then said to be optimal). This calculation provides a system of $(n + 1)$ linear equations in $(n + 1)$ unknown (the n weights and the Lagrange parameter m). Equation 18 is called the Kriging system.

$$\left\{ \begin{array}{l} \sum_{\beta=1}^{\sigma} \lambda_\beta \bar{C}(v_\alpha, v_\beta) - \mu = C(v_\alpha, V), \text{ for } \alpha = 1 \dots n \\ \sum_{\beta=1}^{\sigma} \lambda_\beta = 1 \end{array} \right\} \quad (19)$$

The minimum estimation variance, or Kriging, can be written as

$$(\sigma_k)^2 = E\{[Z_v - Z * K]^2\} = \bar{C}(v, V) + \mu - \sum_{\alpha=1}^n \lambda_\alpha \bar{C}(V_\alpha, V) \quad (20)$$

Kriging system (19) can be expressed in a matrix form as:

$$kw = d \quad (21)$$

$$\text{Where } k = \begin{bmatrix} \bar{C}_{11} & \dots & \bar{C}_{1x} & 1 \\ \vdots & \dots & \vdots & \vdots \\ \bar{C}_{1x} & \dots & \bar{C}_{xx} & 1 \\ 1 & \dots & 1 & 0 \end{bmatrix}, w = \begin{bmatrix} \lambda_1 \\ \vdots \\ \lambda_V \\ -\mu \end{bmatrix}, d = \begin{bmatrix} \bar{C} \\ \vdots \\ C_{x0} \\ 1 \end{bmatrix}$$

Where $\bar{C}_{(I=1..n, j=1..n)}$ is the covariance between unit vectors i and j; k is the covariance between i^{th} known location and the estimation location; w is the solution vector, which includes Kriging weights and the Lagrangian.

2.5.2 Kriging Overview Theory

Kriging is a geostatistical gridding technique for a random data, non-parallel line data or orthogonal line data (figure. 2.3). The method is only used if the data is variable between sample locations, known to be statistical, or poorly sampled or clustered.

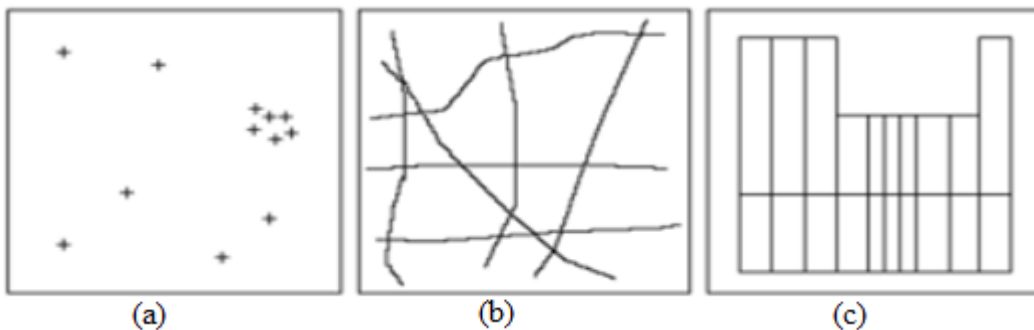


Figure 2.3: Geostatistical gridding technique for (a) random data, (b) non-parallel data and (c) orthogonal line data (Telford *et al.*, 1990; Parasnus, 1997; Kearey *et al.*, 2013)

Kriging is ideally suited to a geochemical or other geological and geophysical sample-based data in which they do not tend to follow a naturally smooth surface. Kriging first calculates a Variogram of the data showing the correlation of the data as a function of distance (Chiao *et al.*, 2014; Shamsipour *et al.*, 2017). The greater the distance between the data points, the greater the variation between the points. This technique uses the model to estimate the data values at the nodes of the grid. A significant by-product of Kriging is the ability to estimate the error of the data at each grid node (Martinez – Moreno *et al.*, 2014; Jiang *et al.*, 2017; White *et al.*, 2017). In this geophysical study, Geosoft Oasis Montaj software supports Kriging through the KRIGRID GX tool.

2.6 Geophysical Data Enhancement

This section looks at various ways of geophysical data enhancement that focuses mainly on gravity data by use of a range of linear and non-linear filter algorithms. The algorithms can selectively enhance the anomalies due to one group of geophysical sources relative to other

groups. Emphasis is on the principles behind the enhancements and usefulness of the enhancements in the interpretation of the data. After collection of gravity data from the field, several geophysical data corrections are applied to the data to produce profiles, contours and grid versions of ‘processed’ images like gravity Bouguer anomaly, residual anomaly and filtered grids (Mulwa *et al.*, 2011; Kearey *et al.*, 2013). It is, however, possible in many cases to apply various filtering and transformation processes to enhance the data and produce secondary products with improved visual information (Telford *et al.*, 1990).

2.6.1 Descriptive and Application of Linear Transformations (filters)

Filters are categorized into two broad categories: filters relying on the Fourier transform of the field and convolution. That is, filtering can be undertaken in the spatial frequency domain using the Fourier transform or in the space domain by convolution. Fourier transform techniques involve converting the data set into the frequency domain, operating on the data in the same way, and then returning it to the space domain. It allows different spatial frequencies (wavelengths) of the data to be highlighted or suppressed. This technique includes bandpass filter (whereby selected wavelengths of outside a specified band are removed), Derivative filters (a process for determining the first and second vertical derivatives of the data) and field continuation (a process that calculates what a field should look like if it were measured at a different height). Filters that attenuate short wavelength features are referred to as low-pass filters (removes near surface features), while filters that suppress long wavelength features are called high-pass filters (removes regional features) (An and Lu, 2013; Kearey *et al.*, 2013; Iwanaka, 2013; Boashash, 2015; Skowronek *et al.*, 2015; Durham, 2017).

Convolution methods involve convolving a filter impulse response $h(x, y)$ with the data $B(x, y)$. The filter impulse response has to be defined by the user, or it depends on the coefficient to be applied. A finite window is placed around the data points in question, selecting adjacent points in each direction. The size of the window determines how many samples are taken. The extracted data is then isolated to form a new data set (An and Lu, 2013). Convolution methods include: averaging or smoothing filters (where the entire data set is smoothed), sunlight Filters (where the data set is highlighted from a specific direction) and Edge-Detection Filters (where the boundaries in a certain direction are highlighted). If the conventional model is valid (i.e., a linear operation) then, each process can be done in each medium, but Fourier transforms are global operators and can't easily accommodate local variations in media properties (Telford *et al.*, 1990; Kearey *et al.*, 2013).

2.6.2 Fourier Transform Filters

In Geosoft Oasis Montaj software, it has MAGMAP tool that applies filters in the Fourier domain. The Fourier transform of a function $f(x, y)$ is an integral transform (Telford *et al.*, 1990; Blakely, 1996; An and Lu, 2013; Durham, 2017) and in two dimensions can be defined as follows:

$$F(u, v) = \int_{-\infty}^{\infty} \int_{-\infty}^{\infty} f(x, y) e^{-i(ux+vy)} dx dy \quad (22)$$

The inverse transform can, therefore, be defined as:

$$f(x, y) = \frac{1}{4\pi^2} \int_{-\infty}^{\infty} \int_{-\infty}^{\infty} F(u, v) e^{i(ux+vy)} du dv \quad (23)$$

Where u and v are wave numbers in the x and y directions respectively, measured in radians per meter and x and y are given in meters. A grid (in the space domain) is transformed to and from the wavenumber domain using Fast Fourier Transform (FFT). A Transform of the grid is composed of wavenumbers, which have units of cycles per meter and have real and imaginary components. A given potential field function in the space domain has a single and unique wavenumber domain function, and vice versa. The addition of two functions (anomalies) in the space domain is equivalent to the addition of their Transforms. The Fourier Transform of the potential field produced by a prismatic body has a broad spectrum whose peak location is a function of the depth to the prism's top and bottom surfaces, and whose magnitude is determined by the prism's density or magnetization. The peak wavenumber (ω') can be determined by the expression:

$$\omega' = \frac{i n \left(\frac{h_b}{h_t} \right)}{h_b - h_t} \quad (24)$$

Where ω' is the peak wavenumber in radians per meter h_t is the depth to the top, h_b is the depth to the bottom. The spectrum of a bottomless prism peak at the zero wavenumbers according to the following expression (Bhattacharya, 2006; Oldenburg and Pratt, 2007; Kearey *et al.*, 2013):

$$\ddot{f}(u, v) = e^{-hr} \quad (25)$$

$$r = \sqrt{(u^2 + v^2)} \quad (26)$$

Where h is the depth to the top of the prism. The spectrum of a prism with top and bottom surface is:

$$\ddot{f}(u, v) = e^{-h_t r} - e^{-h_b r} \quad (27)$$

Where h_t and h_b are depth to the top and bottom surface respectively. As the prism bottom is brought up, the peak moves to higher wavenumbers (Figure 2.4).

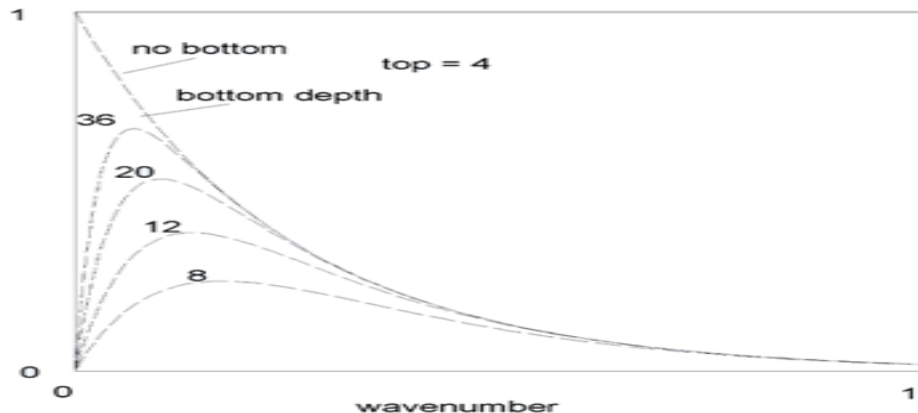


Figure 2.4: The spectrum of a prism with top and bottom (Telford *et al.*, 1990; Kearey *et al.*, 2013)

Considering the spectrum of a fixed size prism, as the prism depth is increased, the peak of the spectrum shifts to lower wave numbers (the anomaly becomes broader) and the magnitude of the spectrum is reduced (Figure 2.5).

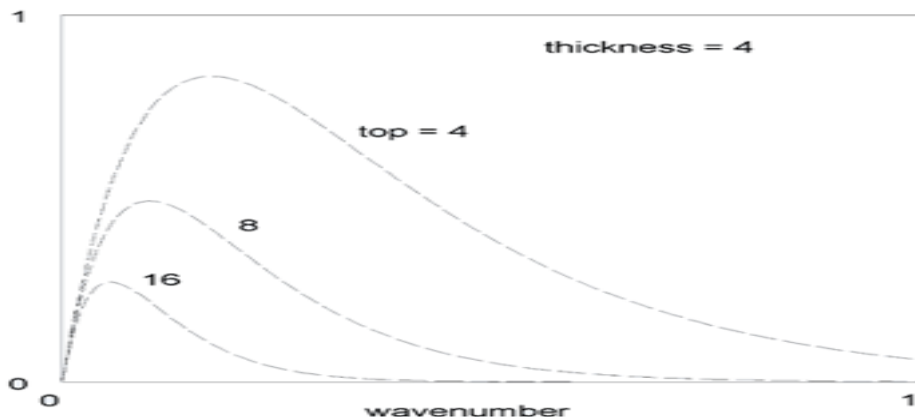


Figure 2.5: Spectrum shifted to a lower wavenumber as the prism depth increases (Kearey *et al.*, 2013)

From Figure (2.4 – 2.5), it is noted that the spectrum of a deep prism does not exceed the magnitude of the same prism at a lesser depth at any wavenumber; only the peak is shifted to lower wavenumbers. Due to this, wavenumbers filters cannot be used to separate the effect of deep sources from shallow sources of the same type. It can only be possible if the deep sources are of stronger magnitude, or if the shallow sources have a lesser depth extent. If the grid is so large enough to include many sources, then the log spectrum of the data can be interpreted to determine the statistical depth to the top of the sources using the relation:

$$\text{Log } E(r) = 4\pi h r \quad (28)$$

2.6.3 Convolution

Another way of filtering is by convolving the data set in the space domain with a set of filter coefficients whose frequency response (i.e. Fourier transforms) is the same as the desired amplitude and phase changes. This method is referred to as convolution (Milligan and Gunn, 1997; An and Lu, 2013). In the convolution method, data are filtered in the space domain using a moving window with an associated filter (2D impulse response), $w(x, y)$, which is convolved with the data, $D(x, y)$. The software, has a filter tool that provides several convolution filter confidence that includes 3×3 convolution, 5×5 symmetric convolution, 7×7 symmetric convolution, 9×9 symmetric convolution. A 3×3 -convolution filter removes the regional data treads from the data and produces a filtered curvature grid. Hanning filter is highly used to generate residual grids. The symmetric convolution is also known as smoothing or averaging filters. For potential field gradient tensor data, a smoothing (or averaging) filters enhance anomalies to best locate a source position (An and Lu, 2013; Bruna and Mallat, 2013; Srivastava and Buschman, 2013). They are the low-pass filter and hence removes short wavelength data, which is an ideal for data sets with much high-frequency noise. Relating the output $Y(t)$ to the input $X(t)$ in a time-invariant system through a convolution integral:

$$Y(t) = \int_{-\infty}^{\infty} X(u)g(t-u)du \quad (29)$$

Where $g(t)$ is a functional characteristic of the wave system. We say that Y is the convolution of X and g (fig 2.6), which we write as:

$$Y(t) = X(t) * g(t) \quad (30)$$

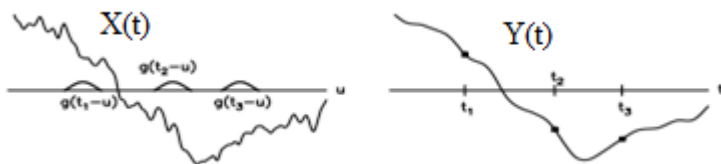


Figure 2.6: A graphical representation of convolution ((Telford *et al.*, 1990; Kearey *et al.*, 2013)

The left panel shows $x(t)$ an input and $y(t)$ an output. $Y(t)$ shows a system having free of regional and noise trends (Figure 2.6). For this research, a 3×3 convolution (Hanning) filter was used to remove the regional data trends by producing the curvature-filtered grid that was used to produce a residual grid.

2.6.4 Band pass Filters

It is a combination of high-pass and low-pass filters. It is whereby the selected wavelengths of outside a specified band are removed. If the main objective of a study is the large-scale crustal structure of the regional anomalies, then a low-pass filter is used to enhance regional anomalies (Simiyu and Keller, 1997, 2001; Mariita and Keller, 2007; Iwanaka, 2013; Skowronek *et al.*, 2015). Conversely, when investigating anomalies due to shallow crustal sources, the regional effect should be suppressed by high-pass filtering at the expense of enhancing high spatial frequency near surface features (Mariita and Keller, 2007; Iwanaka, 2013; Mulwa and Mariita, 2013; Skowronek *et al.*, 2015).

2.6.5 Upward and Downward Continuation

Continuation is the process of transforming data set so that it appears that it has been measured at a different height. If the data set is being moved away from the source, then its upward continuation and if the data set is being moved towards the source, then its downward continuation (Pawlowski, 1995; Ma *et al.*, 2013). Upward continuation removes a high spatial frequency noise and highlights regional features in a potential field data set (Figure 2.7). While downward continuation highlights subtle features, but at the expense of also highlighting any noise present in the data (Figure 2.8) (Telford *et al.*, 1990; Kearey *et al.*, 2013; Shako and Wamalwa, 2014).

This process of upward or downward continuation involves converting the data set into the Fourier domain by multiplying through by the term $e^{\pm 2\pi h\sqrt{(u^2 + v^2)}}$, where h is the new height, and u and v are the frequency domain variables (An and Lu, 2013; Kearey *et al.*, 2013; Boashash, 2015). This data is then converted back into the space domain for visual analysis. If h is positive, the process is called an upward continuation, if h is negative; the process is called a downward continuation.

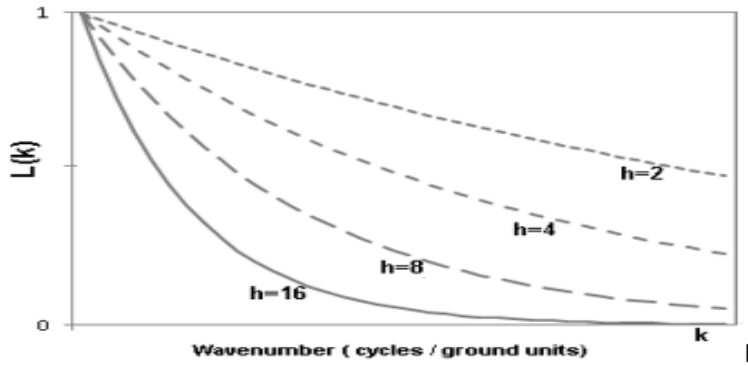


Figure 2.7: An upward continuation with highlighted regional features with low frequency and high wavelength (Telford *et al.*, 1990; Kearey *et al.*, 2013)

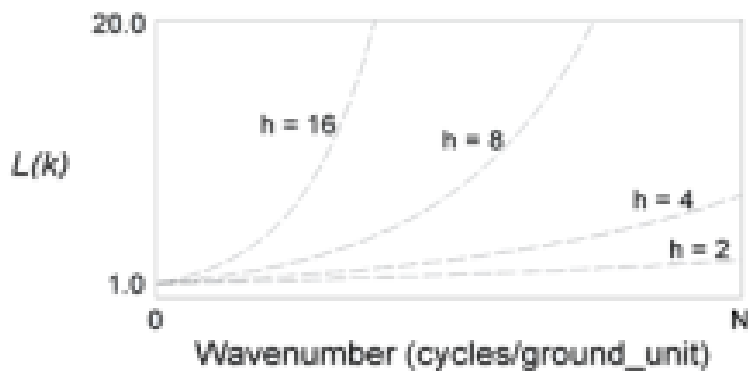


Figure 2.8: Downward continuation with highlighted near surface features and short wavelengths (Telford *et al.*, 1990; Kearey *et al.*, 2013)

2.7 Derivatives

2.7.1 Horizontal Derivatives or Horizontal Gradients (HG)

The methods are extensively used in locating the boundaries of density contrast from gravity data or pseudo gravity data (Fedi and Florio, 2001; Anudu *et al.*, 2014; Ma *et al.*, 2015; Yuan and Yu, 2015). The methods contend that the HG of the gravity anomaly caused by a tabular body tends to overlie the edges of the body if the edges are vertical and well separated from each other. The maxima of HG indicates the location of the faults or contacts. The greatest advantage of the HG methods is that it is less susceptible to noise in the data because it requires only the calculation of the two first-order horizontal derivatives of the field. The HG method is more robust in delineating both shallow and deep sources. The amplitude of the HG is expressed as:

$$HG = \sqrt{\left(\left(\frac{\partial g}{\partial x}\right)^2 + \left(\frac{\partial g}{\partial y}\right)^2\right)} \quad (31)$$

Where g is the gravity field, observed at (x, y) , $\frac{\partial g}{\partial x}$ and $\frac{\partial g}{\partial y}$ are the two horizontal derivatives of the gravity field in the x - and y - directions.

2.7.2 Tilt Derivative (TDR)

The tilt derivative TDR is also known as a tilt angle method, which is a refinement of the analytic signal method (Verduzco *et al.*, 2004; Anudu *et al.*, 2014; Ma *et al.*, 2015; Yuan and Yu, 2015). The TDR determines the location and depth of vertical magnetic contacts or high density contrast fault zone without the prior information on the source configuration by using the horizontal gradient amplitude (first horizontal derivative) of the tilt angle. The method was developed by Salem *et al.* (2007, 2008). The TDR method is used to enhance and sharpen the potential field anomalies. The advantage of the method is that it shows the zero contour line located on or close to contact or fault. The TDR is defined as:

$$TDR = \tan^{-1} \frac{\frac{\partial g}{\partial z}}{\sqrt{\left(\left(\frac{\partial g}{\partial x}\right)^2 + \left(\frac{\partial g}{\partial y}\right)^2\right)}} \quad (32)$$

Where g is the observed gravity field at (x, y) and $\frac{\partial g}{\partial x}$, $\frac{\partial g}{\partial y}$ and $\frac{\partial g}{\partial z}$ are the two horizontal and vertical derivatives of the potential field respectively. The derivative is restricted within the range $+\frac{\pi}{2}$ to $-\frac{\pi}{2}$.

2.7.3 Horizontal Derivative of the Tilt Derivative (HG-TDR)

A horizontal derivative of the tilt derivative is an edge detector method (Verduzco *et al.*, 2004; Anudu *et al.*, 2014). It is defined by:

$$HG-TDR = \sqrt{\left(\left(\frac{\partial_{TDR}}{\partial_x}\right)^2 + \left(\frac{\partial_{TDR}}{\partial_y}\right)^2\right)} \quad (33)$$

HG-TDR it is an independent of the geometric field and generates maximum values over the edges of the magnetized bodies or fault. The HG-TDR delineates model edges well (Chen *et al.*, 2014), as the amplitude peaks over magnetic sources, but the results for the deeper sources are not so effectively mapped (Arisoy and Dikmen, 2013).

2.7.4 Analytic Signal (AS)

The analytic signal technique is also known as total gradient method and has been the subject of continuing investigation and improvements since it was first applied (MacLeod *et al.*, 1993; Roest *et al.*, 1992; Hsu *et al.*, 1996; Debeglia and Corpel, 1997; Keating and

Pilkington, 2004; Dragomiretskiy and Zosso, 2014; Boashash, 2015). The method assumes that the causative sources are magnetic contact or a region having high-density contrast (fault zones). The general equation for 3D gravity source is defined as:

$$AS(x, y) = \sqrt{\left(\left(\frac{\partial g}{\partial x}\right)^2 + \left(\frac{\partial g}{\partial y}\right)^2 + \left(\frac{\partial g}{\partial z}\right)^2\right)} \quad (34)$$

Where $\frac{\partial g}{\partial x}$, $\frac{\partial g}{\partial y}$ and $\frac{\partial g}{\partial z}$ are the two horizontal and vertical derivatives of the gravity respectively.

The techniques have an ability to identify regions having high-density contrast. The higher values or maxima of analytic signal amplitudes indicates that the regions have a significant density contrast that produces an identifiable signature on the map (Dragomiretskiy and Zosso, 2014; Boashash, 2015; Yuan and Yu, 2015). The maxima of AS amplitudes produces a clear resolution for the shallower bodies (sources), but it does not delineate deeper bodies very well (Arisoy and Dikmen, 2013). The analytic signature of the Paka volcano was calculated in the frequency domain using the Fast Fourier Transform technique (Blakely, 1995).

2.8 Theoretical Aspects of Geophysical Modeling

The main objective of geophysical modeling is to construct a sensible geologic model that satisfies all the geological and geophysical constraints simultaneously (Longo *et al.*, 2016). Constrained computer modeling of a potential field data provides a particularly useful means to integrate independent geophysical and geological constraints to derive a clear picture of geological structure (Simiyu and Keller, 1997; Oldenburg and Pratt, 2007; Mulwa and Mariita, 2013; Longo *et al.*, 2016). In exploration, geophysical inversion usually means producing an earth model, which is in agreement with geophysical survey data, in a timely and cost-effective manner (Roy *et al.*, 2017). Earth modeling is a process used to find the distribution of a physical property that caused a set of physical measurements recorded in a field survey. Modeling enables an explorer to extract more insight from geophysical measurements into images of the subsurface that can be integrated with other surface and subsurface geological observation (Simiyu and Keller, 1997; Mulwa and Mariita, 2013; Longo *et al.*, 2016; Strom, 2018). The earth model must conform to other geophysical and geological investigations in the surveyed area.

According to Oldenburg and Pratt (2007), the inversion is divided into three categories;
 Type I – Discrete body inversion where a few parameters are sought.
 Type II – Pure property inversion where a voxel (cell) representation of the earth is invoked.

Type III – Lithological inversion where the earth is characterized by specific rocks.

In an inversion problem, as per Oldenburg and Pratt (2007), it is provided with observations, some estimates of their uncertainties, and relationship that enables the computation of the predicted data for any model. The model represents the spatial distribution of a physical property such as density contrast, susceptibility or conductivity.

2.8.1 Geophysical Data Modeling

There are two methods of modeling geophysical data, namely forward modeling and inversion modeling. Each of these methods attempts to determine the model parameters such as depth, thickness, density and orientation of the anomaly in the model (Oldenburg and Pratt, 2007; Mulwa and Mariita, 2013, 2015; Longo *et al.*, 2016).

2.8.2 Forward Modeling

Forward modeling (also referred to as the forward problem) is the process of computing a response from a given earth model (Mulwa and Mariita, 2013, 2015; Longo *et al.*, 2016; Strom, 2018). It assumes a priori information such as mass and calculates the corresponding anomaly. The most important geological units and structures are brought into the forward model to ensure a realistic model. The calculated anomaly is in turn compared to the measured anomaly, and the model is manipulated (modifications to the model is performed interactively) until the calculated anomaly mimics/coincides the observed anomaly to an acceptable degree (Oldenburg and Pratt, 2007; Richarte *et al.*, 2018).

2.8.3 Inverse Modeling

The inverse problem is complementary to forward modeling. It helps in determining the distribution of physical properties that yields the measured field response in a best way (Oldenburg and Pratt, 2007; Mariani *et al.*, 2013; Oruc *et al.*, 2013; De Castro *et al.*, 2014; Dossing *et al.*, 2014; Longo *et al.*, 2016). The method requires ‘starter model’ that has an incorporated prior information on the source body, which is given in, by a forward model. The method computes the model parameters directly from the measurements, however, many model creates the same surface response, which results to non-uniqueness (Richarte *et al.*, 2018). To reduce the non-uniqueness, a priori information that is incorporated into starter model constraints the model, which reduces the uncertainties in data interpretation.

2.8.4 VOXI Earth Modeling (Inversion Software) Theory

VOXI Earth Modeling is a geophysical inversion tool in Oasis Montaj software that generates 3D voxel models from gravity data using cloud-computing (Longo *et al.*, 2016). The utility of potential data in many areas of geophysical exploration is as well-known as the application of 3D voxel inversion to aid gravity data interpretation. The inversion process in VOXI Earth modeling software can be explained starting with the forward and inverse problem represented by the following equations:

$$G(m) = d \quad \text{forward problem} \quad (35)$$

$$G^{-1}(m) = d \quad \text{inverse problem} \quad (36)$$

Where G is a geophysical phenomenon, m is the earth model, and d is the geophysical data. However G^{-1} does not exist, therefore the inversion problem becomes one of optimizing the closeness of the predicted model and its forward calculated response to what it's observed and what's assumed in the model look like (Mariani *et al.*, 2013; Oruc *et al.*, 2013; De Castro *et al.*, 2014; Dossing *et al.*, 2014; Longo *et al.*, 2016; Richarte *et al.*, 2018; Strom, 2018). In VOXI, the idea is to quantify the closeness between the predicted model response and the observed data using the data misfit equation:

$$\varphi_d = \frac{1}{N} \sum_{i=1}^N \left(\frac{d^{obs} - d^{pre}}{\delta_d} \right)^2 \quad (37)$$

Where φ_d is the data misfit, N is the number of observations, d^{obs} is the observed geophysical data, d^{pre} is the predicted model response and δ_d is the error. It is possible to also quantify how closely the predicted model is to the preferred reference model with the model norm equation for M voxels:

$$\varphi_m = \frac{1}{M} \sum_{i=1}^M \left(\frac{m^{ref} - m^{pre}}{\delta_m} \right)^2 \quad (38)$$

Where φ_m is the model norm, M is the number of voxels, m^{ref} is the reference earth model, m^{pre} is the predicted model and δ_m is the error. When the confidence in the reference model is high, $\varphi_m \approx 0$, it means it conforms to geology. From a geophysical inversion, it is shown that:

$\varphi_d \approx 1$ In agreement with survey data

$\varphi_m \rightarrow 0$ Earth model conforms to geology

An inversion process seeks a model that satisfies both the observed data and the known geology. Therefore inversion seeks to balance these two quantities before arriving at the final model. An objective function can balance the two quantities:

$$\varphi_T = \varphi_d + \lambda \varphi_m \quad (39)$$

Where φ_T is the total objective function, φ_d is the data misfit, φ_m is the model norm with regularization parameter λ that is adjusted by the inversion algorithm in successive steps. During each step of the calculation, the inversion tries to find a model that minimizes the objective function so that the data misfit $\varphi_d \approx 1$

VOXI inversion tries to solve this problem numerically (Minimize $\varphi_T = \varphi_d + \lambda \varphi_m$ and where choose λ so that $\varphi_d \approx 1$), where the earth volume is divided into a number of cubic cells, each of which has a constant, but unknown value of the physical property. The model objective function and forward modelling equations are discretized using the gridded earth volume and the total objective function minimized (Pilkington, 1997). When the total objective function is minimized for a specific, λ it produces a model that has quantifiable and model norm. When the optimization is carried out for many values of λ the results of these step calculations can be plotted to produce a Tikhonov, or trade-off curve (Figure. 2.9)

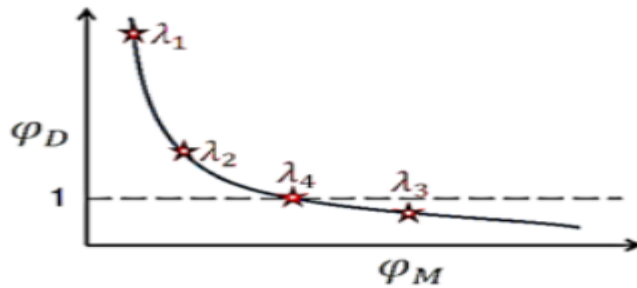


Figure 2.9: Tikhonov curve showing how optimisation is carried out for the values of λ (Telford *et al.*, 1990; Kearey *et al.*, 2013)

In this process, λ represents an iteration in the inversion process. The final model is the one that minimizes the objective function with the condition specified above, that is the data misfit $\varphi_d \approx 1$.

According to Oldenburg and Pratt (2007), the left-hand side of the curve in (Figure. 2.9) corresponds to large λ and the significant decrease can be obtained in the misfit without greatly increasing the model norm φ_m . The area under the curve fits the geophysical signal. But on the right-hand portion of the curve, the model norm (structure) increases significantly with only a small decrease in misfit thus in this realm fitting the noise. Therefore, the best fit can be obtained somewhere near the kink of this curve (between λ_2 and λ_4).

2.9 Tectonic and Geology of Paka prospect

Paka is composed of trachytic and basaltic lavas and pyroclastic deposits. Sceal (1974) first described its geology, and William *et al.* (1984) summarised it in reviews. The evolutionary history of Paka volcano was broadly separated into two periods of trachytic volcanism separated by basaltic activity and faulting. The early history of Paka volcano was uncertain as the older shield forming lavas are mantled by trachytic pyroclastic deposits which covers much of the northern, western and southern flanks of the volcano (Baker and Wohlenberg, 1971; Sceal, 1974, Smith and Mosley, 1993). Dissection of these deposits has produced a radial drainage pattern and irregular topography of gullies and ridges densely vegetated by acacia and grass. The summit and the upper flanks of Paka volcano are characterized by the short trachyte flow that can be discerned beneath the mantle of younger pyroclastic deposits. Basalt lavas erupted from fissures and cones located along N-trending fractures on the northern and southern flanks, and contemporaneous normal faulting led to the formation of N-trending linear zone of the rifting that extended down the northern flanks (Dunkley *et al.*, 1993).

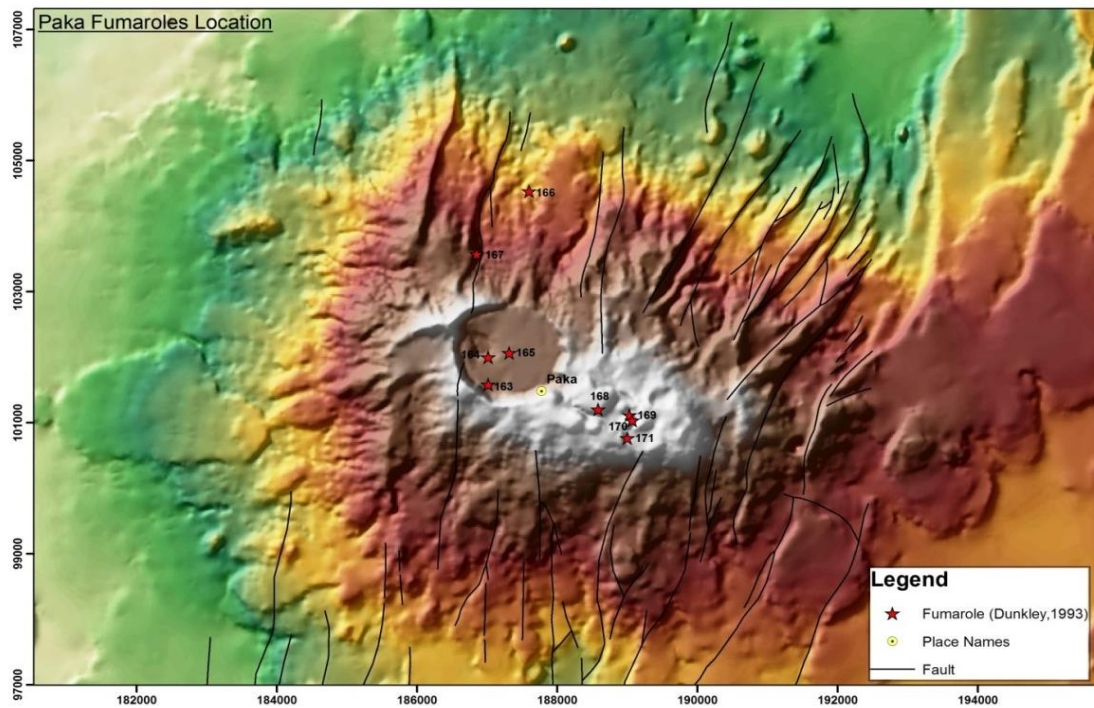


Figure 2.10: Location of fumaroles, crater, and faults in Paka volcano (Dunkley *et al.*, 1993)

The rift zones are defined by a set of faults systems, the eastern and western boundary faults (fig 2.10) that controlled the dispersion of lava and pyroclastic flows during the final

stages of eruption and caldera collapse, and constrain the geothermal activity of Paka. Trachyte and basalt lavas erupted in the caldera and flowed out through a breach and down the northern flanks (Prodehl *et al.*, 1994, 1997). Paka volcano is surrounded by some smaller volcanic centers, which are linked to the main volcano by linear zones of basalt and trachyte cones and eruptive fissures. The activities of these centers are considered to have been broadly contemporaneous with that of Paka. In the south, at Adomeyan faulted trachyte lavas flows erupted from N-trending fissure zones extending between Paka and Korosi (Smith and Mosley, 1993).

The summit area of Paka is dominated by some craters and small caldera, which is aligned in a northwesterly direction. The caldera is circular in plan with a diameter of 1.5 km, has vertical walls up 120 m high, and is breached on its northern side. To the southeast, there is a second larger crater, in which Sceal (1974) named it as the “explosion crater” that refers to the eastern crater. The eastern crater measures 1 km by 0.5 km and has degraded trachyte pumice cone, which forms a ridge across the Centre effectively splitting the crater into two. An older crater along axis trending NNE is also present to the west of the main caldera and exposes sections through stratified pumice-rich breccias and lapilli deposits, and other old crater features also occur to the south-west of the eastern crater. The deposits are well exposed in the caldera walls where they overlie a thick sequence of trachyte lavas and lithic breccias. They consist predominantly of stratified pumice lapilli tuffs interbedded with poorly sorted polymitic agglomerate and a meter in size.

The tectonic activities that characterize Paka are dominated by zones of intense normal faulting and fissuring that are located on the eastern and northern flanks. This fault extends northwards onto Silali and southwards to Korosi figure 2.10 (Baker and Wohlenberg, 1971; Sceal, 1974; Truckle, 1977; Smith and Mosley, 1993). In contrast, there is no evidence for faulting nor fissuring to the west of Paka on the Natan plains. Extensive faulting accompanied by block tilting characterizes the terrain and these form numerous N-S ridges and fault scarps (Connor *et al.*, 2000). According to Baker and Wohlenberg (1971), Baker *et al.*, (1972, 1988), and Baker (1986), this complex network of faults and fractures suggests that tensional strain oblique to the primary rift axis is still occurring.

2.10 Physiography of the Inner Trough of Paka Volcano

In the northern Kenya rift, the regional topography between Lake Baringo and Emuruangogolak is marked with westerly tilt. Specifically, the inner trough of Paka volcano is

marked with northward gradient. Due to northward gradient that exist in the northern Kenya rift, it has resulted for the local rivers like Komoi River to flows from east to west between Korosi and Paka and it drops 300 m across the rift floor. Similarly, Amaya River falls 200 m across the rift floor of the trough between Paka and Silali. Nginyang' river flows northward in the western side of Paka volcano. The northerly and westerly gradient in the rift floor results in an overall north-westerly tilt vector. Elgeyo escarpment on the western and Laikipia escarpment (plateau) in the eastern are the main feeder or recharge of the Paka volcano (Lagat *et al.*, 2007). All this rivers flows to Lake Alablab and Lake Logipi in the north of Namarunu volcano (Dunkley *et al.*, 1993). This networked rivers provides re-ejection of surface meteoric water into deeper fractured fault zones under Paka volcano (Kipng'ok and Nyamongo, 2013).

2.11 Previous Geophysical Studies

2.11.1 Gravity Studies

Over the last several decades from the 1970s, some geophysical investigations, models have been undertaken and reported about the East African rift system. Searle (1970) surveyed the Kenya rift from Menengai to the south covering Longonot and Suswa volcanoes prospects. The survey indicated that the axial gravity high continues, but varies in width and amplitude. He explained the anomaly regarding a dense mantle-derived intrusion 20 km wide extending from a depth of 20 km to width 6 km of the Rift floor, thus representing extreme thinning of the lithospheric plate. Baker and Wohlenberg (1971) presented a similar interpretation for a long wavelength, roughly equatorial profile through the southern part of Baringo but with narrower 10 km intrusion in the crust and a wedge-shaped low-density zone in the upper mantle for the broad negative Bouguer in the Rift valley. Fairhead (1976) showed that most of the Kenya rift is characterized by a dominant gravity 'low' some 350 km wide and - 50 mGal in amplitude and a superimposed central 'high' about 55 km wide and +20 mGal amplitude.

In the 1990s, Kenyan rift was a target of some geophysical and geological investigations, especially the southern rift as compared to the northern rift for the regional tectonic evolution of rift, lithospheric analysis, and geothermal exploration. The results of these investigations are summarised in three collections of papers (Prodehl *et al.*, 1994, 1997; Morley, 1999). Regional seismic and gravity studies based on the results of the KRISP that provided many new constraints on the lithospheric structure and revealed significant differences between the northern and southern parts of the Kenya Rift. For example, Bouguer gravity anomaly values increased by 200 mGal towards the Lake Turkana region, but are

mostly due to crustal thinning (Mechie *et al.*, 1994). As one progresses northward toward Lake Turkana, these changes in deep structure are accompanied by a gradual decrease in the elevation of the rift valley floor and an increase in width of the rift valley (Keller *et al.*, 1994).

The regional Bouguer gravity data covering the central and southern Kenya rift indicate that all the major volcanic centers (e.g., Menengai, Eburru, Olkaria and Suswa) are associated with positive gravity anomalies superimposed on the regional gravity low. Modeling this broad gravity low using KRSIP and seismic result as constraints, Swain (1992) and Simiyu and Keller (1997, 2001) revealed gravity low were due to less dense mantle under the Kenya dome. The gravity highs were modeled and interpreted as resulting from the volcanic centers underlain by discrete mafic bodies. Also, axial gravity high can be explained as resulting from densification of the basement by dike intrusions (Young *et al.*, 1991; Tongue, 1992; Tongue *et al.*, 1992, 1994; Swain, 1992). Also, the other element of the positive axial gravity was due to an intra-rift host block (Precambrian basement) that extends along the axis of most of the rift valley (Simiyu and Keller, 2001). Mariita and Keller (2007) extended the results of Simiyu and Keller (2001) to the north (from Menengai to Lake Turkana) at regional analyses. As observed by previous studies done in the southern rift, Mariita and Keller (2007) explained the gravity high observed along the rift axis as due to mafic bodies associated with the main volcanic centers or due to densification of the upper crust as diking or as host blocks when Precambrian basement has been brought near the surface.

Recently, the Kenya rift lithospheric structure was revisited based on regional 3D gravity modeling (Sippel *et al.*, 2017). The study indicated an overall trend of increasing mean crustal densities from mainly less than 2880 kgm^{-3} in Western Kenya to more than 2880 kgm^{-3} in the eastern Kenya, which implies the crustal temperature is decreasing from the Kenya rift in the west to eastern Kenya while the integrated strength of the lithosphere increases. The study generally explained the positive gravity anomaly in Kenya rift crustal at the regional analysis $> 10 \text{ km}$ as due to magnesium and iron rich mafic intrusions. While the gravity ‘low’ in the northern Kenya rift was explained as due to positive thermal anomalies within the crust, involving partial melting/or rock expansion which strongly weakens the lithosphere. However, thermal effect decreases towards the south rift due to narrowing of the plume beneath the floor (Sippel *et al.*, 2017).

2.11.2 Resistivity Studies

Magnetotelluric studies by Rooney and Hutton (1977) showed that a low resistivity anomaly $\rho_a \approx 2\text{-}20 \Omega\text{m}$ at shallow depths ($< 8 \text{ km}$) exists along the Kenya rift, including Paka volcano. According to Rooney and Hutton (1977), the low resistivity anomaly is probably due to high temperature and water saturation. Hautot *et al.* (2000) have identified a thick succession of well-defined tectonic stratigraphic units in north rift portion including Paka volcano and downward continuous layer. Many electrical or electromagnetic geophysical investigations done along the Kenyan rift potential prospects indicates an existence of the shallow magma body at depth $< 6 \text{ km}$. Magnetotelluric (MT) resistivity shows an existence of a conductive body directly below the Paka massif volcano and on the eastern side at foot scarp depth of about 3 km (Omenda, 2007). The iso-resistivity maps at shallow depth 600 m.a.s.l indicated the extensive of low resistivity alluvial formation covering all valley and lower slopes of the Paka massive (Mulwa and Mariita, 2013, 2015; Wamalwa and Serpa, 2013; Wamalwa *et al.*, 2013; Abdelfettah *et al.*, 2016). But the conceptual model developed by JICA (2010), shows that geothermal activities in Paka volcano are driven by a heat source at depth centred below the summit crater and extends to the east. Lichoro *et al.* (2017) extended most of the regional resistivity studies to the resistivity imaging of Korosi, Paka and Silali prospects based on the joint inversion of Magnetotelluric and Transient electromagnetic TEM. The study revealed a resistivity pattern consistent with the existence of several geothermal systems within the prospects. The resistive $100\text{-}\Omega\text{m}$ surficial layer is overlying $\approx 10 \Omega\text{m}$ low resistive zones interpreted as the hydrothermally altered clay cap of the system at a depth less than 1 km. A higher resistivity zone of about $60 \Omega\text{m}$ at about 1 km interpreted as a potential high-temperature alteration zone and a trend of moderate-high resistivity at the depth of the potential reservoir corresponds to the zone of intense faulting and fracturing.

2.11.3 Seismic Studies

Most studies have shown that massive intrusions are associated with high levels of (earthquake activities) seismic events (Tongue, 1992; Tongue *et al.*, 1992, 1994). In a geothermal environment or volcanic setting, seismicity events are associated with fluid movement (Mulwa *et al.*, 2014; Simiyu, 2013). For example, Olkaria field in southern Kenyan rift, seismic hypocenter shallow events have been observed at about 2.3 km near Ololbutot fault zone and the deepest events at a depth that do not exceed 6 km (Simiyu and Keller, 2000). Simiyu and Keller (2000, 2001), Mulwa and Mariita (2013), Mulwa *et al.* (2014), and Omenda

and Simiyu (2015) seismology studies along the rift prospects have indicated attenuation of the seismic local wave at depth < 6 km due to a hot fluid circulation at local depth. Patlan *et al.* (2017) extended the Simiyu and Keller (2000, 2001) and Mulwa *et al.* (2014) regional seismic studies at regional ($5 - 40$ km) and teleseismic (> 40 km) events to local events < 6 km at Menengai, Paka and Silali. A swarm of seismicity was detected beneath Paka volcano at depth $0 - 6$ km and a low shear wave velocity anomaly identified east of the flank of Paka at depth $3 - 6$ km. The low shear wave velocity anomaly to the east of the massive volcanic centre was viewed as due to the hot deep fluid to a shallow depth that was evidenced of active hot grounds and fumaroles.

2.11.4 Summary

Kenya rift system has been studied, for example Smith (1994) indicated a strong coincidence of location of magmatic activity and rifting with pre-existing zones of crustal weakness beneath the Kenya rift. Simiyu and Keller (1997), delineated the major regional tectonic feature that probably predates the Kenya plateau uplift. The variation in crustal thickness from about 35 km around Lake Magadi in the south to 20 km in the north at Lake Turkana and this was explained as due to northward increase in extensional force that exist on the upper crust (Keller *et al.*, 1994). Which implied that Lake Magadi and Lake Turkana area are situated on a different crustal thickness. Simiyu and Keller (2001) modeled the gravity highs of the southern rift and interpreted as resulting from volcanic centres. Mariita and Keller (2007) extended Simiyu and Keller (2001) studies to the northern rift and made a similar observation. The local analysis for the key geothermal concealed structural features like heat sources inform of dikes and shallow faults that are significant have remained relatively poorly constrained. Hence, the key concealed structural features at local analysis heat sources in form of dikes and shallow faults have not been mapped at regional scale. The study is an advancement of the earlier studies carried out at a regional analysis in northern Kenya rift to a detailed local analysis < 5 Km in Paka volcano. The study ought to improve and bring out new information on the subsurface density distribution patterns that can be used to explain the local structural features in the Paka volcano.

CHAPTER THREE

MATERIALS AND METHODS

3.1 The Study Area

The gravity survey was carried out in Paka volcano that is situated approximately 25 km north of Lake Baringo and 15 km east of the Nginyang' village at $00^{\circ} 25' N$ and $36^{\circ} 12' E$. The volcano lies in the inner trough of the Kenya Rift and its volcano massif extends over an area of about 280 km^2 and rises between 600 - 700 m above the rift floor (Dunkley *et al.*, 1993; Lagat *et al.*, 2007; Kanda *et al.*, 2011; Girdler, 2013; Lichoro *et al.*, 2017; Waswa, 2017) (Figure 3.1). The central volcano (Paka) rises to a height of 1697 m, and is surrounded by plains to the south, west and east. At the summit, the well-preserved caldera is about 1.5 km in diameter and is filled with young basaltic flows. The surface is rocky and rugged, covered by a low bush and shrubs (Lichoro *et al.*, 2017; Waswa, 2017).

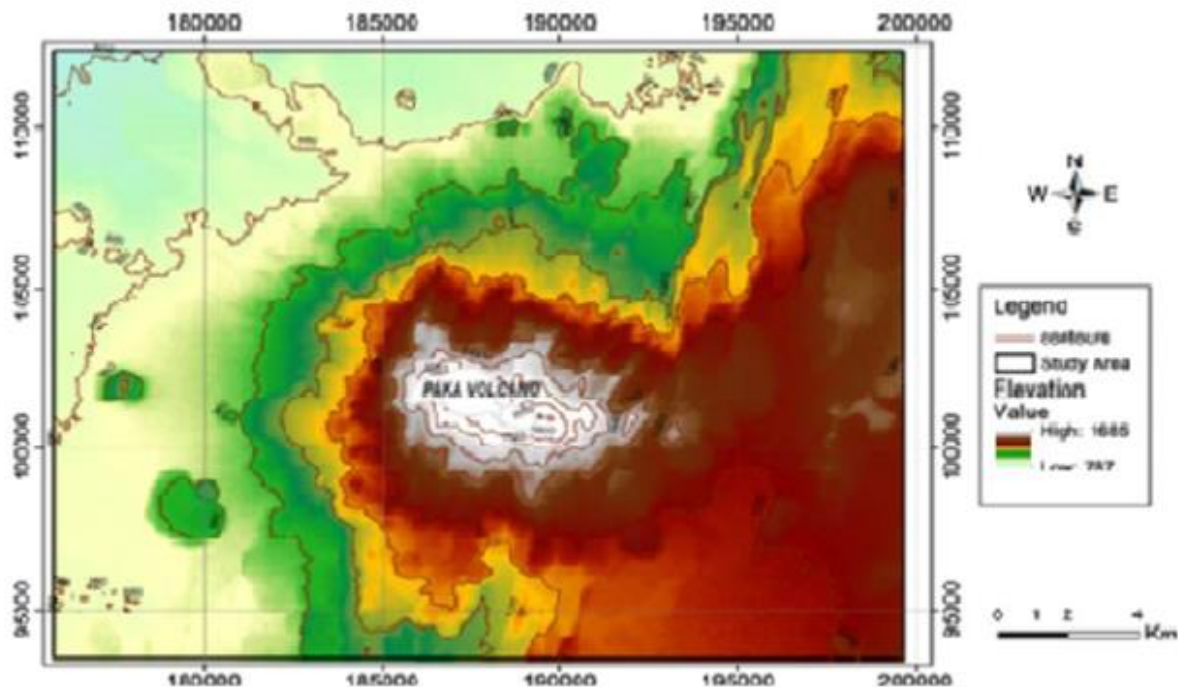


Figure 3.1: The Elevation of Paka Volcano Mountain in the Kenya rift valley (Waswa, 2017)

3.2 Materials for Gravity Data Collection and Processing

In this study of Paka volcano, the following instruments were used during the field survey which includes CG-5 Autograv model type gravimeter and Trimble R8 GRSS model type DGPS. The gravimeter was used to measure the vertical component of the observed gravitational attraction to a reading resolution of 0.001 mGal while the DGPS was used to

obtain the location of each station, i.e., elevation, latitude and longitude (Grid Easting and Grid Northing) to a reading resolution of 5mm. In data reduction, exploration gravity survey quality assurance spreadsheet was used to check for the correlation between topographical elevation and Bouguer anomaly (Nyakundi, 2017). Geosoft Oasis Montaj version 8.5 software provided a platform for all data processing. Several tools in Oasis software which includes GX, database tools, grid and image, VOXI, map tools and Magmap; were mainly for signal data anomaly enhancement (Richarte *et al.*, 2018; Strom, 2018).

3.3 Survey Design and Field Operations

Gravity data collected in the Paka volcano, a total of 156 gravity stations were distributed to cover the Paka prospect area (Figure 3.2).

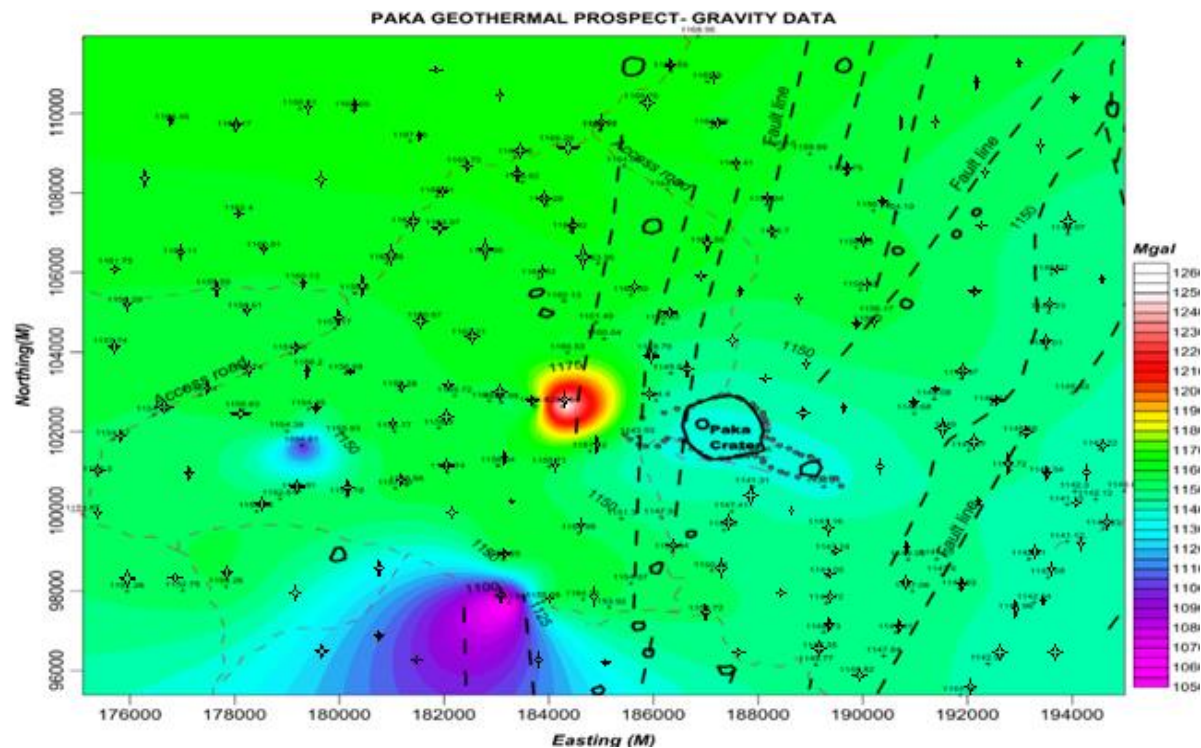


Figure 3.2: Gravity data coverage of Paka volcano showing gravity data locations

The observed gravity readings were taken using the gravimeter. All the field data readings were tied to a primary base station at *Kambi ya samaki* junction in Baringo for drift and tidal correction since we were residing at *Kambi ya samaki*, which was in turn tied to Nairobi International Base Station IGSN71 having a gravity value of 9775260.7 in *situ*/gravity unity (Mariita and Keller, 2007; Nyakundi, 2017). Before the gravity survey began, gravity meter drift and tidal effects were determined at *Kambi ya samaki* junction (as the primary base station). The gravity readings at the primary base station were taken twice a day for drift and

tidal effect correction. In the surveyed area, gravity readings were taken in the whole day from 9.00 am to 4.30 pm since the region is not prone to traffic ground vibrations, which normally affects the gravity readings.

Due to the poor terrain in Paka prospect, most of gravity straight line profile and equally spaced gravity stations were not taken into account. However, the gravity station locations were randomly located to cover the Paka volcano (Figure 3.2). The gravity readings obtained showed a small variation per hour, which indicated a low value of gravity meter drift and tidal effects. The small gravity meter drift value variation was within the required limits of accuracy and could, therefore, be tolerated. In this study, the gravimeter was set up to take the average of six reading per minute. Also, the measurement was not accepted unless it had very small standard deviation and the tilt in both x (Eastings) and y (Northings). Going by this procedure, it allowed quality and consistency in the gravity data and served to filter out readings with a lot of noise (data with high standard deviation and the tilt) (Nyakundi, 2017; Khazri and Gabtni, 2018). The station locations (latitude and longitude) and elevation were determined using DGPS receiver (Figure 3.3) (Mauri *et al.*, 2017).



Figure 3.3: Gravity measurement being taken in the field using a gravimeter and DGPS receiver.

3.4 Developing Bouguer Anomaly Map

3.4.1 Gravity Data Pre-Processing (Data Reduction)

Raw gravity data was reduced to Bouguer anomaly using a traditionally Bouguer density 2.67g/cm^3 and sea level as datum, then it was adjusted to a common IGSN71 having a gravity value of 9775260.7 *in situ* (gravity datum) before being processed in Geosoft software (Hinze, 2003; Simiyu and Keller 2001; Mariita and Keller 2007). These gravity reductions included tide and drift corrections for computing the absolute gravity, reductions accounting for the flattening of the earth (latitude), free air correction, terrain correction and Bouguer correction. All the reductions were based on section 2.4 of this thesis. After data reduction, it was saved in an excel sheet as CSV.

3.4.2 Setting the Projected Coordinate System of Paka Geothermal Prospect

For the gravity data to be processed in Geosoft Oasis Montaj software, the coordinate system must be projected to the Geographic Earth Coordinate System for gridding and mapping (Mauri *et al.*, 2017; Nyakundi, 2017). In this study, Arc 1960 datum was used in specifying the horizontal location in the DGPS, and the ITRF was in the coordinates system for the satellite altimetry-derived gravity data over the oceans and Paka volcano was projected in a UTM zone 37N for gridding in Oasis Montaj software.

3.4.3 Gridding

The distribution of gravity stations in the study area that had highly variable between sample locations, poorly sampled and clustered, it facilitated the use of the Kriging method.

3.4.4 Kriging of Bouguer Channel

With the aid of Geosoft Oasis Montaj software, Bouguer channel was gridded at the grid cell size of 400 to give the Bouguer anomaly grid (Figure 3.4). The grid cell size of 400 gives an anomalies with increased visually based on this data. The Bouguer anomaly grid had a positive amplitude of more than 100 mGal at the contour interval of 100.

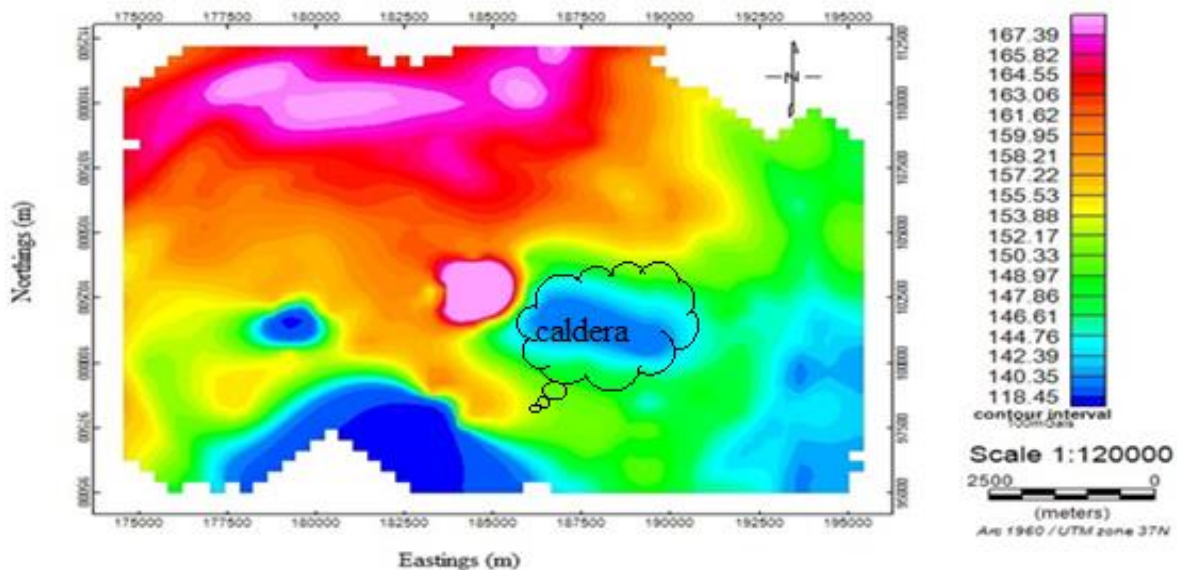


Figure 3.4: Total Bouguer anomaly grid after Kriging

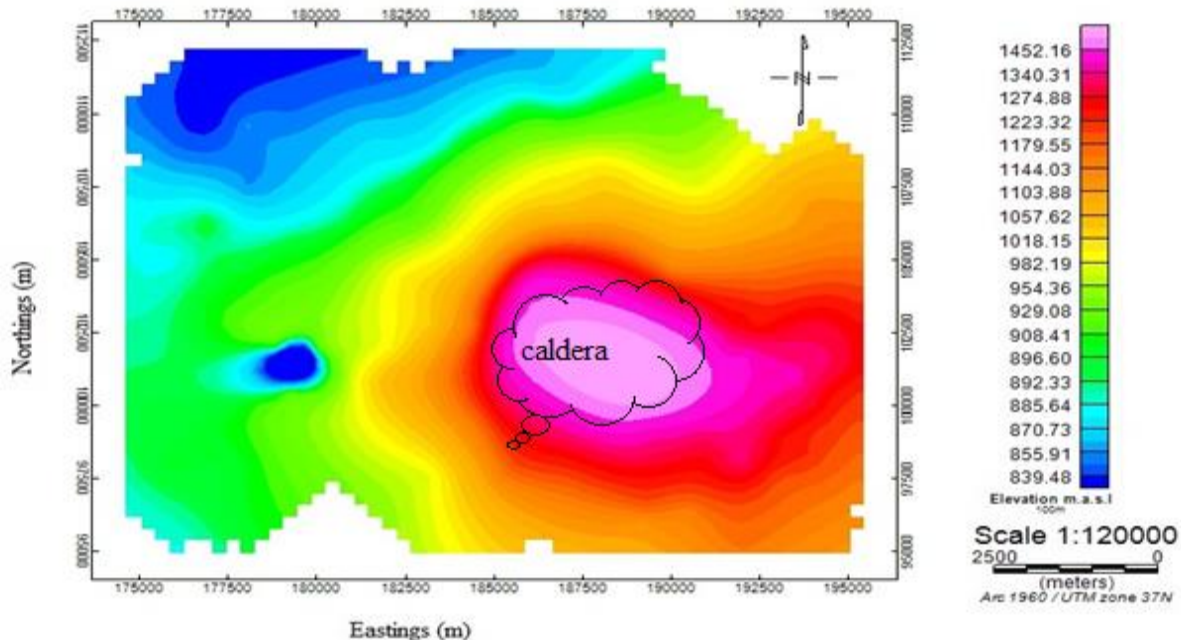


Figure 3.5: Elevation grid of Paka area.

3.4.5 Kriging of Elevation Channel

An elevation channel was gridded under Oasis Montaj software in Geosoft to generate the elevation grid with grid cell size of 400 (Figure 3.5). The grid indicated the elevation of Paka prospect area. The elevation grid was used in generating the DEM grid during VOXI inversion.

3.4.6 Filtering

Filters emphasize the boundaries between geological units through highlighting deeper and shallow structures, or showing features from different angles (Telford *et al.*, 1990). It was applied to the potential gravity field data after the data collection and reduction into a standard format (Bouguer gravity).

3.4.7 Floating Grid

The pre-processed total Bouguer grid was transformed by MAGMAP filters in the 2D Fast Fourier Transform FFT (in the space domain) to and from a wavenumber domain using FFT to produce a floating grid. This grid was used to generate different Bouguer anomaly maps when subjected to different bandpass and upward continuation filters. The floating grid still contains all information in the space domain, and it is where the filters are defined (Durham, 2017).

3.4.8 Generating Gravity Bouguer Anomaly Maps using the Step-By-Step Filtering

Two filters were defined on the floating grid, then projected onto the original total Bouguer grid to generate the Bouguer grids. A band-pass filter was defined as filter one and upward continuation as filter two. For a band-pass filter, long wavelength cutoff and short wavelength were defined, i.e., long wavelength cutoff as 8 km and short wavelength cut off as 1 Km. The upward continuation was also defined at different depths varying from 1 km to 5 km. An upward continuation was considered and used as a clean filter because it provides almost no side effect that may require the application of the other filters or process to correct. Due to this, it was used to minimize the effects of shallow sources and noise (high spatial frequency) in the grid and highlighting regional features (Telford *et al.*, 1990; Ma *et al.*, 2013). Several anomaly Bouguer maps were generated. Through this process of filtering, the first objective was achieved in developing Bouguer anomaly maps.

3.5 The 3D Inversion Model

3.5.1 Gravity Anomaly Separation

Potential field anomaly maps (Bouguer anomaly map) normally presents the effects of both shallow and deeper geological structures. The two components are known as regional trends and local anomalies (residual) that can be expressed as (Pawloski, 1994):

$$G(x, y) = g_s(x, y) + g_d(x, y)$$

Where $G(x, y)$ is the observed gravity field, g_s and g_d refers to the gravity response of shallow and deeper structures respectively. Thus, one of the most important issues in the potential field data interpretation is the removal of the regional trends when dealing with shallow local geological structures (Khazri and Gabtni, 2018). Therefore, some mathematical methods are required to separate the map data into two components, which are the regional nature and the local fluctuations. To enhance this anomaly separation, the data was subjected to a 3 x 3-convolution filter in Geosoft Oasis Montaj software. A 3 x 3-convolution filter (or Hanning filter) removes the regional data trends from the data and produces a filtered curvature grid (Durham, 2017). This filter was subjected once to the gravity Bouguer grid to generate a filtered grid (output grid is the filtered grid).

3.5.2 Calculating the Residual Grid

Since the study presented herein deals with shallow geological structures from the earth's surface of the Paka volcano complex, regional/residual separation process was applied to gravity data set to eliminate the regional background amplitude. The final residual gravity grid was calculated by subtracting the filtered grid from the gravity Bouguer grid (Khazri and Gabtni, 2018)).

$$G_O = G_1 - G_2$$

Where G_O is the residual grid, G_1 is the original input gravity Bouguer grid and G_2 is the filtered grid.

3.5.3 Constraints on Crustal Structure

Most seismic and gravity studies determine the crustal thickness and densities constraints for the rift valley areas in Kenya using the rift axis seismic and gravity models from Henry *et al.* (1990), Mechie *et al.* (1994) and Simiyu and Keller (1997, 2000, 2001). Outside the rift, the KRISP 90, 94 cross-rift profiles (Muguire *et al.*, 1994), the rift flank profile (Prodehl *et al.*, 1994, 1997; Simiyu and Keller, 1997, 2001) that are used to calculate geometries and densities. Table 2 from Simiyu and Keller (1997), shows the structural units, observed velocity range and estimated density values used in modeling in Kenyan axial rift. The density of 2.67 g/cm³ was used as a constraint during the inversion process since the study area Paka prospect lies between Turkana – Baringo region for local depth in the upper crustal analysis as per table 2.

Table 2: Kenya rift axial seismic velocity versus density values used (Simiyu and Keller, 1997).

Unit	Region	V_p (km/s)	ρ (g/cm ³)
Sediments	Turkana area	2.00 – 3.10	2.350
Sediments	Lokichar-Baringo area	2.00-4.15	2.450
Sediments	Nakuru-Magadi area	2.00-3.85	2.450
Upper crust	Turkana-Baringo	6.10-6.30	2.700
Upper crust	Nakuru-Magadi	6.20-6.35	2.740
Upper crust	Tanzanian craton	6.00-6.20	2.680
Upper crust	Mozambiquan belt	6.10-6.30	2.700
Lower crust	Lokichar- Magadi	6.45	2.850

3.5.4 Preparing VOXI for Inversion and the Gravity Inversion Model

VOXI session was created by first defining the geographical area of interest (AOI) using a polygon file outlining the distinct region of an anomaly. A digital elevation model (DEM) for the area was also created and entered into the new VOXI session as a grid. A mesh showing the area of interest and depth of investigation was then created (Figure 3.6). The type of the potential field data was also entered, and in this case, residual gravity gird was used. A linear background was not removed since the removal of background can remove some residual data. The model resolution was either equal or less than (50, 50, 50) number of cell grids since if the number of cell grid is greater than this then inversion cannot run and if it's running, the model has greater errors. The inversion process runs online (using the internet) for some minutes, depending on the size of the AOI and the number of constraints being applied. When the inversion process was complete, the model then downloaded for modeling process.

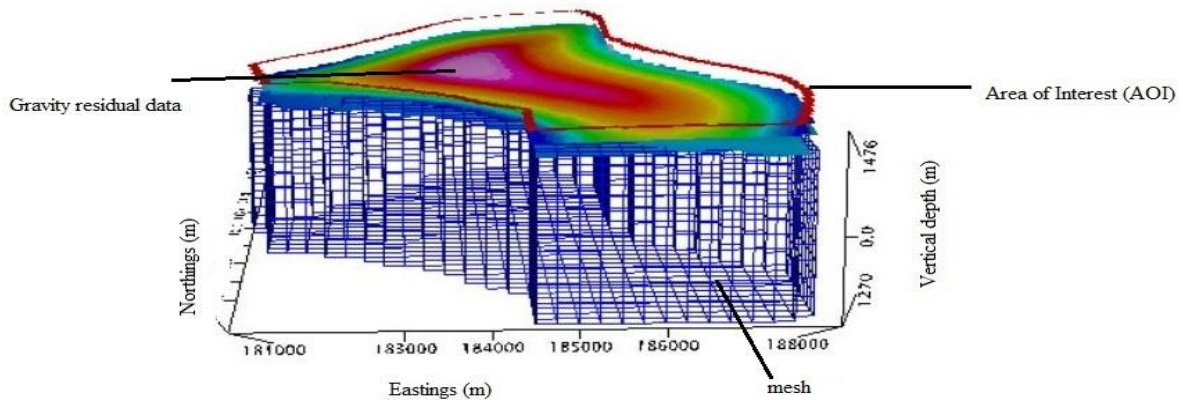


Figure 3.6: A mesh showing the Area of Interest (AOI), distinct areas (region) of an anomaly and the depth extent of modeling.

3.5.5 Gravity inversion Modeling

3D gravity modeling of an inverted model was carried out by clipping out the materials from the model. This procedure was carried out using the Geosoft VOXI manager via the clipping tool. For the inversion that was done on the high-density zones, the 3D modeling was achieved by systematic clipping out the low-density materials from the model. At each step, the low-density limit value of the density range was used to interpret the model and the depth to the top of the model was determined using the z component clip. However, the 3D gravity modeling for the low-density zones was achieved by systematic clipping out the high-density materials from the model. At each step, the high density of the density range was used to interpret the model, and the depth to the top of the model was determined using the z-direction component clipping. In 3D modeling, the subsurface physical properties (density contrast) vary with depth. For each step of clipping, the density contrast and the depth to the top of the model was noted for interpretation of the model. Through this, the second objective was achieved.

3.6 The 3D Density Model and Interpretation

After the inversion for whole area of Paka prospect, it was converted into 3D density model using an export tool in Geosoft Oasis Montaj version 8.5. Several vertical planes that served as profiles across the density model along the y-direction were employed to analyze the vertical density variation. For each of the anomaly, it was analyzed and interpreted based on the calculated density, shape, extended depth and the orientation of the anomaly.

3.7 Delineating the Subsurface Fault Structures

For delineating the subsurface volcanic fault structures, then derivative filters were applied to the gravity Bouguer grids. Several gravity interpretation techniques such as horizontal gradient HG, tilt derivative TDR, a horizontal derivative of the tilt derivative HG – TDR and analytic signal AS was applied to the gravity data with the objective of marking the faults or contacts more visible. The combination of these techniques was to improve the visual interpretation of subsurface fault structure (Nashijima and Naritomi, 2017; Khazri and Gabtni, 2018). The technique worked well with the gravity Bouguer anomaly grid. Each of the derivative filters and the analytic signal was applied once to the gravity Bouguer grid, and the interpretation for each technique as discussed in section 2.7 of this thesis.

CHAPTER FOUR

RESULTS AND DISCUSSION

4.1 Overview

The main focus of this study under Paka volcano in northern section of the Kenya rift system was to generate a geological interpretation of the density model derived from the gravity data inversion. But gravity inversion model normally sets an interpreter mind with a clear picture of the distribution of a geophysical parameters like depth, thickness, density and the orientation of anomaly that caused the recorded measurement in the field in the best way with reduced data misfit between observed data and the known geology. Also, basing on density distribution in the subsurface, to be able to explain whether the volcano is a potential for geothermal system.

4.2 Bouguer Anomaly Maps

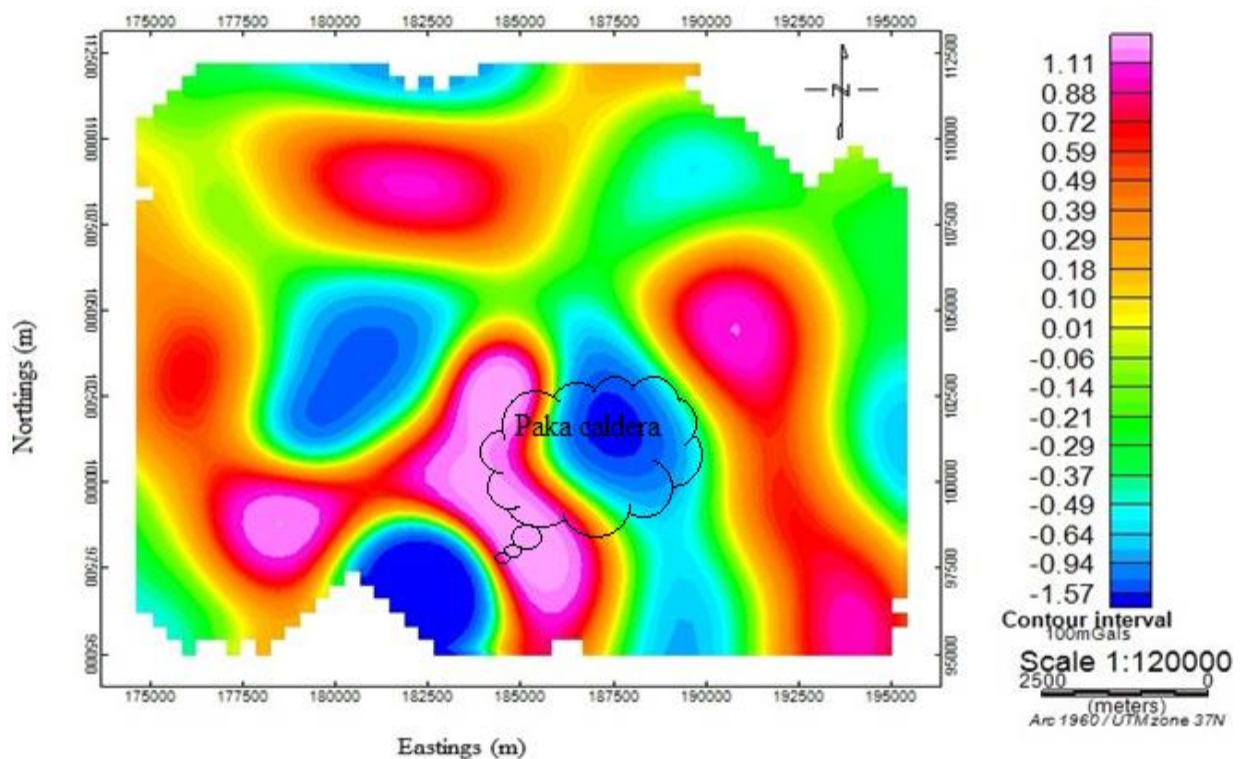


Figure 4.1: Bouguer anomaly map at upward continuation of 2 km

From the series of Bouguer anomaly maps that were constructed at upward continuation revealed that Paka volcano is associated with a broad gravity ‘highs’ and gravity ‘low.’ The high amplitudes highlighted at of 2 km upward continuation (Figure 4.1) is associated with near-surface features, but as the upward continuation increases to 5 km, the

amplitudes reduce since it highlights regional signatures at that depth (Figure 4.2). The positive anomaly is associated with high density intrusive while negative anomaly is due to low density fractured parts of rocks. The Bouguer anomalies in Figure 4.1 - 4.2 trends in NW–SE direction. But according to Mutonga (2013) and Wedge *et al.* (2016), Proterozoic basement trends in NW – SE in northern Kenya rift (from Menengai towards Lake Turkana). Hence, this basement seems to have played a role in guiding the magmatic activities associated with Bouguer anomalies orientation in Paka volcano.

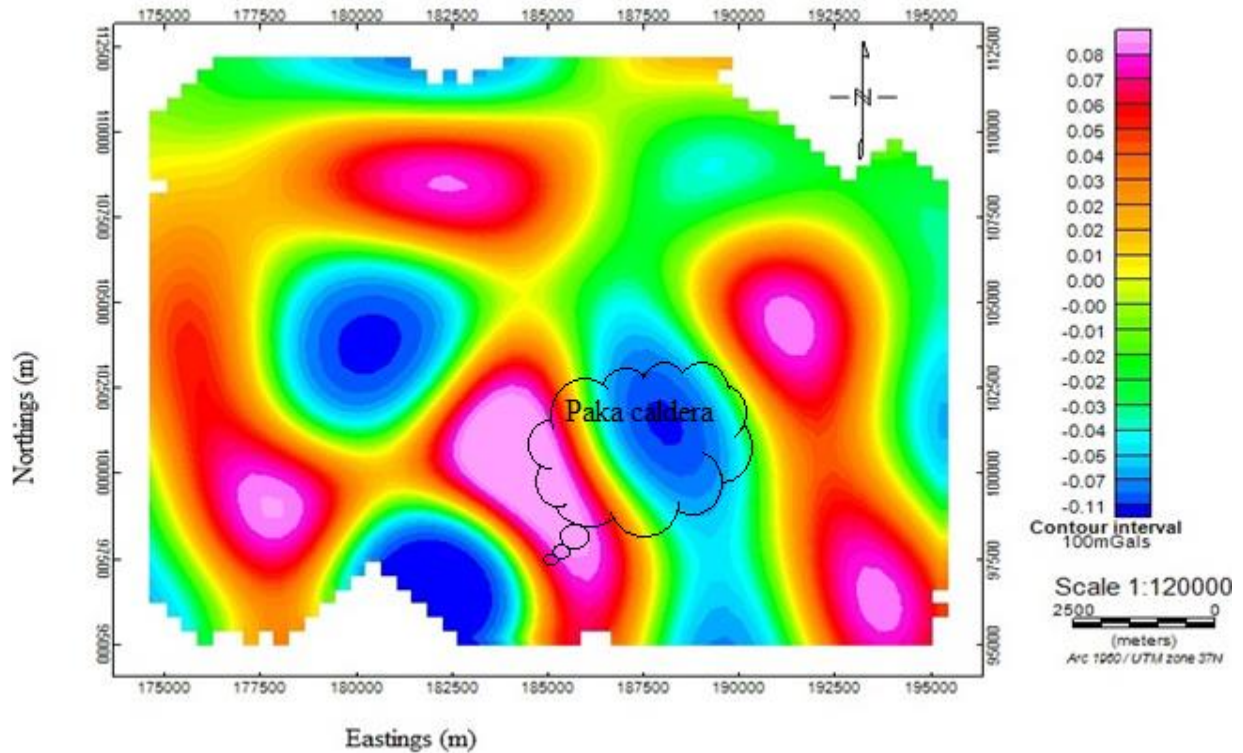


Figure 4.2: Bouguer anomaly map at upward continuation of 5 km

4.3 A Residual Gravity Map Showing the Area of Interest

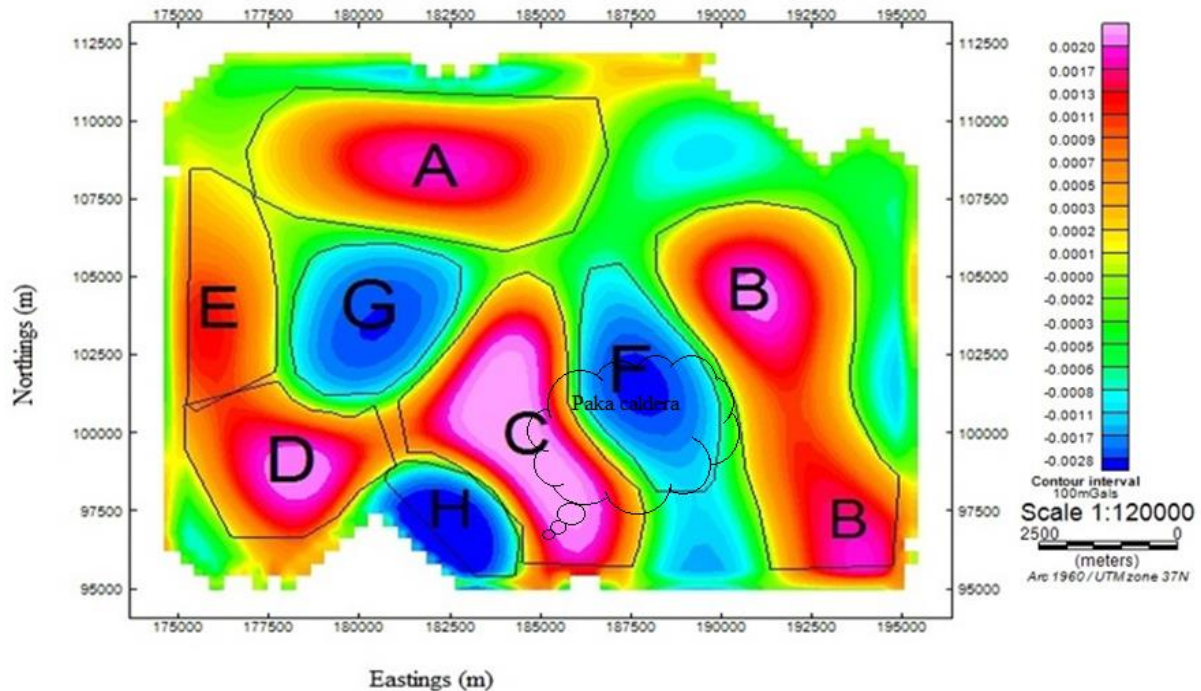


Figure 4.3: A residual gravity map showing the anomaly regions to be modeled

4.3.1 3D Gravity Inversion Model for Region A (*Riongo area*)

Modeling to a density range $2.77 \text{ g/cm}^3 - 2.941 \text{ g/cm}^3$ and the depth from the earth's ground surface to the top of the model was 393 m (Figure 4.4).

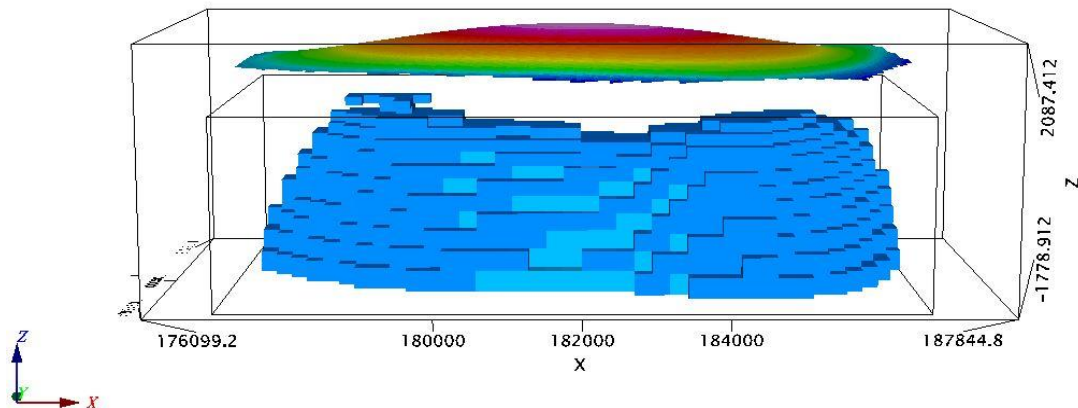


Figure 4.4: Region A clipped to density range $2.77 \text{ g/cm}^3 - 2.941 \text{ g/cm}^3$

Further modeling to the density range $2.88 \text{ g/cm}^3 - 2.941 \text{ g/cm}^3$ the depth from the ground surface to the top of the 3D model increased to 1170 m (Figure 4.5).

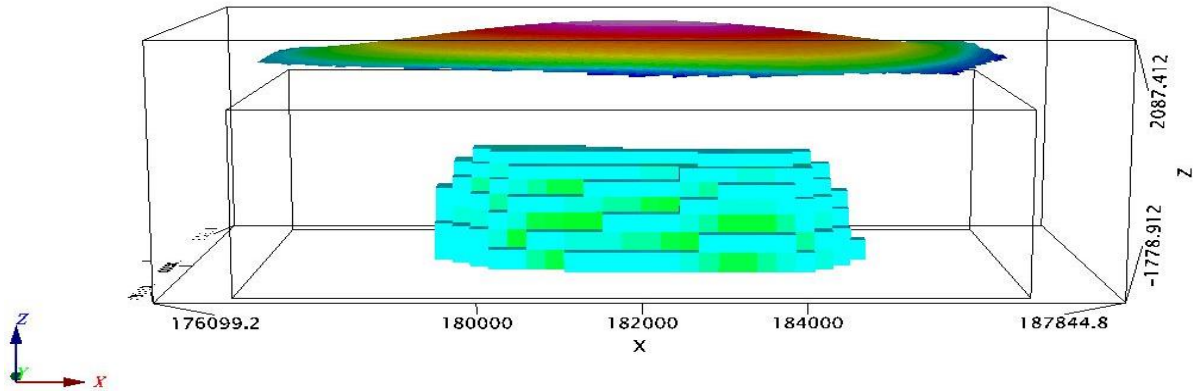


Figure 4.5: Region A modeled to density $2.88 \text{ g/cm}^3 - 2.941 \text{ g/cm}^3$

The region A is overlain by low density 2.47 g/cm^3 surficial layer at a depth less than 300 m that were interpreted as due to volcanoclastic/pyroclastic sediments. The calculated surficial layer low density of 2.47 g/cm^3 agrees with the Mulwa and Mariita (2013) modeled low surficial density of 2.4 g/cm^3 due to volcanic soils sediments at Arus-Bogoria in the south of Paka prospect. According to Kearey *et al.* (2013) and Nyakundi (2017), an intruding rock has a density ranging from $(2.70 - 3.20) \text{ g/cm}^3$. As the depth to the top of the model increases from 293 m to 1170 m, the calculated rock density also increases from 2.77 g/cm^3 to 2.88 g/cm^3 . The calculated density range was interpreted as an intruding rock. From Figure 4.4, the top of the model appears to be horizontally flat which imply an intruding rock is a sill. At a depth of 2625m from the earth's surface to the top of the modeled body, the model has a density of 2.941 g/cm^3 . This calculated density of 2.941 g/cm^3 , it is in line with an axial rift profile gravity high model mafic body density 2.9 g/cm^3 (Simiyu and Keller, 2001).

4.3.2 3D Gravity Inversion Model for Region B (*Cheptebesia*)

The model had a maximum extent of 2857 m from the earth's surface and initial density range of $2.661 \text{ g/cm}^3 - 2.953 \text{ g/cm}^3$. On removal of low-density material from the inversion model to the density range of $(2.675 - 2.953) \text{ g/cm}^3$, the vertical depth to the top of the model was 391 m (Figure 4.6).

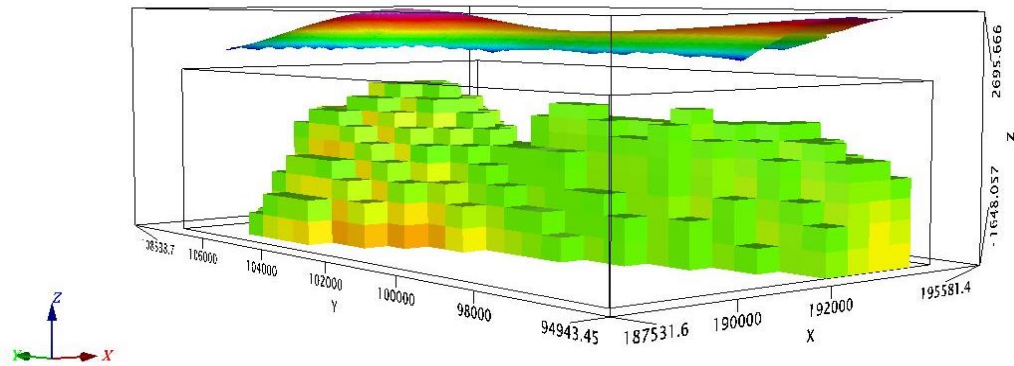


Figure 4.6: A 3D modeled body for region B at to density range (2.675 – 2.953) g/cm³

At a depth of 1011 m to the top of the inverted model, the density range was (2.785 – 2.953) g/cm³. The lower limit of calculated the density of 2.675 g/cm³ and 2.785 g/cm³ at a depth of 391 m and 1011 m respectively fall under the density (2.70 – 3.20) g/cm³ of intruding rock of (Kearey *et al.*, 2013; Nyakundi, 2017). From the calculated density, the intruding body was interpreted as a dyke due to its sharpness at the top. This modeled dyke body was compared with high-density dyke intrusions at Gilgil prospect in Nakuru County by Nyakundi (2017) that had the density range of (2.77 – 2.95) g/cm³ at shallow depth, where the study indicated that the intrusions could be taken as the heat sources for the prospect. This magmatic dyke intrusion trend/orient in NW – SE direction. But according to Mutonga (2013) and Wedge *et al.* (2016), the Mozambique Proterozoic mobile basement belt trends in NW – SE in northern Kenya rift (from Menengai towards Lake Turkana). Hence, from this study, the Proterozoic basement seems to have played a role in guiding this magmatic dyke intrusion orientation at region B.

4.3.3 The 3D Inversion Model for Region C (*Paka summit*)

On modeling the model to the density range of (2.787 – 3.176) g/cm³, the depth to the top modeled body was 367 m (Figure 4.7).

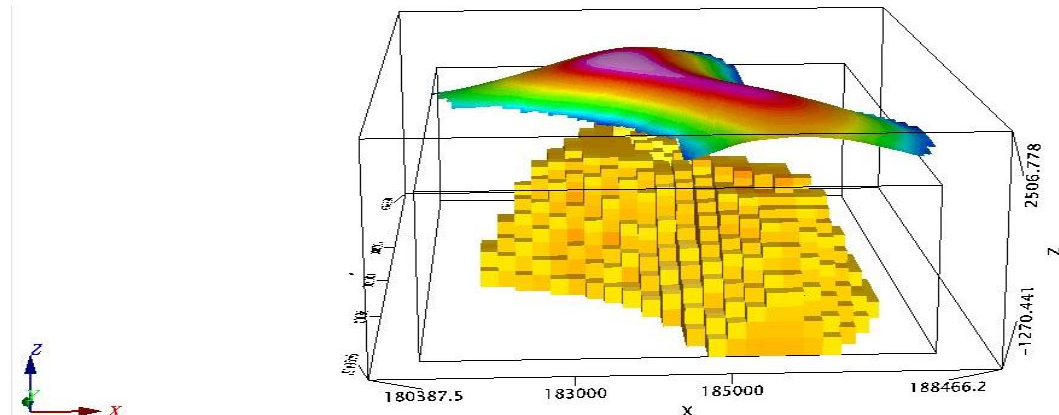


Figure 4.7: An intrusive body for region C at density range (2.787 – 3.176) g/cm³

As the depth to the top of the modeled intrusive rocks increased to 897 m from the earth's surface, the density range changed to $(2.983 - 3.176) \text{ g/cm}^3$. Based on Kearey *et al.* (2013) and Nyakundi (2017) arguments that high-density intrusion rocks are of density range $(2.70 - 3.20) \text{ g/cm}^3$. Then it implies that the calculated density range at depths of 367 m and 897 m respectively fall under the high-density intrusion rocks. But region C also falls under the Paka caldera that encompasses intensified fracture and fault patterns which can be discerned by many ridges on the summit area, that providing evidence of shallow magma chamber. From Mutonga (2013) argument of intensified faults and fracture and the indication of magmatic activities by Robertson *et al.* (2016) about the young eruption of Basaltic lava that occurred at 10 Ka within Paka caldera, it is beyond proven that the calculated high-density range at this shallow depth can be interpreted as a shallow magma intrusion. Also, this magmatic intrusion under region C trends in NW – SE. According to Robertson *et al.* (2016), Paka elliptical caldera is oriented in NW – SE, that is aligned with Proterozoic pre-existing basement structures and perpendicular to the rift faults. These pre-existing structures seem to have controlled the storage and orientation of this shallow magma reservoir.

4.3.4 Inversion Model for Region D (*Paka west*)

The initial model had density range $(2.491 - 3.025) \text{ g/cm}^3$, and it extends to a maximum depth 1725 m from the earth's surface. On modeling to a density range $(2.71 - 3.025) \text{ g/cm}^3$, the depth to the top of the model was 120 m from the earth's surface (Figure 4.8). As the modeling continues to density range $(2.85 - 3.025) \text{ g/cm}^3$, the depth increased to 480 m from the earth's surface to the top of the model. As the depth increases, the intrusion becomes more cylindrical in nature.

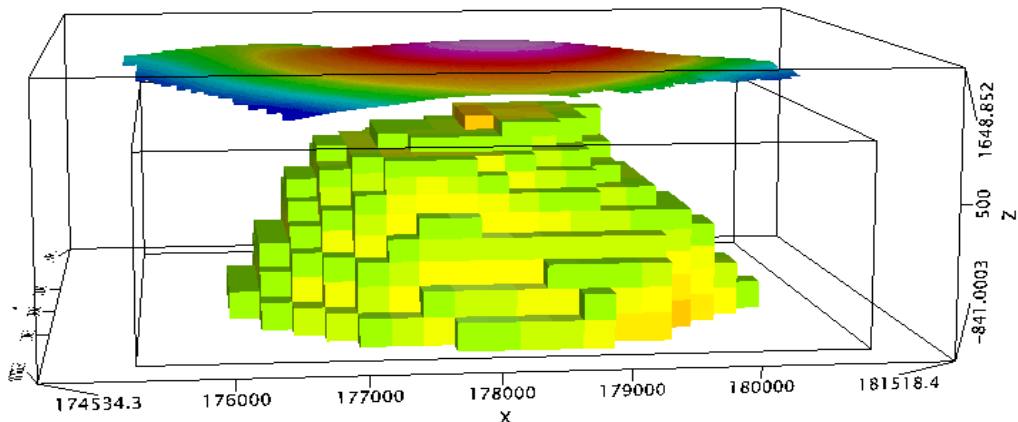


Figure 4.8: Modeled body for region D at density range $(2.71 - 3.025) \text{ g/cm}^3$

Due to high-density range for the modeled body in region D, the intrusion was interpreted as a dyke. The modeled mafic density under region D is in agreement with other studies done in Arus-Bogoria and the axial northern rift where the mafic density was 2.9 g/cm^3 (Mariita and Keller, 2007; Mulwa and Mariita, 2013; Ochieng, 2014; Renaut *et al.*, 2017). The dyke intrusion trends in NW–SE direction. The orientation of this dyke is in line with the Proterozoic basement that trends in NW–SE as per Wedge *et al.* (2016). Hence, the study can indicate that the pre-existing Proterozoic structure seems to have played a role in guiding the intrusion orientation.

4.3.5 The Inversion Model for Region E (*Tuwot*)

An initial model had a density range $(2.57 – 2.791) \text{ g/cm}^3$ and extended to a maximum depth of 2159 m from the earth's surface. At density range of $(2.675 – 2.791) \text{ g/cm}^3$ on the removal of low density from the initial model, the depth from the earth's surface to the top of the model was 553 m (Figure 4.9). As the depth increased to 1123 m from the earth's surface, the density changed to $(2.695 – 2.791) \text{ g/cm}^3$.

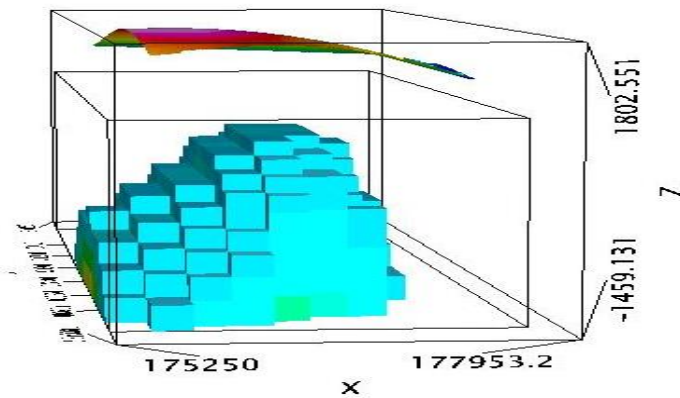


Figure 4.9: An inversion model for region E $(2.675 – 2.791) \text{ g/cm}^3$

The surficial layer of Paka prospect is characterized by low density due to volcanoclastic sediments or clay sediments (Lichoro *et al.*, 2017). Hence, this modeled low density 2.60 g/cm^3 at a depth less than 450 m from the earth's surface that overlain region E was interpreted as due to volcanoclastic sediments or clay sediments and or volcanoclastic sediments. This calculated density range of $(2.675 – 2.791) \text{ g/cm}^3$ and $(2.695 – 2.791) \text{ g/cm}^3$ was viewed as density for intrusive rocks as per Kearey *et al.* (2013) and Nyakundi (2017), who postulated that an intruding rock has a density ranging from $(2.70 – 3.20) \text{ g/cm}^3$. The intrusion was interpreted as a magmatic dyke intrusion and it trends in NW – SE direction. Similarly, the Proterozoic basement interpreted by Wedge *et al.* (2016) that trends in NW – SE

seem to control the orientation of this intrusion. The intrusion under region E was compared to an intrusion under region B and it is observed that the intrusion at region E has lower density range than that under region B.

4.3.6 An Inversion Model for Region F (*Eastern flank of Pako summit*)

On modeling to a depth of 408 m from the earth's surface, the density range was (2.528 – 2.682) g/cm³ (Figure 4.10). Further removal of high density from the model to the density range of (2.528 – 2.616) g/cm³, the depth to the top model increased to 938 m from the earth's surface.

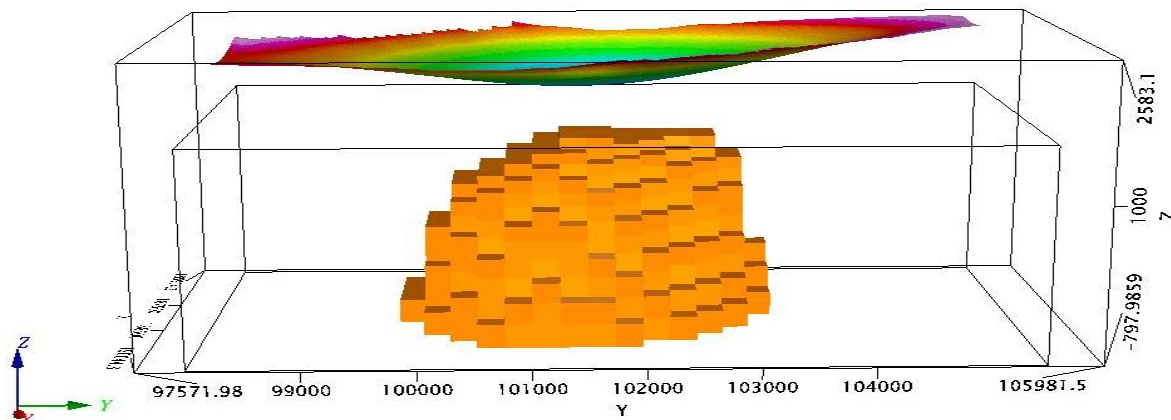


Figure 4.10: An inversion model for region F at density range (2.528 – 2.682) g/cm³

Under region F, the surficial layer is characterized by high density above 2.620 g/cm³ at a depth of 600 m; it was tentatively interpreted as volcanoclastic/pyroclastic sediments that forms a cap that overlain a lower density zone. As depth increases from 600 m to 2351 m from the earth's surface, the density reduces approaching 2.528 g/cm³. This low-density intra-fault swarm was interpreted as the hydrothermally altered clay or partial melting rock zone or due to higher porosity or highly fractured parts of rocks. Due to higher porosity or highly fractured parts of rocks, the zone provides a good structural set up that allows recharge of the prospect and penetration of water into deep crust towards the high density/hot magmatic modeled bodies. According to Swain (1992), Mariita and Keller (2007) and Sippel *et al.* (2017) the density of the host rock is taken as 2.70 g/cm³ and a density range of (1.60 – 2.70) g/cm³ has been augmented as density for gravity 'low'. The low-density intra-fault swarms' trends in NW – SE. But according to Robertson *et al.* (2016), the pre-existing Proterozoic basement trends in NW – SE and the presence of extensional local stress regime in northern Kenya rift, seem to control this intra-rift swarm fault orientations under region F.

4.3.7 An Inversion Model for Region G (*South Riongo area*)

An initial model had a density range (2.00 – 2.632) g/cm³, and the model extends to a maximum depth of 2085 m from the earth's surface. The high-density material was clipped out of the model since the inversion was for low gravity region. At density range (2.00 – 2.548) g/cm³, the depth to the top of the model was 534 m from the ground surface. On further removal of high-density material from the model to depth 1174 m, density changed to (2.00 – 2.417) g/cm³ (Figure 4.11).

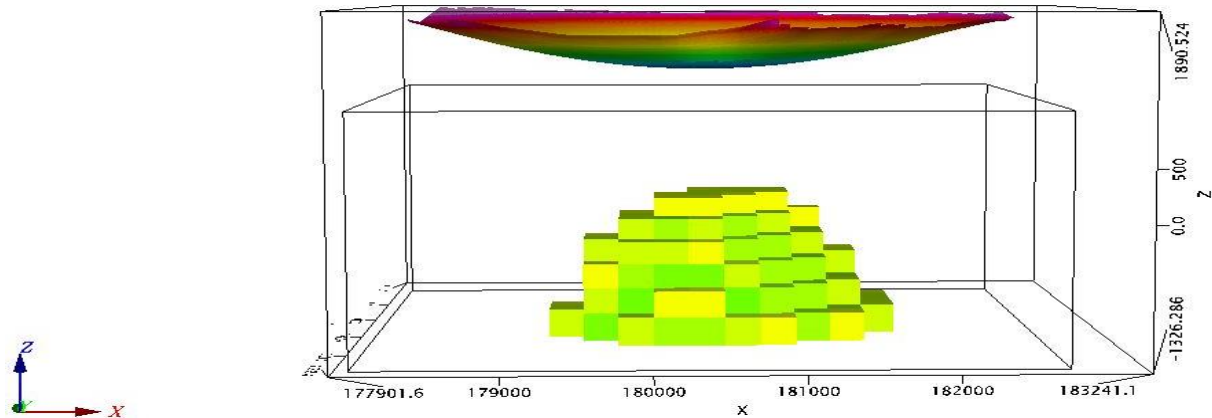


Figure 4.11: Inversion model at density range (2.00 – 2.417) g/cm³

The surficial high-density layer more than 2.60 g/cm³ that overlain the low-density zone was due to volcanoclastic/pyroclastic sediments. This surficial high-density layer seems to provide the cap to the low-density zone. Reduction in rock density as depth increases might be due to partial melting of rocks or due to high porosity or fracturing of rocks. Tentatively at the depth greater than 1174 m, the zone was interpreted as altered clay zone based on Kearey *et al.* (2013), the density of clay is (1.63 – 2.60) g/cm³. The zone is surrounded by high density hot mafic intrusions, which implies that it's good for hot thermal fluids reservoir.

4.3.8 Gravity Inversion Model for Region H (*southern flank of Paka summit area*)

An initial model had density range (2.281 – 2.672) g/cm³, and it extends to a maximum depth of 1454 m from the earth's surface. On modeling to a density range (2.281 – 2.658) g/cm³, the depth to the top of the model was 720 m (Figure 4.12). Further modeling by clipping out the high-density material from the model a depth 905 m, the density change to (2.281 – 2.505) g/cm³. According to the Kearey *et al.* (2013) and Nyakundi (2017), the calculated density ranges for this region fall under the gravity 'low' of density range (1.60 – 2.70) g/cm³. The high-density surficial layer greater than 2.10 g/cm³ was due to volcanoclastic sediments

that form a cap to the lower density zone. As depth increases, the density approaches 2.281 g/cm³ for region H that was interpreted as a zone of high porosity or highly fracturing. As per Lichoro *et al.* (2017), the zone of high porosity or highly fracturing was viewed as hydrothermally altered clay zone.

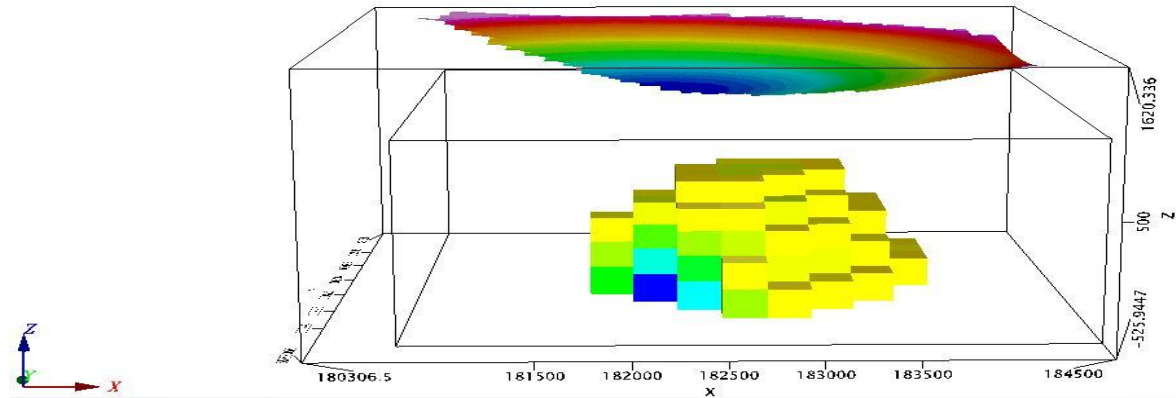


Figure 4.12: An inversion model for region H at density range (2.281 – 2.658) g/cm³

4.4 The 3D Density Model of Paka Prospect

Model for Paka volcano covered an area approximately 258.49 km². The 3D density model revealed a density distribution patterns that are consistent with the existence of the several 3D massive intrusion bodies for each anomaly within the Paka prospect (Figure 4.13). The subsurface local depth geology was explained regarding 3D density model and interpretations based on table 2 and 3.

Table 3: P-wave velocity model, layer thickness and lithology (Simiyu and Keller, 2000, 2001)

Layer number	Thickness (Km)	P-wave velocity	Lithology
1	0.2	2.0	Pyroclastic
2	0.8	3.7	Trachyte/Basalts
3	1.5	4.2	Lava/intrusive
4	4.0	5.0	Fractured granite
5	> 6.5	6.0	Crystalline basement

Paka prospect is overlain with the surficial layer of density range (2.10 – 2.40) g/cm³ volcanic soils and sediments at thickness 200 – 300 m (table 2). From the elevation grid of Paka prospect figure 3.5 central volcano in SE that rises to a maximum height of 1697 m and the lowest elevation region in NW that rises to 830 m above the sea level has same surficial

layer density range ($2.10 - 2.40$ g/cm 3). The surficial layer density it is in line with Arus-Bogoria modeled 2.40 g/cm 3 surficial density (Mulwa and Mariita, 2013).

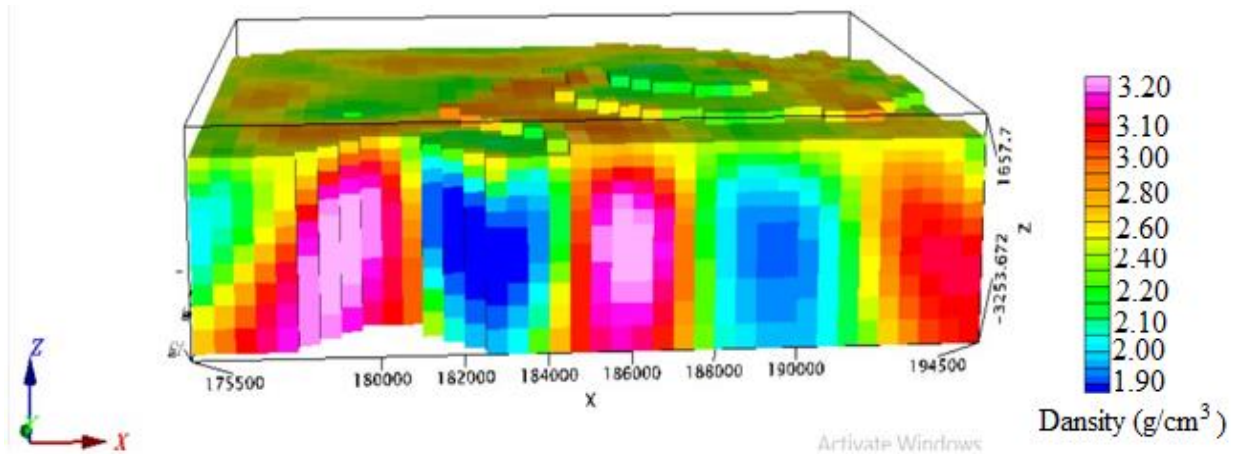


Figure 4. 13: The 3D density model of Paka prospect

Vertical planes across the density model along y-direction were employed to analyze vertical density variations. A profile 99000 northings Figure 4.14 indicates vertical density variations for different modeled regions. West of region D has a slanting low-density material less than 2.50 g/cm 3 that was interpreted as volcanic sediments or due to highly fractured parts of rocks. Region D and C is overlain with (2.20 – 2.50) g/cm 3 low-density volcanic soils and sediments. At a depth, more than 400 m from the earth's surface, the density for regions C and D increases from 2.60 g/cm 3 to 3.20 g/cm 3 that was interpreted as dyke intrusion or shallow magma (Table 2). For region F, its density is less than 2.60 g/cm 3 at depth more than 4608 m maximum extents. Due to (1.90 – 2.60) g/cm 3 low density in a filled zone, then the zone was interpreted as a result of clay or volcanic soils or highly fractured rocks (Table 2). Region B has a density (2.40 – 3.10) g/cm 3 that was interpreted as a high-density intrusion dyke bordering (2.10 – 2.40) g/cm 3 fractured rocks on either side.

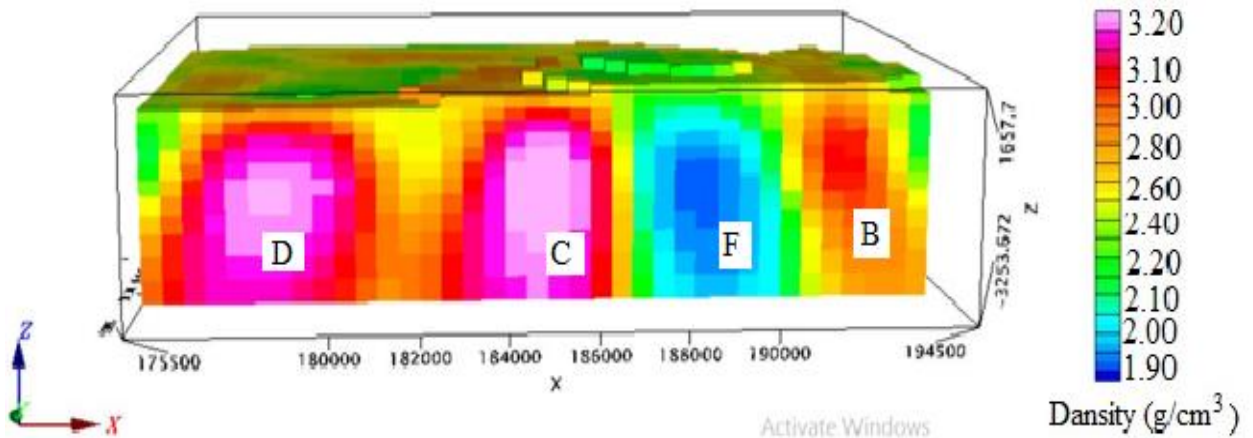


Figure 4.14: Profile 99000 in the y-direction across the 3D density model

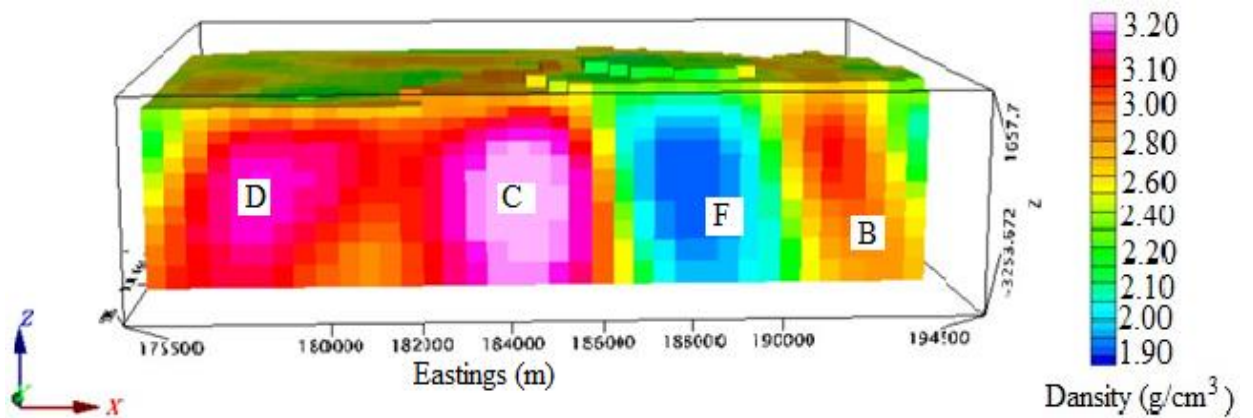


Figure 4.15: Profile 99800 in the y-direction across the 3D density model

From Figure 4.14 and Figure 4.15, region D reduces in intrusion density while the intrusion density for under region C increases. Between regions D and C, the rock density is more than 2.80 g/cm^3 that was seen as an intrusion rock. For region F, the rock density is lower than 1.90 g/cm^3 which implies rock fracturing increase northwards that in turn increases rock porosity. As the profile increases northwards to profile 102700 northings, the eastwards of region B ($2.10 - 2.60 \text{ g/cm}^3$) low density increases inwards compared to previous profiles. From Figure 4.16 it means that the right triangular region B intrusion trends in NW – SE direction. The rock density ($1.60 - 1.90 \text{ g/cm}^3$) for region G and F under Figure 4.16 has reduced, but rock fracturing is well developed at its center. The rock fracturing that is well developed for region G downwards has greatly affected the roots for the high-density intrusion of E and C (Figure 4.16). The low density for region G that is as a result of intensely fracturing/faulting can form a good reservoir rock for geothermal fluids.

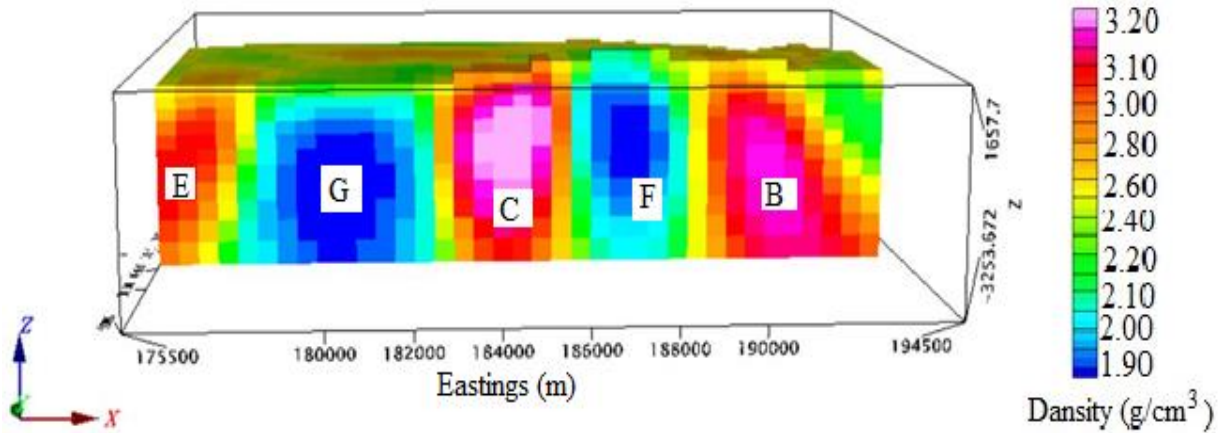


Figure 4.16: Profile 102700 in the y-direction across the 3D density model

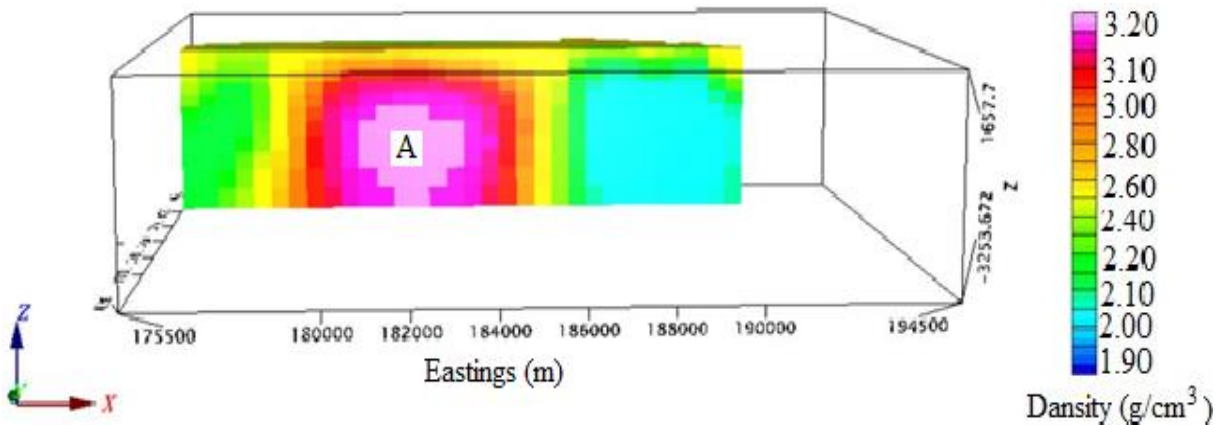


Figure 4.17: Profile 108500 in the y-direction across the 3D density model

Profile 108500 cuts across region A as in Figure 4.17. The region is surrounded by $(2.00 - 2.60) \text{ g}/\text{cm}^3$ low-density rocks. Due to its $(2.60 - 3.10) \text{ g}/\text{cm}^3$ high density, it was interpreted as sill intrusion as the top of this region appear to be horizontally flat.

Generally, the calculated surficial layer low density ($2.10 - 2.40) \text{ g}/\text{cm}^3$ agrees with the Mulwa and Mariita (2013) modeled low surficial density of $2.4 \text{ g}/\text{cm}^3$ due to volcanic soils sediments at Arus-Bogoria in the south of Paka prospect. According to Kearey *et al.* (2013) and Nyakundi (2017), an intruding rock has a density ranging from $(2.70 - 3.20) \text{ g}/\text{cm}^3$. From our interpretation of high-density intrusions, then it agrees with Kearey *et al.* (2013), and Nyakundi (2017) augments and for the low-density zones. Comparing the $(2.60 - 3.20) \text{ g}/\text{cm}^3$ calculated modeled high-density intrusion and the axial rift profile gravity high model mafic body of density $2.9 \text{ g}/\text{cm}^3$ by Simiyu and Keller (2001), then it agrees with it. All modeled high-density intrusion and the low-density zones trends in NW – SE. But according to Mutonga (2013) and Wedge *et al.* (2016), the Proterozoic basement trends in NW – SE in northern Kenya

rift (from Menengai towards Lake Turkana). Hence, from this study, the Proterozoic basement seems to have played a role in guiding the magmatic dyke intrusions and low-density zones orientation in Paka volcano.

4.5 Delineating the Subsurface Fault Structures in Paka Prospect

Several gravity interpretation techniques such as horizontal gradient HG, tilt derivative TDR, a horizontal derivative of the tilt derivative HG – TDR and analytic signal AS was applied to the gravity data with the objective of making the geological features such as faults or contacts more visible. The combination of these techniques was to improve the visual interpretation of subsurface structure. The technique worked well with gravity Bouguer anomaly grid.

4.5.1 Horizontal Gradient contour map

The technique is extensively used to locate the boundaries of density contrast from gravity data. With the aid of Oasis Montaj software, HG filter was subjected to the gravity Bouguer grid to generate horizontal gradient map (Figure 4.18). According to Rosid and Siregar (2017), the horizontal derivative can identify or show the existence of near-surface fault that is indicated by a zone of highest anomalous gravity value because on the fault zone there is highest contrast rock density. Therefore, from Figure 4.18, the region labeled 1, 3 and 5 are near surface fault zones due to the highest anomalous gravity value. Also, deeper the depth of the fault can be observed, but the gravity anomalous amplitude value is getting smaller (Mwaura, 2016; Rosid and Siregar, 2017). In that case, regions labeled 2, 4 and 6 was interpreted as deeper fault zones. In another way, the anomalous gravity values on horizontal derivative contour map can be explained regarding variations of dip faults, where the greater dip of the fault the bigger amplitude value of horizontal derivative as the gravity horizontally contrast increases. Hence, regions 1, 3 and 5 are viewed as fault zones with greater dip while the regions 2, 4 and 6 are fault zones with less dip. The interpreted faults zones both deep and near-surface faults trends in Northwest to southeast direction are parallel to major rift fault and pre-existing Proterozoic basement regional tectonic structures (Mulwa *et al.*, 2014; Wedge *et al.*, 2016). Hence, these pre-existing structures seem to have played a role in guiding the orientation of the interpreted faults. But Paka volcano is situated in northern Kenya rift where extensional stretching force (extension local stress regime for shallow magmatism) that was subjected to crustal layer during the rifting process, the weak zone developed half graben or swarms of intra-faults as a result of rock fracturing (Njue, 2015; Robertson *et al.*, 2016).

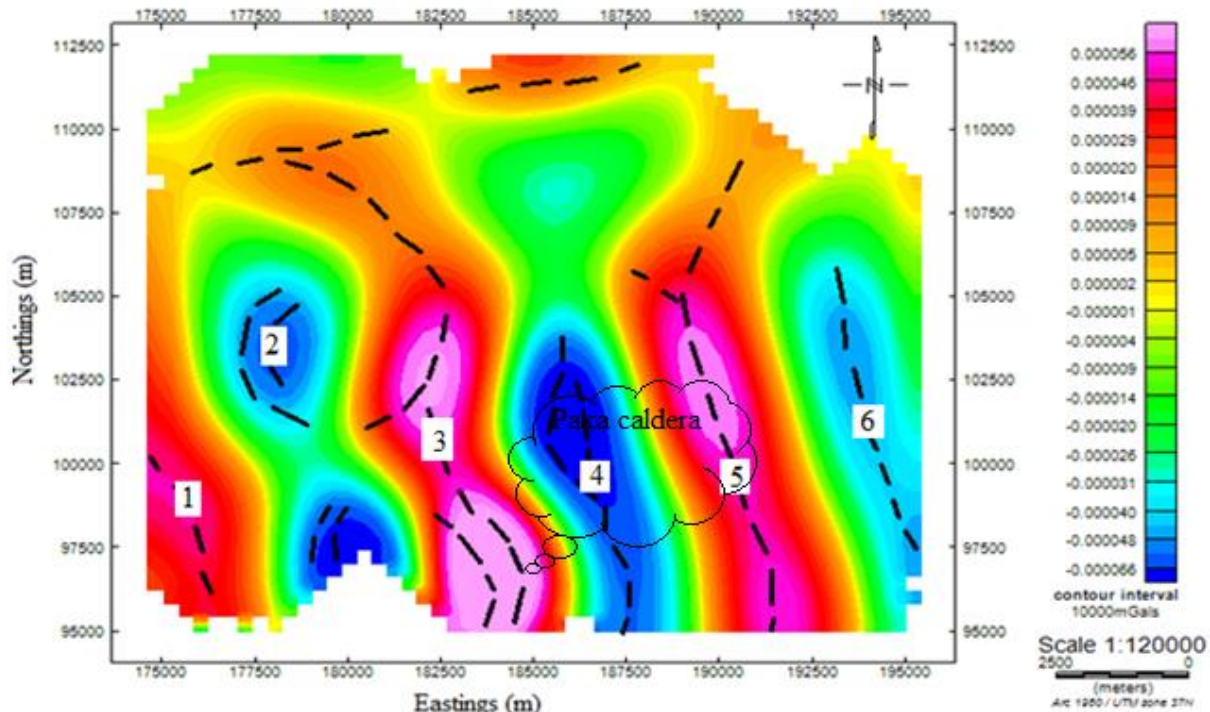


Figure 4.18: The horizontal gradient contour map that shows a shallow and deeper geophysical fault structure

4.5.2 Tilt Derivative Contour Map (Tilt Depth Map)

The technique was used to enhance and sharpen the potential field anomalies. In Oasis Montaj software, the tilt derivative contour map was mapped through the application of tilt derivative filter on the gravity Bouguer grid (Figure 4.19). The zero contours in Figure 4.19 delineate the edges between two geophysical structures. This geophysical edge structure was interpreted as fault contact. Also, the depth to the top of fault was estimated directly from the tilt depth contour map Figure 4.19 by simply measuring the distance between appropriate contours of the gravity data that is restricted to the range - 45 °, 0° and +45°. In Oasis Montaj software has a display method that uses a colour contour fill which allows rapid visual inspection of depth variations over a geophysical study area (Fairhead *et al.*, 2010). From Figure 4.19, the zero contours occur at depth range (2.5 – 3.0) km that it is the depth to the top of fault contact. The fault boundary is in between the high anomalous gravity amplitude associated with shallow massive intrusive (depth less than 1.5 km) and the deeper structures associated with smaller anomalous gravity amplitude at depth 4.5 – 5.0 km. The interpreted faults trends in N-S, E-W, NW-SE and NE-SW at a different depth from the earth's surface. The subsurface fault trending agrees with Dunkley *et al.* (1993) the topographic fault trending.

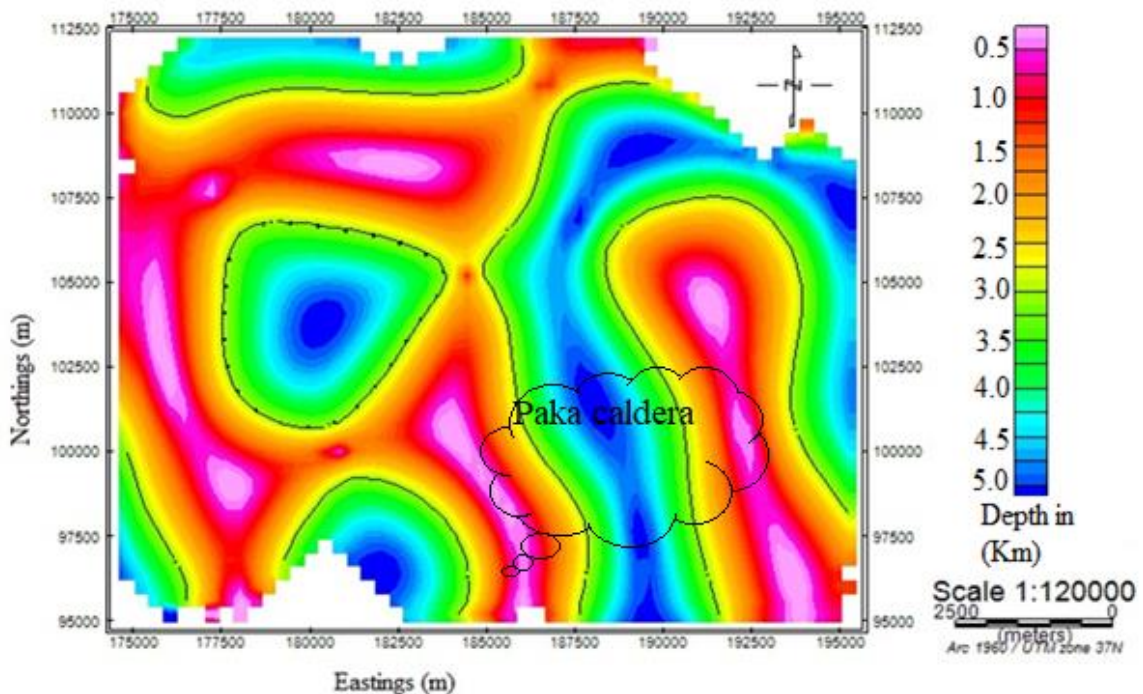


Figure 4.19: The zero contours on the tilt depth map shows a geophysical fault structure

4.5.3 Horizontal Derivative of the Tilt Derivative Contour Map

The technique can identify vertical contact between the subsurface rocks and generates the maximum gravity amplitude values directly over the fault zone due to the presence of high contrast rock density (Verduzco *et al.*, 2004; Anudu *et al.*, 2014). The high amplitudes gravity values identified by dotted lines in Figure 4.20 delineates the appearance of faults. The higher the anomalous gravity amplitude values in Figure 4.20 mean that the faults occur at the shallower depth. The deeper structural faults can be identified in Figure 4.20, but with reduced amplitude values since at a greater distance (depth) of an anomaly body, the gravity anomaly is smaller. The deeper sources of a fault were identified on the western part of the volcano and discrete spikes encompassed by shallow faults in the Paka volcano region. Comparing Figure 4.18 interpreted faults at shallow depth with Figure 4.20 the zero contour fault, the delineated faults appear to coincide with each other. The interpreted faults trends in N-S, E-W, NW-SE and NE-SW at a different depth from the earth's surface.

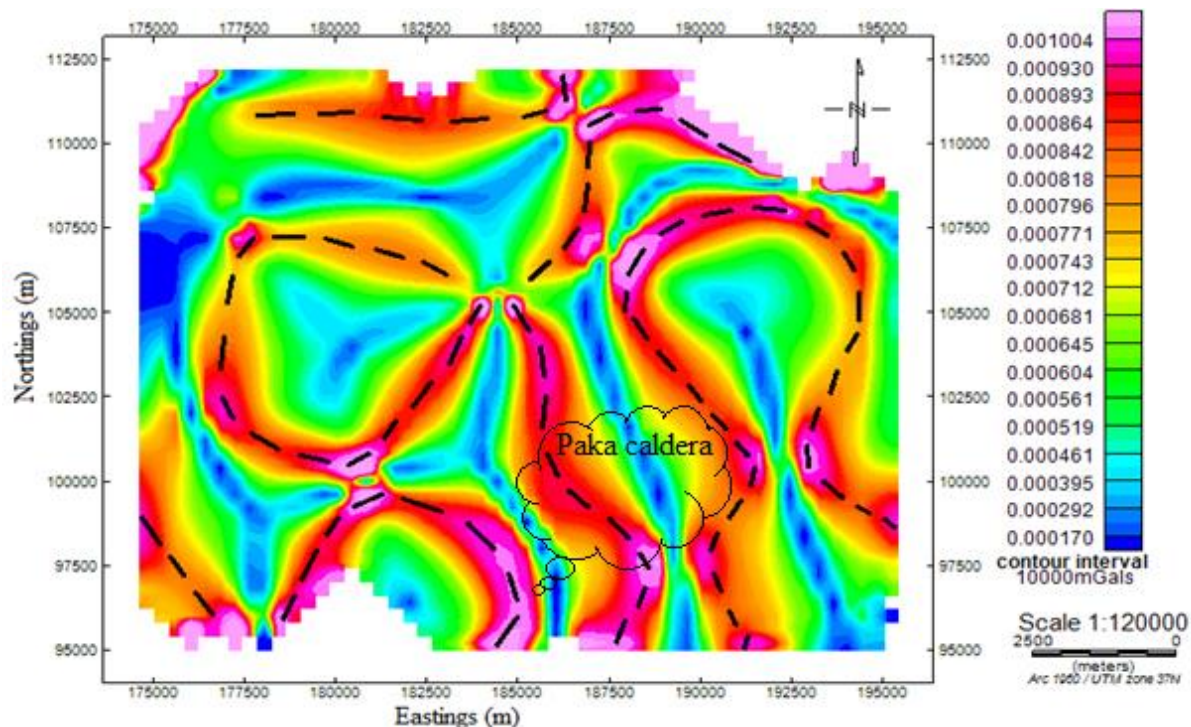


Figure 4.20: Horizontal derivative of the tilt contour map shows a geophysical shallow fault structure indicated by the black dotted line in gravity high amplitude zone

4.5.4 An Analytic Signal Contour Map

The analytic signal filter can locate and identify zones of high rock density contrast at a different depth by producing maxima over the high-density rock contrast regardless of the fault strike (MacLeod *et al.*, 1993). The maxima amplitude values identified in the analytic signal map in Figure 4.21 delineates a fault zone. The amplitude gravity values increase with the reduction of depth to the top of a fault structure. From this augment, the fault zone in the region H occur at shallow depth while the structural sources at NW and NE of Paka prospect occur at deeper depth. The high maxima zones on the Analytic signal contour map was interpreted as zones with a high degree of fracturing. The low-density zones F, G and H from figure 4.3 that was overlaid on top of the analytic signal map, the regions exactly coincided with the maximum amplitude values of the analytic signal map (Figure 4.21). This coincided with low-density zones on Bouguer anomaly map with maxima regions on analytic contour map implies that the low-density zones are associated with high degree of fracturing. The fault zone that runs from the north through G and H can be interpreted as an axial fault zone while the fault zone from H through F to the northwest was interpreted as a lateral fault.

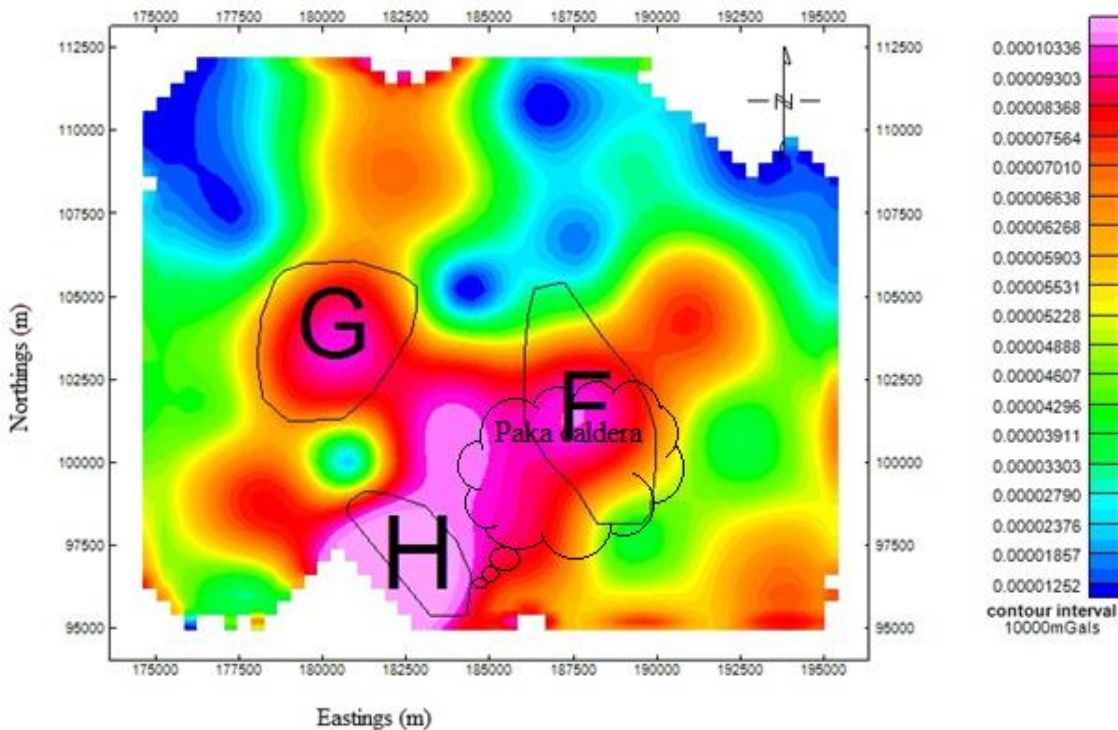


Figure 4.21. The Analytic signal map

4.6 Discussion of the Results

The main aim of this study was to give a geological interpretation of the density model derived from a gravity data processing and investigate the local structural features associated with the geothermal system. The results obtained in this geophysical study was able to substantiate gravity as an effective tool for modeling and mapping. A more detailed evaluation of the gravity method was carried out to determine the physical parameters necessary for the interpretation of the subsurface local structural features. The method involved data corrections, filtering, gravity inversions, modeling and data interpretation. The physical parameters that were being sought include depths, density and 3D shapes and sizes of the bodies causing the gravity anomalies. The results obtained in this geophysical investigation were subjective and entirely relied on geologic interpretation.

Past studies focused on tectonic evolution of the East Africa rift, lithospheric and crustal analysis at regional analysis (Simiyu and Keller, 1997, 2001; Mariita and Keller, 2007; Wamalwa *et al.*, 2013; Abdelfettah *et al.*, 2016; Lichoro *et al.*, 2017; Sippel *et al.*, 2017). This study is an extension of the regional studies in northern Kenya rift into a detail local analysis in Paka volcano. The study focused on subsurface density distribution to explain the local structural features in relation to Paka geothermal system.

According to Kearey *et al.* (2013), Mulwa and Mariita (2013), Shako and Wamalwa (2014) for shallow crustal analysis, a band pass filter and upward continuation filter is applied to simple Bouguer data. A bandpass of 8 km long wavelength and 1 km short wavelength was subjected first to simple Bouguer data then followed by an upward continuation varying from 1 km to 5 km. For local analysis less than 5 km were based on the regional studies previously done in the northern Kenya rift. For example the study done by Omenda (2014b) and Omenda and Simiyu (2015) where Magnetotelluric technique showed an existence of a conductor directly under volcano and seismic studies indicated a shallow events directly under Paka suggesting a hot body exist below 5 km depth. Along the Kenya rift, there exist bristle ductile transition limit at a depth of 6 km and above. Hence, for geothermal system analysis should be analyzed at depth less than 6 km (Simiyu *et al.*, 1998). Also, regional Seismic analysis studies done along the axial rift indicated local events at a depth less than 6 km (Simiyu and Keller, 2000; Patlan *et al.*, 2017).

A series of Bouguer maps and residual maps that were constructed, showed that Paka prospect is associated with broad positive gravity anomaly and negative anomaly (Figure 4.1 – 4.2). The broad positive anomaly is due to massive dyke or shallow magma intrusions while the negative anomaly is due to high density fracture zones or fractured parts of rocks. The gravity high was also linked to plume activities under Kenya dome, where ascending high-density trachytic-Basaltic rock from the earth's mantle to the upper crust (Mutonga, 2013; Nyakundi, 2017; Waswa, 2017). Whereas the negative gravity resulted from the extensional force (stretching force on crustal rocks) that occurred between the Tanzanian craton and the mobile Mozambique Proterozoic basement belt, that increased rock fracturing which in turn increased the rock porosity hence low density (Smith, 1994; Robertson *et al.*, 2016; Wedge *et al.*, 2016). Gravity maps (Figure 4.1 – 4.2) show NW – SE trending of the mapped anomalies that are parallel to major rift fault and pre-existing Proterozoic basement regional tectonic structures (Mulwa *et al.*, 2014; Wedge *et al.*, 2016). Hence, these pre-existing structures seem to have played a role in guiding the orientation of gravity anomalies.

According to Mariita and Keller (2007), Kearey *et al.* (2013) and Nyakundi (2017) gravity low has density range (1.60 – 2.60) g/cm³ while an intruding rock has a density ranging from (2.70 – 3.20) g/cm³. The inversion 3D models for regions A – E, Figures 4.4 – 4.7 had a density greater than 2.70 g/cm³ hence our study interpreted modeled intrusion rocks under these region as intruding rocks while regions F – H that had a density lower than 2.60 g/cm³ and

modeled rocks interpreted as low gravity zones. The 3D modeled intrusion under region A (*Riongo area*) was interpreted as a dyke intrusion Figure 4.4– 4.5 while for region B, D and E as a dyke intrusion. Intrusion under region C was interpreted as dyke due to shallow magma that have high-density greater than 2.70 g/cm^3 at local depth $< 3\text{km}$. This dyke can serve as a geothermal heat source for the prospect and occurs directly on top of the Paka massive. The dyke intrusion under region C coincides with Paka caldera where a swarm of seismicity was detected beneath volcano at a depth $0 – 6 \text{ km}$ (Patlan *et al.*, 2017). From figure 2.11, the region between C, F and B coincides with the presence of fumaroles, which is proven that the interpreted intrusions are of hot rock. At a depth less than 1000 m , the interpreted dykes are due to lava rock of magnesium ion reach. But at a deeper greater than 3000 m from the earth's surface, the interpreted dykes are due to magma intrusions which can be viewed as tapping heat and can serve as a heat source for the prospect. The modeled depth was compared with the axial intrusion modeled magmatic bodies in south rift by Simiyu and Keller (2001) and in the northern Kenyan rift by Mariita and Keller (2007) where the studies indicated the existence of intrusion at $1 – 6 \text{ km}$ depth from the earth's surface. Also, with modeled intrusive dykes of density 2.9 g/cm^3 at varying depth $3 – 6 \text{ km}$ in Arus-Bogoria by Mulwa and Mariita (2013) and at varying depth of $2.3 – 6 \text{ km}$ in Olkaria field by Simiyu *et al.* (1995) and Simiyu (1996). Our study indicated that the calculated density of intrusive bodies varies from 2.70 g/cm^3 to 3.176 g/cm^3 depending on depth from the earth's surface. The modeled density complements the modeled mafic density 2.90 g/cm^3 intrusion by Simiyu and Keller (2001) and Mariita and Keller (2007) in which they associated with major volcanic centers along the axial rift. Generally, Paka volcano is predominantly dominated with trachytic volcanism that is derived from saturated magma and around 10 Ka , Quaternary (Neogene) eruption of young Basalt lavas erupted within the Paka caldera summit extending northwards in the flanks along NNE trending fissures (Omenda, 2007; Mutonga, 2013; Waswa, 2017). Due to this high-density eruptive material (Trachyte and Basalt rocks) in Paka volcano, we conclude that the intrusive at local depth is of Trachyte – Basalt origin. The high heat flow observed in the area as evidenced by fumaroles, steaming ground and hot springs could be due to these high density intruding bodies from the mantle under the volcano. This local depth intrusive in the form of the trachyte-basalt dyke was concluded to be tapping heat from large magma bodies at few kilometers from the surface. Such intrusive dykes may be geothermal heat sources.

The modeled low gravity zone under regions F – H, was mainly interpreted as due to a high density fracture zone. But Paka volcano is situated in northern Kenya rift where extensional/stretching force (extension local stress regime for shallow magmatism) that was subjected to crustal layer during the rifting process, the weak zone developed half graben or swarms of intra-faults as a result of rock fracturing (Njue, 2015; Robertson *et al.*, 2016). From figure (4.10 – 4.12), the density decreases with increase in depth from the earth's surface. Therefore as depth increases, the degree of fracturing/rock porosity increases (Figure 4.10 – 4.12). We interpreted the intensely fractured zone at deeper depth as due to lower trachyte fractured zone since the prospect is dominated by trachyte volcanism that erupted earlier (Omenda, 2007; Mutonga, 2013; Waswa, 2017). This lower trachyte that is highly fractured or faulted can form a good storage for geothermal fluids, hence it can be viewed as a geothermal aquifer. This zone occurs at a depth 1 – 3 km, and if filled with clay minerals due to infiltration, then it becomes a good conductor zone. According to Lichoro *et al.* (2017), from MT and TEM joint inversion, $\approx 10 \Omega\text{m}$ low resistive zone interpreted as altered clay zone at 1 – 2 km depth coincides with our lower trachyte fractured zone that is viewed as a good rock reservoir.

The 3D density model revealed a density pattern consistent with the existence of several intrusions within Paka prospect (Figure 4.13 – 4.17). Paka prospect is overlain with the surficial pyroclastic or Paka Basalt of density range (2.2 – 2.60) g/cm³ and of thickness 200 – 300 m, this can form a good capping layer for the Paka geothermal aquifers. The presence of low density pyroclastic volcanic soils are indicators of volcanic activities which deposited high materials close to the surface. The mapped surficial pyroclastic layer density it is in line with Arus-Bogoria modeled 2.40 g/cm³ surficial density (Mulwa and Mariita, 2013). Vertical planes across the density model were employed to give more information on density variation at depth.

From several profiles developed across the density model, the density for different structural features was analyzed in details (Figure 4.13 – 4.17). Intruding rocks of density greater 2.70 g/cm³ and low-density zones less than 2.60 g/cm³ were easily discerned from profiles. The high-density intrusion was due to massive trachyte-basalt rock since the volcano is dominated by trachytic and basaltic quaternary eruptions (Mutonga, 2013; Waswa, 2017). On the other hand, the low-density discerned as region F, G and H Figure (4.13 – 4.16) occur at a depth which does not exceed 5 km. The zone is viewed as due to high density fractured parts of rocks that form fault zones.

Due to low density of the fractured parts of rock, the zone F which is east of Paka volcanic summit was viewed as a fault zone. The zone having sandwiched with high density intrusion, it can form a good storage for geothermal fluids. From the seismicity study done by Patlan *et al.* (2017) indicated a low shear wave velocity anomaly to the east flank of Paka volcanic center at a depth 3 – 6 km that is due to a hot deep fluid to shallow circulation. This study agrees with our interpretation of low-density zone F that occur at depth 3 km. From our interpretation, Patlan *et al.* (2017) and Simiyu and Keller (2000) arguments, then we can conclude that, the fault at zone F is an active seismic zone. This fault zone F can be a good conduit for heat and geothermal fluid movement within the reservoir. This zone can be a good target for drilling geothermal wells since such zones have the largest mass output (Simiyu and Keller, 2000; Njue, 2015).

But the study done by Sippel *et al.* (2017) indicates that gravity ‘low’ in the northern Kenya rift including Paka prospect is due to positive thermal anomalies within the crust which involves partial melting or rock expansion that strongly weakens the upper crust. Also, from our density model, our study indicates an increase in shallow crustal density less than 2.70 g/cm³ from the western part of the prospect region D and E to the region B eastern part of the Pakal prospect greater than 2.70 g/cm³ density. The density trend can be attributed to compositional rock difference. The density increase trend was also observed by Sippel *et al.* (2017) where the study postulated that there is an overall trend of increasing mean crustal densities from mainly < 2.88 g/cm³ in western Kenya to > 2.88 g/cm³ in eastern Kenya. Also, from density model, we noted NW – SE trending structural features that are parallel to the major rift fault and pre-existing Proterozoic regional structures in northern Kenya rift (Smith, 1994; Simiyu and Keller, 1997; Mwaura, 2016; Robertson *et al.*, 2016; Wedge *et al.*, 2016). These pre-existing regional structures seem to have played a role in guiding the orientation and trending for this local depth structural features under Pakal prospect.

The subsurface fault structures were enhanced through the application of gravity derivative filters (Figure 4.18 – 4.21). The horizontal gradient HG, tilt derivative TDR, and horizontal derivative of the tilt derivative HG-TDR in which they revealed shallow faults that trends in NW – SE direction. While analytical signal delineated regional faults that trend in N – S and NE – SW direction. The intra-rift shallow fault swarms are resulting from extensional tectonic of local stress regime that is responsible for shallow magmatism in northern Kenya rift (Robertson *et al.*, 2016). The shallow faults in the earth’s subsurface direct the flow of thermal

fluids on the upper parts of the basements while the top faults direct the flow of water from rift scarps to the hot masses underground (Nyakundi, 2017).

Hence at local scale, these trending faults and fractures are essential in enhancing permeability in the Paka prospect. The regional faults delineated using analytical signal (Figure 4.21) seem to be the axial fault that was discerned at the deeper depth and trends in the same direction as the surface faults. The presence of this subsurface axial faults that extend southwards to Lake Baringo can serve as axial flow paths for recharge of the Paka prospect. As per Lagat *et al.* (2007), the axial faults probably serve as recharging for the axial prospects along the rift. At regional view, the interaction between lateral and axial flows can be augmented by faults and dykes trending NNE – SSW and N – S along the rift. Faults can cause lateral flows to flow longer and deeper paths and to align with axial flow paths within the rift floor (Bernard *et al.*, 2014). For the Paka volcano, lateral recharge is from Laikipia escarpment, and Baringo ranges and axial recharge is from Lake Baringo (Mutonga, 2013). The fluid can circulate deep through the reservoir rocks and heated up in the vicinity of shallow intrusive.

CHAPTER FIVE

CONCLUSIONS AND RECOMMENDATIONS

5.1 Conclusion

The results obtained from this study showed that the gravity method is an effective tool for making sufficient modeling and accurate determination of geophysical parameters.

5.1.1 Conclusion on the Bouguer Anomaly Map under Paka volcano

Bouguer anomaly maps revealed that:

- i) In Paka volcano, the local geothermal structural features are associated with positive gravity anomalies and negative gravity anomalies.
- ii) The NNW – SSE trending of the mapped anomalies appears to be parallel to major faults trends and pre-existing regional tectonic structures like Nyanza rift (Kavirondo), Sudan-Anza rift and Proterozoic basement trends.

5.1.2 Conclusion on 3D Gravity Inversion Models in Paka Volcano

The inversion modelling showed that:

- i) For positive gravity regions, intruding dyke are of density range (2.70 – 3.176) g/cm³
- ii) The intruding dyke is of trachyte-basalts rocks and at depth less than 1000 m, it was interpreted as due to lava rocks of magnesium iron reach and at depth greater than 3000 m as magma that can serve as a geothermal heat source for the Paka geothermal prospect
- iii) Negative gravity zones are due to parts of rock fracturing and of density range (1.90 – 2.40) g/cm³. This forms a good rock storage for geothermal fluids.

5.1.3 Conclusion on the Interpretation of 3D Density Model

The following conclusions were derived from 3D density model:

- i) It revealed a density distribution patterns that are consistent with the existence of several intrusion of high density dykes within the study area
- ii) It is overlain with surficial pyroclastic rocks or Paka Basalt of layer thickness 200 – 300 m across the prospect of density range (2.20 – 2.60) g/cm³ that can serve as a capping layer for the geothermal aquifer or regions with high fracture density.
- iii) The region from Paka caldera to the eastern flank and to the north-western flank along the fault zone can be good target for drilling geothermal wells

- iv) There is NW – SE trending of the mapped structural dykes and faults that are parallel to the major rift fault and pre-existing Proterozoic regional structures in northern Kenya.

5.1.4 Conclusion on delineating the subsurface volcanic fault structures, their influence on the hydrothermal fluid flow and contribution to the geothermal system in Paka volcano

The study revealed and delineated both deep and shallow subsurface fault zones that are essential in enhancing permeability. The deep fault zones serve as axial and lateral flow paths for recharge of the Paka prospect while the shallow faults in the earth's subsurface direct the flow of thermal fluids on the upper parts of the basements. The deeper fractured fault zones can serve as a storage rock for geothermal fluids.

5.2 Recommendations

5.2.1 Recommendations Based on this Research Results

In view of the finding of this study, the following are recommendations

- i) Local gravity analysis < 5 km, reveals the near surface structural information such as like defining the geometry, depth and extent of the heat sources, and the buried faults which were overlooked at regional analysis
- ii) Massive intrusions in the form of dykes at depth greater than 3000 m can be tapping heat from large magma intrusion rock a few kilometers from the earth's surface and can serve as geothermal heat sources for the Paka prospect.
- iii) The mapped high density fracture zones at deeper depth greater than 2000 m can serve as a geothermal aquifers
- iv) Exploratory geothermal borehole drilling be undertaken in Paka prospect area from the caldera summit towards the eastern flank and northwestern flank.

5.2.2 Recommendation for Further Studies

Even though the study area is prone to underlined massive intrusions and fault zones, microgravity, magnetotellurics and microseismic monitoring be undertaken to help in tracking possible magma migration and underground geothermal fluid movement. Such data could, in turn, play an important role in predicting the future drilling sites. Also, the data can be used for comparison.

REFERENCES

- An, M., and Lu, C. (2013). Algorithms for the discrete Fourier transform and convolution. *Springer Science and Business Media*, **25**, 423-429.
- Anudu, G. K., Stephenson, R. A., and Macdonald, D. I. (2014). Using high-resolution aeromagnetic data to recognize and map intra-sedimentary, volcanic rocks and geological structures across the Cretaceous middle Benue Trough, Nigeria. *Journal of African Earth Sciences*, **99**, 625-636.
- Arisoy, M.O., and U. Dikmen (2013). Edge detection of magnetic sources using an enhanced total horizontal derivative of the tilt angle. *Bulletin Earth Science Application Research Center Hacet University*, **34** (1), 73-82
- Baker, B. H., (1986). Tectonics and volcanism of the southern Kenya rift valley and its influence on sedimentation in the African rifts. *Geological Society of London*, **25**, 45-57
- Baker, B. H., Mitchell, J.G., Williams, L.A.J., (1988). Stratigraphy, geochronology and volcano-tectonic evolution of the Kedong-Naivasha-Kinangop region, Gregory rift valley, Kenya. *Geological Society of London*, **27**, 107-116
- Baker, B.H. and Wohlenberg, J., (1971). Structural and evolution of the Kenya rift valley. *Nature*, **229**, 538-542
- Baker, B.H., Mohr, P.A., Williams, L.A.J., (1972). Geology of the eastern rift system of Africa. *Geological Society of America*, **17**, 1-67
- Bhattacharya, Indrajit, Jan Wuite and Kenneth C. Jezek. (2006). Determination of Absolute Gravity at BPRC/US Polar Rock Repository, *BPRC Technical Report Byrd Polar Research Center. The Ohio State University, Columbus, Ohio*, **2**, 15 pg
- Blakely, R.J. (1996). *Potential Theory in Gravity and Magnetic Applications*. Cambridge University Press, Cambridge, **41**.
- Boashash, B. (2015). Time-frequency signal analysis and processing: a comprehensive reference. *Academic Press*
- Bruna, J., and Mallat, S. (2013). Invariant scattering convolution networks. *IEEE transactions on pattern analysis and machine intelligence*, **35** (8), 1872-1886.
- Chen, Q., Dong, Y., Cheng, S., Han, L., Xu, H. H., and Chen, H. (2014). Interpretation of fault system in the Tana Sag, Kenya, using edge recognition techniques and Euler Deconvolution. *Journal of Applied Geophysics*, **109**, 150-161

- Chiao, L. Y., Chen, Y. N., and Gung, Y. (2014). Constructing empirical resolution diagnostics for kriging and minimum curvature gridding. *Journal of Geophysical Research: Solid Earth*, **119** (5), 3939-3954
- Connor, C. B., Conway, F. M., and Sigurdsson, H. (2000). Basaltic volcanic fields. *Encyclopedia of volcanoes*, 331-343.
- Cooper, G. R. J. (2004). The textural analysis of gravity data using co-occurrence matrices. *Computers and Geosciences*, **30** (1), 107-115.
- De Castro, D. L., Fuck, R. A., Phillips, J. D., Vidotti, R. M., Bezerra, F. H., and Dantas, E. L. (2014). Crustal structure beneath the Paleozoic Parnaíba Basin revealed by airborne gravity and magnetic data, Brazil. *Tectonophysics*, **614**, 128-145.
- Debeglia, N., and J. Corpel (1997). Automatic 3-D interpretation of potential Field data using analytic signal derivatives. *Geophysics*, **62**(1), 87-96
- Døssing, A., Hansen, T. M., Olesen, A. V., Hopper, J. R., and Funck, T. (2014). Gravity inversion predicts the nature of the Amundsen Basin and its continental borderlands near Greenland. *Earth and Planetary Science Letters*, **408**, 132-145.
- Dragomiretskiy, K., and Zosso, D. (2014). Variational mode decomposition. *IEEE transactions on signal processing*, **62** (3), 531-544
- Dunkley P. N., Smith, M., Allen, D.J., and Darling, W.G., (1993). The geothermal activity and geology of the northern sector of the Kenya Rift Valley. *British Geological Survey Research Report SC*, **93** (1)
- Durham, R. L. (2017). Potential field modelling across the neodymium line defining the Paleoproterozoic-Mesoproterozoic boundary of the southeastern margin of Laurentia. *Theses and Dissertations--Earth and Environmental, University of Kentucky*
- Fairhead, J.D., (1976). The structure of the lithosphere beneath the eastern rift, East Africa, deduced from gravity studies. *Tectonophysics*, **30**, 269-298
- Fedi M. and G. Florio, (2001). Detection of potential field source boundaries by the enhanced horizontal derivative method. *Geophysical Prospecting*, **49**, 40–58
- Hackman, B. D., Charsley, T. J., Key, R. M., and Wilkinson, A. F. (1990). The development of the East African Rift system in north-central Kenya. *Tectonophysics*, **184** (2), 189-211.
- Hautot, S., Tarits, P., Whaler, K., Le Gall, B., Tiercelin, J., Le Turdu, C., (2000). Deep structure of the Baringo Rift Basin (Central Kenya) from three-dimensional Magnetotelluric imaging: Implications for rift evolution. *Geophysics*, **105** (23), 493-518

- Hinze, W. J. (2003). Bouguer reduction density, why 2.67?. *Geophysics*, **68** (5), 1559-1560.
- Hinze, W. J., Aiken, C., Brozena, J., Coakley, B., Dater, D., Flanagan, G. ... and Kucks, R. (2005). New standards for reducing gravity data: The North American gravity database. *Geophysics*, **70** (4), 25-32.
- Hinze, W. J., Von Frese, R. R., and Saad, A. H. (2013). *Gravity and magnetic exploration: Principles, practices, and applications*. Cambridge University Press.
- Hsu, S.K., J.-C. Sibuet, and C.T. Shyu (1996). High-resolution detection of geologic boundaries of potential field anomalies: An enhanced analytic signal technique, *Geophysics*, **61**(2), 373-386
- Iwanaka, D. (2013). U.S. Patent Application No. 14/426,717.
- Jiang, W., Huang, T., Mao, X., Wang, L., Zhao, Y., Jia, C., ... and Ma, J. (2017). Gridded emission inventory of short-chain chlorinated paraffin and its validation in China. *Environmental Pollution*, **220**, 132-141.
- Kanda I.K., (editor), Ranks L., Bett E.K., Kipngok, J.K., Mutonga, . M. B., Sosi, J. Gichira, R.M Mwakirani, I.J. Mboin, C. Ndongoli, L. Oundo, E. Ouko, H. Mwawasi, (2011). Paka Prospect: Investigations of its geothermal potential. *GDC Internal report*.
- Kearey, P., Brooks, M., and Hill, I. (2013). An introduction to geophysical exploration. *John Wiley & Sons*.
- Keating, P., and M. Pilkington (2004). Euler deconvolution of the analytic signal and its application to magnetic interpretation. *Geophysical Prospecting*, **52**(3), 165-182
- Keller, G.R., Prodehl, C., Khan, M.A., Morgan, P., Braile, L.W., Olsen, K.H., Wendlandt, R.F., Baldridge, W.S., (1994). The East African rift system in the light of KRISP 90. In: Prodehl, C., Keller, G.R., Khan, M.A. (Eds.), Crustal and Upper Mantle Structure of the Kenya Rift. *Tectonophysics* **236**, 465–483
- Kemei J.K., Langat G.K., Ambusso W. and Okumu J. I., (2011). Results of gravity and ground magnetic survey of menengai geothermal fields, Kenya. *Proceedings, Kenya geothermal conference Kenyatta international conference center, Nairobi, November*, 21-22
- Khazri, D., and Gabtni, H. (2018). Geophysical methods integration for deep aquifer reservoir characterization and modeling (Sidi Bouzid basin, central Tunisia). *Journal of African Earth Sciences*, **138**, 289-308.
- Kipng'ok, J., and Nyamongo, J. (2013). Fumarole gas geochemistry of Paka geothermal prospect, North Rift, Kenya. *Geothermal Resources Council Transactions*, **37**.

- Lagat J.k., (editor), Omenda P.O., Mungania, J., Mariita, N.O., Wambugu, J.M., Opondo, K., Ofwona, C.O. Mwawongo, B.M., Kubo., Wetangula, G., (2007). Geoscientific Evaluation of the Paka Geothermal Prospect, KenGen. *Internal report*.
- Li, X., and Goetze, H. J. (2001). Comparison of some gridding methods. *The Leading Edge*, **18** (8), 898 -900.
- Lichoro, C. M., Árnason, K., and Cumming, W. (2017). Resistivity imaging of geothermal resources in northern Kenya rift by joint 1D inversion of MT and TEM data. *Geothermic*, **68**, 20-32.
- Liu, L., Gao, S. S., Liu, K. H., and Mickus, K. (2017). Receiver function and gravity constraints on the crustal structure and vertical movements of the Upper Mississippi Embayment and Ozark Uplift. *Journal of Geophysical Research: Solid Earth*.
- Longo, L. M., De Ritis, R., Ventura, G., and Chiappini, M. (2016). Analysis of the Aeromagnetic Anomalies of the Auca Mahuida Volcano, Patagonia, Argentina. *Pure and Applied Geophysics*, **173** (10-11), 3273-3290.
- Ma, G., Liu, C., and Huang, D. (2015). The removal of additional edges in the edge detection of potential field data. *Journal of Applied Geophysics*, **114**, 168-173
- Ma, G., Liu, C., Huang, D., and Li, L. (2013). A stable iterative downward continuation of potential field data. *Journal of Applied Geophysics*, **98**, 205-211.
- Macdonald, R., Bagiński, B., and Upton, B. G. J. (2014). The volcano–Pluton interface; The Longonot (Kenya) and Kûngnât (Greenland) peralkaline complexes. *Lithosphere*, **196**, 232-241.
- MacLeod, I.N., K. Jones, and T.F. Dai (1992). The 3-D analytic signal in the interpretation of total magnetic field data at low magnetic latitudes, *Exploration. Geophysics*, **24**(3-4), 679-688
- Mariani, P., Braitenberg, C., and Ussami, N. (2013). Explaining the thick crust in Paraná basin, Brazil, with satellite GOCE gravity observations. *Journal of South American Earth Sciences*, **45**, 209-223.
- Mariita, N., (2007). The gravity method. *Short Course II on a surface exploration of geothermal resources, Kenya*, 1-9.
- Mariita, N.O., (2003). An Integrated geophysical study of the northern Kenya rift crustal structure: Implications for geothermal energy prospecting in Menengai area. *Ph.D. dissertation, University of Texas at El Paso, USA*, 1-188

- Mariita, N.O., and Keller, G.R., (2007). An integrated geophysical study of the northern Kenya Rift. *Journal of African Earth Sciences*, **48**, 80-94
- Martínez-Moreno, F. J., Galindo-Zaldívar, J., Pedrera, A., Teixidó, T., Peña, J. A., and González Castillo, L. (2014). Regional and residual anomaly separation in microgravity maps for cave detection: The case study of Gruta de las Maravillas (SW Spain). *Journal of Applied Geophysics*, **114**, 1-11.
- Mauri, G., Husein, A., Mazzini, A., Irawan, D., Sohrabi, R., Hadi, S., ... and Miller, S. A. (2017). Insights on the structure of Lusi mud edifice from land gravity data. *Marine and Petroleum Geology*, **79**, 245-251
- Mechie, J., Keller, G. R., Prodehl, C., Gaciri, S., Braile, L. W., Mooney, W. D. Gajewski, D. and Sandmeier, K.-J. (1994). Crustal structure beneath the Kenya Rift from axial profile data. *Tectonophysics*, **236**, 179–199.
- Milligan, P.R. and Gunn, P.J., (1997). Enhancement and presentation of airborne Geophysical data. *Journal of Australian Geology and Geophysics*, **17** (2), 63-75
- Morley, C.K. (Eds.), (1999). GeoScience of Rift Systems – Evolution of East Africa. *AAPG Studies in Geology*, **44**, 250p.
- Muirhead, J. D., Kattenhorn, S. A., and Le Corvec, N. (2015). Varying styles of magmatic strain accommodation across the East African Rift. *Geochemistry, Geophysics, Geosystems*, **16**(8), 2775-2795.
- Mulwa, J. K., and Mariita, N. O. (2015). Dyking processes in Arus-Bogoria geothermal prospect in Kenya revealed using gravity and microseismic data. In *37th New Zealand Geothermal Workshop: The next 10,000 Megawatts*. The University of Auckland, New Zealand Geothermal Association.
- Mulwa, J. K., Kimata, F., Suzuki, S., and Kuria, Z. N. (2014). The seismicity in Kenya (East Africa) for the period 1906–2010: A review. *Journal of African Earth Sciences*, **89**, 72-78.
- Mulwa, J., and Mariita, N. (2013). A comparative analysis of gravity and microseismic results from Arus-Bogoria geothermal prospect, Kenya. *Scholarly Journal of Scientific Research and Essay*, 2315-6163.
- Mulwa, J., (2011). Integrated Geophysical Study of Lake Bogoria Basin, Kenya: Implications for Geothermal Energy Prospecting (*Doctoral dissertation, Ph.D. dissertation, University of Nairobi, Kenya*).

- Munoz-martin, A., Catalan. M., Martin-Davila. J. and Carbo. A., (2005). Upper crustal structure of Deception Island area (Bransfield Strait, Antarctica) from gravity and magnetic modeling. *Antarctic Science* **17** (2), 213–224
- Musset, A. E. and Aftab, K. M., (2009). *Looking into the Earth - An Introduction to Geological Geophysics*: (revised edition) New York: Cambridge University Press, pg 107- 137
- Mutonga, M. (2013). The Geology of Paka Volcano, and its Implication on Geothermal. *Geothermal Resources Council Transactions*, 431-436.
- Mwakirani. R.M., (2011). Resistivity structure of Paka geothermal prospect in Kenya. *Internal report*, **26**, 5-13
- Mwangi, M. (2005), Country Update Report for Kenya 2000-2005. *Proceedings World Geothermal Congress 2005 Antalya, Turkey*, 34, 1-10
- Mwaura, H. K. (2016). *Geophysical Mapping of Shallow Structures Controlling Geothermal Reservoir Recharge in Eburru Geothermal Field, Kenya Rift* (Doctoral dissertation, University of Nairobi).
- Namaswa, S.W., Ambusso, W.J. and Migwi, C.M., (2014). Gravity variation across Nakaporon fault in Korosi geothermal prospecting field. *The International Journal of Science and Technology*, **2**(8), 121-124
- Nishijima, J., and Naritomi, K. (2017). Interpretation of gravity data to delineate underground structure in the Beppu geothermal field, central Kyushu, Japan. *Journal of Hydrology: Regional Studies*, **11**, 84-95.
- Njue, L. M. (2015). A geological model of Korosi geothermal prospect, Kenya. In *Proceedings World Geothermal Congress, Melbourne, Australia, 19–25 April 2015*.
- Nyakundi, E. R. (2017). Geophysical Investigation of Geothermal Potential of the Gilgil Area, Nakuru County, Kenya Using Gravity Method (*Doctoral dissertation, Kenyatta University*).
- Ochieng, L. (2014). Overview of geothermal surface exploration methods. *001374011*.
- Odera, P. A. (2016). Assessment of EGM2008 using GPS/ leveling and free-air gravity anomalies over Nairobi County and its environs. *South African Journal of Geomatics*, **5** (1), 17-30.
- Ofwona, C., Omenda, P., Mariita, N., Wambugu, J., Mwawongo, G., and Kubo, B. (2006). Surface geothermal exploration of Korosi and Chepchuk prospects. *KenGen Internal report, unpublished*, 45-62.

- Oldenburg, D.W. and Pratt, D.A., 2007. Geophysical Inversion for Mineral Exploration: a Decade of Progress in Theory and Practice. *The Leading Edge*, 61-95.
- Omenda, P., and Simiyu, S. (2015). Country update report for Kenya 2010–2014. *Proceedings World Geothermal*.
- Omenda, P. (2014a). Geothermal country update report for Kenya: 2014. *001374011*.
- Omenda, P. (2014b). The geology and geothermal activity of the East African Rift. *001374011*.
- Omenda, P. A. (2007). Status of geothermal exploration in Kenya and plans for its development. *Short Course II on Surface Exploration for Geothermal Resources, organized by UNU-GTP and KenGen, at Lake Naivasha, Kenya*, 2-17.
- Omenda, P. A. (2000). The anatetic origin for comendite in Olkaria geothermal field, Kenya rift: geochemical evidence for syenitic protolith. *African Journal of Science and Technology*, **1** (2), 39-47
- Omenda P.A., Oondo K., Lagat J., Mungania J., Mariita N., Onacha S., Simiyu S., Wetang'ula G. and Ouma P., (2000). Ranking of geothermal prospects in the Kenya Rift. *KenGen Internal report*, pp. 121
- Omenda, P. A. (1998). The geology and structural controls of the Olkaria geothermal system, Kenya. *Geothermics*, **27**(1), 55-74.
- Oruç, B., Sertçelik, I., Kafadar, Ö., and Selim, H. H. (2013). Structural interpretation of the Erzurum Basin, eastern Turkey, using curvature gravity gradient tensor and gravity inversion of basement relief. *Journal of Applied Geophysics*, **88**, 105-113
- Ouma, P.A., (2010). geothermal exploration and development of the Olkaria geothermal field. Paper presented at *Short Course V on Exploration for Geothermal Resources organized by UNU-GTP, GDC and KenGen, at Lake Bogoria and Lake Naivasha, Kenya*, pg 16.
- Parasnis D.S. (1997) Principles of Applied Geophysics. *Chapman and Hall, U. S. A.* 61-103
- Patlan, E., Antony, W., Galen, K. and Aaron, A. V., (2013). Ambient Noise Cross-Correlation Study of Menengai Caldera: Geothermal Prospect in the Central Kenya Dome GDC. *Transactions*, **37**, 1037-1043
- Patlan, E., Velasco, A. A., Wamalwa, A., and Kaip, G. (2017). Seismic Zone at East Africa Rift: Insights into the Geothermal Potential. *Proceedings, 42nd Workshop on Geothermal Reservoir Engineering Stanford University, Stanford, California, February 13-15, 2017*
- Pawlowski, R. S. (1995). Green's equivalent-layer concept of gravity band-pass filter design. *Geophysics*, **59** (1), 69-76.

- Prodehl, C., Keller, G.R., Khan, M.A., (Eds), (1994), Crustal and Upper mantle structure of the Kenya Rift. *Tectonophysics*, **236**, 2-483
- Prodehl, C., Ritter, J., Mechier, J., Keller, G.R., Khan, M.A., Fuchs, K., Nyambok, I.O., Obel, J.D, (1997). The KRISP 94 Lithospheric investigation of southern Kenya-the experiments and their main results, In Stress and stress release in the Lithosphere. *Tectonophysics*, **278**, 121-148
- Renaut, R. W., Owen, R. B., and Ego, J. K. (2017). Geothermal activity and hydrothermal mineral deposits at southern Lake Bogoria, Kenya Rift Valley: Impact of lake level changes. *Journal of African Earth Sciences*, **129**, 623-646.
- Richarte, D., Lupari, M., Pesce, A., Nacif, S., and Gimenez, M. (2018). 3-D crustal-scale gravity model of the San Rafael Block and Payenia volcanic province in Mendoza, Argentina. *Geoscience Frontiers*, **9**(1), 239-248.
- Ring, U. (2014). The East African Rift System. *Austrian Journal of Earth Sciences*, **107**(1), 231-236
- Robertson, E. A. M., Biggs, J., Cashman, K. V., Floyd, M. A., and Vye-Brown, C. (2016). Influence of regional tectonics and pre-existing structures on the formation of elliptical calderas in the Kenyan Rift. *Geological Society, London, Special Publications*, **420**(1), 43-67.
- Roecker, S., Ebinger, C., Tiberi, C., Mulibo, G., Ferdinand-Wambura, R., Mtelela, K., ... and Peyrat, S. (2017). Subsurface images of the Eastern Rift, Africa, from the joint inversion of body waves, surface waves and gravity: investigating the role of fluids in early-stage continental rifting. *Geophysical Journal International*, **210**(2), 931-950.
- Roest, W.R., J. Verhoef, and M. Pilkington (1992). Magnetic interpretation using 3-D analytic signal. *Geophysics* **57**, 1, 116-125
- Rooney, D., Hutton, R.S. (1977). A Magnetotelluric and magneto-variation study of the Gregory Rift Valley, Kenya. *Geophysics Australia Society*, **51**, 91-119.
- Rosid, M. S., and Siregar, H. (2017). Determining fault structure using first horizontal derivative (FHD) and horizontal vertical diagonal maxima (HVDM) method: A comparative study. In *AIP Conference Proceedings*, **62**, (1), 171pg
- Roy, R., Benedicto, A., Grare, A., Béhaegel, M., Richard, Y., and Harrison, G. (2017). Three-dimensional gravity modeling applied to the exploration of uranium unconformity-related

- basement-hosted deposits: the Contact prospect case study, Kiggavik, northeast Thelon region (Nunavut, Canada). *Canadian Journal of Earth Sciences*, **54**(8), 869-882.
- Salem, A., S. Williams, J.D. Fairhead, R. Smith, and D. Ravat (2008). Interpretation of magnetic data using tilt-angle derivatives. *Geophysics* **73**, 1-10
- Salem, A., S. Williams, J.D. Fairhead, D. Ravat, and R. Smith (2007). Tilt-depth Method: A simple depth estimation method using first-order magnetic derivatives. *The Leading Edge*, **26**(12), 1502-1505
- Sceal, J. S. C., (1974), The geology of Pako volcano and the country to the east, Baringo District, Kenya, *unpublished Ph.D. thesis, University of London*
- Shako, L., and Wamalwa, A. (2014). GIS Applications in Heat Source Mapping in Menengai Geothermal Field. In *Proceedings of the 5th African Rift Geothermal Conference*.
- Shamsipour, P., Chouteau, M., and Marcotte, D. (2017). Data analysis of potential field methods using geostatistics. *Geophysics*, **82** (2), G35-G44.
- Simiyu, S. M. (2013). Application of micro-seismic methods to geothermal exploration: examples from the Kenya Rift.
- Simiyu, S. M. (2010, April). Status of geothermal exploration in Kenya and plans for its development. In *Proceedings world geothermal congress* (pp 25-29).
- Simiyu, S.M. and Keller G.R., (2001). An integrated geophysical analysis of the upper crust of the southern Kenya Rift. *Geophysical journal international*, **147**, 543-556
- Simiyu, S. M., and Keller, G. R. (2000). Seismic monitoring of the Olkaria Geothermal area, Kenya Rift valley. *Journal of Volcanology and Geothermal Research*, **95**(4), 197-208.
- Simiyu, S.M. and Keller, G.R., (1997). An integrated analysis of lithospheric structure across the East African plateau based on gravity anomalies and recent seismic studies. *Tectonophysics*, **278**, 291-313
- Simiyu, S.M., (1996). Integrated geophysical study of the crustal structure of the southern Kenya Rift. *Ph.D. Dissertation, University Texas-El Paso*, 240 pp.
- Simiyu, S. M., Omenda, P. A., Anthony, E. Y., and Keller, G. R. (1995). Geophysical and geological evidence for the occurrence of shallow magmatic intrusions in the Naivasha sub-basin of the Kenya Rift. *EOS Transactions of the AGU*, **76**, 257-258.
- Sippel, J., Meeßen, C., Cacace, M., Mechie, J., Fishwick, S., Heine, C., ... and Strecker, M. R. (2017). The Kenya rift revisited: insights into lithospheric strength through data-driven 3-D gravity and thermal modeling. *Solid Earth*, **8**(1), 45-46.

- Skowronek, V., Rambach, R. W., and Franke, T. (2015). Surface acoustic wave controlled integrated band-pass filter. *Microfluidics and Nanofluidics*, **19** (2), 335-341.
- Smith, M., (1994). Stratigraphic and structural constraints on mechanisms of active rifting in the Gregory Rift, Kenya. *Tectonophysics*, **236**, 3-22
- Smith, M., Mosley, P.N., (1993). Crustal heterogeneity and basement influence on the development of the Kenya Rift, East Africa. *Tectonics*, **12**, 591-606
- Srivastava, H. M., and Buschman, R. G. (2013). Theory and applications of convolution integral equations. *Springer Science and Business Media*, **79**, 342-345
- Ström, T. (2018). A geophysical study of the Martinez area: Modelling and interpretation of primarily aeromagnetic data.
- Swain, C. J. (1992). The Kenya rift axial gravity high: a re-interpretation. *Tectonophysics*, **204**(2), 59-70.
- Swain, C.J., Khan, M.A., Wilton, T.J., Maguire, P.K.H., Griffiths, D.H., (1981). Seismic and gravity surveys in the Lake Baringo-Tugen Hills area, Kenya rift valley. *Geological Society of London*, **138**, 93-102
- Swain, C.J., Maguire, P.K.H., Khan, M.A, (1994). Geophysical experiments and models of the Kenya rift before 1989. In: Crustal and Upper Mantle Structure of the Kenya Rift. *Tectonophysics*, **236**, 23-32
- Tapponnier, P., and Molnar, P. (1977). Active faulting and tectonics in China. *Journal of Geophysical Research*, **82**(20), 2905-2930.
- Telford, W. M., Geldart, L., and Sheriff, R. (1990). Applied Geophysics. *Cambridge university press*, **1**
- Tiberi, C., Ebinger, C., Ballu, V., Stuart, G. and Oluma, B, (2005). Inverse models of gravity data from the Red Sea–Aden–East African rifts triple junction zone. *Geophysics. Journal International*, **163**, 775–787
- Tongue, J., Maguire, P., Burton, P., (1994). An earthquake study in the Lake Baringo basin of the central Kenya Rift. *Tectonophysics*, **236**, 151-164
- Tongue, J.A., (1992). The Tomographic study of local earthquake data from the Lake Bogoria region of the Kenya Rift Valley. *Geophysics*, **109**, 249-258
- Tongue, J.A., Maguire, P.K.H., Young, P.A.V, (1992). Seismicity distribution of temporary earthquake recording networks in Kenya. *Tectonophysics*, **204**, 71-79

- Truckle, P. H. (1977). The geology of the area to the south of Lokori, South Turkana, Kenya (*Doctoral dissertation, University of Leicester (United Kingdom)*).
- Uwiduhaye, J. D. A., Mizunaga, H., and Saibi, H. (2017). A geophysical investigation using gravity data in Kinigi geothermal field, northwest Rwanda. *Journal of African Earth Sciences*.
- Verduzco, B., J.D. Fairhead, C.M. Green, and C. MacKenzie (2004). New insights into magnetic derivatives for structural mapping. *The Leading Edge*, **23**, 116-119
- Wadge, G., Biggs, J., Lloyd, R., and Kendall, J. M. (2016). Historical volcanism and the state of stress in the East African Rift System. *Frontiers in Earth Science*, **4**, 86pg
- Wamalwa, A. M., and Serpa, L. F. (2013). The investigation of the geothermal potential at the Silali volcano, Northern Kenya Rift, using electromagnetic data. *Geothermic*, **47**, 89-96.
- Wamalwa, A. M., Mickus, K. L., and Serpa, L. F. (2013). Geophysical characterization of the Menengai volcano, Central Kenya Rift from the analysis of Magnetotelluric and gravity data. *Geophysics*, **78** (4), 187-199
- Waswa, A. K. (2017). Mapping of Hydrothermal Minerals Related to Geothermal Activities Using Remote Sensing and GIS: Case Study of Paka Volcano in Kenyan Rift Valley. *International Journal of Geosciences*, **8**(5), 711-725
- White, R. H., Battisti, D. S., and Skok, G. (2017). Tracking precipitation events in time and space in gridded observational data. *Geophysical Research Letters*, **44**(16), 8637-8646.
- William, L. A. J., Macdonald, R. and Chapman, R. R., (1984). Late Quaternary caldera volcanoes of the Kenya Rift Valley. *Journal of Geophysical Research*, **89** (10), 8553-8570
- Williams, E., Fairhead J., and Flanagan G., (2005). Comparison of grid Euler deconvolution with and without 2D constraints using a realistic 3D magnetic basement model. *Geophysics*, **70**, 13-21
- Young, P.A.V., Maguire, P.K.H., Laffoley, N. d'A., Evans, J.R, (1991). Implications of the distribution of seismicity near Lake Bogoria in the Kenya Rift. *Geophysics*, **105**, 665-674
- Yuan, Y., and Yu, Q. (2015). Edge detection in potential-field gradient tensor data by use of improved horizontal analytical signal methods. *Pure and Applied Geophysics*, **172** (2), 461-472